


ผลของโครงสร้างจุลภาคของหัววัดแก๊สชนิดดีบุกออกไซด์ต่อความไวในการตรวจวัดแก๊ส



นางสาวอุทุมพร ก่อเกิด

วิทยานิพนธ์นี้เป็นส่วนหนึ่งของการศึกษาตามหลักสูตรปริญญาวิทยาศาสตรมหาบัณฑิต

สาขาวิชาเทคโนโลยีเซรามิก ภาควิชาวัสดุศาสตร์

คณะวิทยาศาสตร์ จุฬาลงกรณ์มหาวิทยาลัย

ปีการศึกษา 2546

ISBN 974-17-4325-4

ลิขสิทธิ์ของจุฬาลงกรณ์มหาวิทยาลัย

EFFECTS OF MICROSTRUCTURE OF SINTERED TIN OXIDE ON
GAS-SENSING SENSITIVITY



Miss Utoomporn Korkerd

สภามหาวิทยาลัยบูรพา
จุฬาลงกรณ์มหาวิทยาลัย

A Thesis Submitted in Partial Fulfillment of the Requirements
for the Degree of Master of Ceramic Technology in Materials Science
Department of Materials Science

Faculty of Science
Chulalongkorn University
Academic Year 2003
ISBN 974-17-4325-4

Thesis Title EFFECTS OF MICROSTRUCTURE OF SINTERED TIN
 OXIDE ON GAS-SENSING SENSITIVITY
By Miss Utoomporn Korkerd
Field of Study Materials Science
Thesis Advisor Associate Professor Supatra Jinawath
Co-Advisor Dr. Apinya Panupat

Accepted by the Faculty of Science, Chulalongkorn University in Partial
Fulfillment of the Requirements for the Master's Degree

..... Dean of Faculty of Science
(Professor Piamsak Menasveta, Ph.D.)

THESIS COMMITTEE

..... Chairman
(Associate Professor Saowaroj Chuayjuljit)

..... Thesis Advisor
(Associate Professor Supatra Jinawath, Ph.D.)

..... Thesis Co-advisor
(Apinya Panupat, Ph.D.)

..... Member
(Professor Shigetaka Wada, Ph.D.)

..... Member
(Dujreutai Pongkao Kashima, Ph.D.)

อุทุมพร ก่อเกิด: ผลของโครงสร้างจุลภาคของหัววัดแก๊สชนิดดีบุกออกไซด์ต่อความไวในการตรวจวัดแก๊ส (Effects of microstructure of sintered tin oxide on gas-sensing sensitivity)

อาจารย์ที่ปรึกษา: รศ.ดร.สุพัตรา จินาวัฒน์, อาจารย์ที่ปรึกษาร่วม ดร.อภิญญา ภาณุภัทร, 94 หน้า, ISBN 974-17-4325-4

ดีบุกออกไซด์ (SnO_2) เป็นวัสดุที่นำใช้อย่างแพร่หลายในการตรวจวัดแก๊ส โดยดีบุกออกไซด์เป็นสารกึ่งตัวนำประเภท n-type เมื่อมีโมเลกุลของแก๊สเข้ามาดูเกาะที่ผิวของสารกึ่งตัวนำ มีผลทำให้ความต้านทานของสารกึ่งตัวนำเปลี่ยนแปลงไป สมบัติเด่นของดีบุกออกไซด์ คือ มีความสามารถในการตอบสนองต่อแก๊สได้ดีที่อุณหภูมิต่ำและสามารถตรวจวัดแก๊สที่มีความเข้มข้นต่ำได้ ในงานวิจัยนี้ได้ทำการศึกษาผลของปริมาณสารโด๊ป (แอนติโมนีออกไซด์) ที่มีต่อขนาดของอนุภาคและความสามารถในการตอบสนองต่อแก๊สไอโซบิวเทน ในงานวิจัยได้ทำการเตรียมดีบุกออกไซด์เช่นเซอร์โดยวิธีบดผสม ปริมาณสารโด๊ปที่เติมอยู่ระหว่าง 0.3-1.0 wt% หลังจากนั้นนำชิ้นงานไปเผาในบรรยากาศปกติและ N_2 ที่อุณหภูมิ 1000 องศาเซลเซียส ทำการศึกษาโครงสร้างเฟสโดยใช้เทคนิค X-ray diffraction (XRD) ศึกษา oxidation state ของดีบุกออกไซด์โดยเทคนิค X-ray photoelectron spectroscopy (XPS) และ Ultra-violet photoelectron spectroscopy (UPS) และศึกษาโครงสร้างจุลภาคโดยใช้เทคนิค Scanning electron microscope (SEM) และ Transmission electron microscope (TEM) จากผลการวิเคราะห์โดยใช้เทคนิค XRD พบว่าชิ้นงานตัวอย่างดีบุกออกไซด์มีลักษณะโครงสร้างเฟสเป็นแบบ cassiterite จากการวิเคราะห์โดยใช้เทคนิค XPS พบว่าดีบุกออกไซด์มีเลขออกซิเดชันเป็น +4 และ/หรือ +2 และจากผลการวิเคราะห์โดยเทคนิค SEM และ TEM พบว่าโครงสร้างทางจุลภาคของชิ้นงานมีลักษณะโครงสร้างพรุนตัว โดยมีรูพรุนกระจายตัวอยู่ทั่วไป และทำการศึกษาความสามารถในการตอบสนองแก๊สไอโซบิวเทนที่อุณหภูมิ 300-400 องศาเซลเซียส พบว่าเมื่ออุณหภูมิในการทำงานสูงขึ้น ความสามารถในการตอบสนองต่อแก๊สสูงขึ้นด้วย ผลของบรรยากาศในการเผาพบว่าชิ้นงานที่เผาในบรรยากาศปกติแสดงความสามารถในการตอบสนองต่อแก๊สได้ดีกว่าชิ้นงานที่เผาในบรรยากาศ N_2 และปริมาณสารโด๊ปที่ 0.8 wt% เผาในบรรยากาศปกติให้ความสามารถในการตอบสนองต่อแก๊สดีที่สุดใน

ภาควิชา วัสดุศาสตร์

สาขาวิชา เทคโนโลยีเซรามิก

ปีการศึกษา 2546

ลายมือชื่อนิสิต.....

ลายมือชื่ออาจารย์ที่ปรึกษา.....

ลายมือชื่ออาจารย์ที่ปรึกษาร่วม.....

##4472508923: MAJOR CERAMIC TECHNOLOGY

KEYWORDS: STANNIC OXIDE SENSOR/ MICROSTRUCTURE/SURFACE ANALYSIS/Sb-SnO₂
 UTOOMPORN KORKERD: EFFECTS OF MICROSTRUCTURE OF SINTERED TIN
 OXIDE ON GAS-SENSING SENSITIVITY. THESIS ADVISOR: ASSOCIATE
 PROFESSOR SUPATRA JINAWATH, CO-ADVISOR: Dr. APINYA PANUPAT, 94 pp.
 ISBN 974-17-4325-4

Tin oxide (SnO₂) gas sensor is a widely used material for gas sensor applications, its response being a change in conductance on exposure to oxidising or reducing gas. SnO₂ based sensors are of particular interest due to their high sensitivity at relative low operating temperature. In this study, influences of the microstructure of sintered tin oxide on gas sensitivity and the influences of dopant concentration on the electronic structure and sensitivity to iso-butane of sintered SnO₂ gas sensors are investigated. Sb-doped SnO₂ gas sensors were prepared by a conventional mixed oxide method. SnO₂ was doped with various concentration of Sb₂O₃ (0.3-1.0wt%) and sintered in air or in N₂ atmosphere. Structural and morphological changes of the samples were characterized by X-ray diffraction study (XRD), scanning electron microscopy (SEM) and transmission electron microscopy (TEM). XRD study reveals that sintered Sb-SnO₂ contains a cassiterite phase. SEM and TEM investigations of the samples sintered in air and N₂ atmosphere show porous polycrystalline structure with grain size ranging from 50-300 nm. X-ray photoelectron spectroscopy (XPS) analysis was carried out in order to investigate the oxidation states of Sn and Sb in the system and the Fermi level of Sb-doped SnO₂. Ultraviolet photoelectron spectroscopy (UPS) study was used to investigate the valence state of Sb-SnO₂. From the XPS analysis, the splitting of Sn 3d peak cannot be observed and thus suggesting that the oxidation state of Sb-doped SnO₂ is 4⁺ and/or 2⁺. Gas sensitivity are measured at temperature range of 300-400°C as iso-butane vapor is introduced into flowing dry air and correlated with the response time of gas-sensor. It was found that the gas sensitivity increases with the operating temperature and SnO₂ doped with 0.8wt% Sb₂O₃ sintered in air exhibits the highest sensitivity to iso-butane.

Department MATERIALS SCIENCE Student's signature.....

Field of study CERAMIC TECHNOLOGY Advisor's signature.....

Academic year 2003 Co-Advisor's signature.....

ACKNOWLEDGEMENTS

I would like to express deep gratitude to my advisor, Associate Professor Dr. Supatra Jinawath, for her encouragement and consistent guidance. Most of all, gratefully thank my co-advisor, Dr. Apinya Panupat, for giving me a good advice and inspiration. My work would not be completed without her helpful and invaluable suggestions.

I would like to thank the National Metal and Materials Technology Center (MTEC) and the National Synchrotron Research Center (NSRC) for providing laboratory facilities and support, and I also would like to thank Thailand Graduate Institute of Science and Technology (TGIST) for the financial support.

Many thanks also go to all my friends at the Department of Materials Science for their friendship and supports. In addition, I am also grateful to thank to Mr. Ekachai Klansorn for understanding and supports.

Finally, I would like to express my gratitude to my family for their love, understanding and encouragement throughout my study.

สถาบันวิทยบริการ
จุฬาลงกรณ์มหาวิทยาลัย

CONTENTS

| | Page |
|---|-------------|
| ABSTRACT (THAI)..... | iv |
| ABSTRACT (ENGLISH)..... | v |
| ACKNOWLEDGEMENT..... | vi |
| CONTENTS..... | vii |
| LIST OF TABLES..... | x |
| LIST OF FIGURES..... | xi |
| CHAPTER | |
| I INTRODUCTION..... | 1 |
| 1.1 Application and technology of gas sensor..... | 1 |
| 1.2 Material of interest..... | 2 |
| 1.3 Objective of this study..... | 3 |
| II LITERATURE REVIEWS..... | 4 |
| 2.1 Introduction..... | 4 |
| 2.2 Fundamental characteristic of stannic oxide gas sensor..... | 5 |
| 2.2.1 Crystal structure of stannic oxide..... | 5 |
| 2.2.2 Electrical properties of stannic oxide..... | 5 |
| 2.3 The mechanism underlying sensitivity..... | 6 |
| 2.3.1 The surface oxidation of combustible gas..... | 6 |
| 2.3.2 Gas sensitivity..... | 7 |
| 2.3.3 The mechanism of conductance change..... | 8 |
| 2.4 Sensitivity modification using catalysts and additive..... | 15 |
| 2.5 Fabrication of stannic oxide gas sensor..... | 17 |
| 2.6 Summary..... | 18 |
| III Experimental procedures..... | 19 |
| 3.1 Raw materials..... | 19 |
| 3.2 Methodology..... | 20 |
| 3.3 Material characterization..... | 21 |
| 3.3.1 Particle size and particle size distribution..... | 21 |
| 3.3.1.1 Principles of the technique..... | 21 |

CONTENTS (continued)

| CHAPTER | Page |
|---|-----------|
| 3.3.1.2 Experimental details..... | 23 |
| 3.3.2 Phase determination | 23 |
| 3.3.2.1 Principle of the X-Ray Diffraction technique..... | 23 |
| 3.3.2.2 Experimental details of X-ray diffraction analysis..... | 24 |
| 3.3.3 Porosity determination..... | 25 |
| 3.3.3.1 Principle of the technique..... | 25 |
| 3.3.4 Microstructure characterizations..... | 26 |
| 3.3.4.1 Principle of scanning electron microscopy..... | 26 |
| 3.3.4.2 Experimental details of SEM analysis..... | 28 |
| 3.3.4.3 Principle of transmission electron microscope..... | 28 |
| 3.3.4.4 Experimental details of TEM analysis..... | 30 |
| 3.3.5 Surface analysis..... | 30 |
| 3.3.5.1 Principle of X-ray photoelectron spectroscopy..... | 30 |
| 3.3.5.2 Experimental details of XPS analysis..... | 33 |
| 3.3.5.3 Principle of Ultraviolet photoelectron spectroscopy.... | 33 |
| 3.3.5.4 Experimental details of UPS analysis..... | 33 |
| 3.4 Conductivity Measurement..... | 35 |
| IV RESULTS AND DISSCUSSION..... | 38 |
| 4.1 Particle size and particle size distribution..... | 38 |
| 4.2 Physical properties of tin oxide sensor..... | 42 |
| 4.2.1 XRD analysis of crystal phase..... | 42 |
| 4.2.2 Microstructure..... | 47 |
| 4.3 Effect of sintering atmosphere on the microstructure | 49 |
| of tin oxide gas sensor | |
| 4.4 Effect of antimony oxide dopant concentration on the | 56 |
| microstructure of tin oxide gas sensor | |
| 4.5 Effect of binder concentration on the microstructure | 58 |
| of tin oxide sensor | |
| 4.6 Effect of sintering atmosphere on the gas sensitivity..... | 62 |

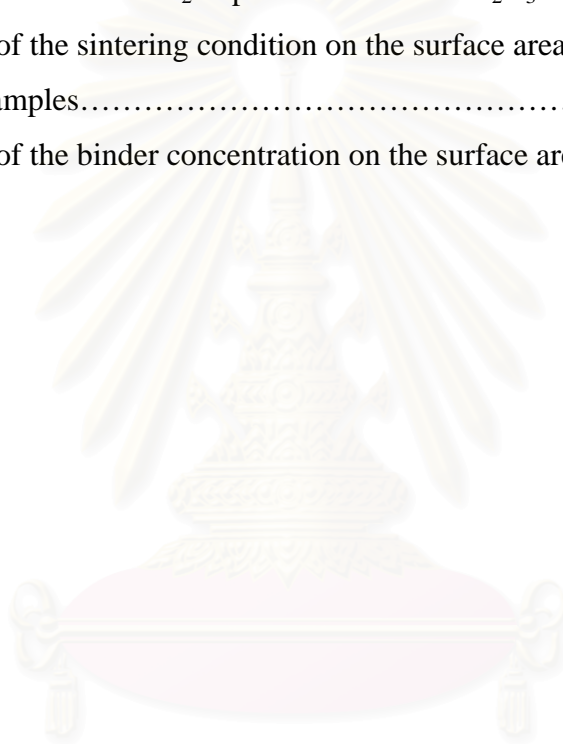
CONTENTS (continued)

| CHAPTER | Page |
|--|------|
| 4.7 Effect of antimony oxide dopant concentration on..... | 63 |
| the gas sensitivity | |
| 4.8 Effect of binder concentration on the gas sensitivity..... | 69 |
| 4.9 Effect of thickness of SnO ₂ sensor on gas sensitivity..... | 70 |
| 4.10 Surface analysis..... | 71 |
| 4.10.1 XPS analysis..... | 71 |
| 4.10.2 UPS analysis..... | 76 |
| V CONCLUSIONS AND RECOMMENDATION..... | 79 |
| 5.1 Conclusions..... | 79 |
| 5.2 Recommendation..... | 79 |
| REFERENCES..... | 80 |
| APPENDICES..... | 83 |
| APPENDIX A | 84 |
| APPENDIX B..... | 85 |
| APPENDIX C..... | 86 |
| APPENDIX D..... | 87 |
| APPENDIX E..... | 88 |
| APPENDIX F..... | 90 |
| APPENDIX G..... | 91 |
| VITA..... | 92 |

สถาบันวิทยบริการ
จุฬาลงกรณ์มหาวิทยาลัย

LIST OF TABLES

| Table | | Page |
|--------------|--|-------------|
| 3.1 | Chemicals used in preparation of gas sensor elements..... | 19 |
| 3.2 | Comparion of XPS and UPS techniques..... | 33 |
| 4.1 | XRD data of raw materials, mixed powder before sintering and after sintering in air and N ₂ from JCPDS file..... | 44 |
| 4.2 | The composition of SnO ₂ doped with 0.5wt% Sb ₂ O ₃ from EDS analysis..... | 47 |
| 4.3 | Influence of the sintering condition on the surface area and grain size of SnO ₂ samples..... | 50 |
| 4.4 | Influence of the binder concentration on the surface area of SnO ₂ samples... | 60 |



สถาบันวิทยบริการ
จุฬาลงกรณ์มหาวิทยาลัย

LIST OF FIGURES

| Figure | Page |
|---|------|
| 2.1 Unit cell of the crystalline structure of SnO ₂ | 5 |
| 2.2 Possible scheme of CO oxidation on SnO _{2-x} | 8 |
| 2.3 Band diagram for SnO _{2-x} with negatively charged adsorbed oxygen..... | 9 |
| 2.4 Model of inter-grain potential barrier (in the absence of air)..... | 10 |
| 2.5 Model of inter-grain potential barrier (in the absence of gases)..... | 11 |
| 2.6 Three models for conductance limited by intergrain constriction..... | 12 |
| 2.7 A gas sensing element of the directly heated SnO ₂ ceramic type..... | 17 |
| 2.8 A gas sensing element of the indirectly heated SnO ₂ ceramic type..... | 18 |
| 3.1 Flow diagram of sample preparation of ceramics gas sensor by a conventional oxide mixing process..... | 20 |
| 3.2 Schematic diagram of the Mastersizer system for measuring particle size and particle size distribution..... | 22 |
| 3.3 XRD measurement..... | 24 |
| 3.4 Basic principles of the scanning electron microscope..... | 27 |
| 3.5 Schematic diagram showing the basic principles of the scanning electron microscope..... | 28 |
| 3.6 Schematic diagram showing the basic principles of the transmission electron microscope..... | 29 |
| 3.7 Energy-level diagram showing the electron transitions that form the basic for X-ray photoelectron spectroscope..... | 31 |
| 3.8 X-ray Photoelectron Spectrometer at Siam Photon Laboratory..... | 32 |
| 3.9 Energy-level diagram showing the electron transitions that form the basic for ultraviolet photoelectron spectroscope..... | 34 |
| 3.10 Gas sensor test system..... | 36 |
| 3.11 SnO ₂ is in contact with platinum electrode in the gas chamber system..... | 37 |
| 4.1 Cumulative and size distribution of SnO ₂ powder..... | 41 |
| 4.2 Cumulative and size distribution of Sb ₂ O ₃ powder..... | 41 |
| 4.3 Cumulative and size distribution of SnO ₂ powder added 0.3 wt % Sb ₂ O ₃ powder dopant..... | 41 |

LIST OF FIGURES (continued)

| Figure | Page |
|--|-------------|
| 4.4 XRD patterns of received raw materials and stannic oxide powder doped with 0.3 wt% Sb_2O_3 before sintering and after sintering in air and in N_2 | 43 |
| 4.5 EDX spectrum of SnO_2 doped with 0.5wt% Sb_2O_3 sintered in air..... | 46 |
| 4.6 SEM micrograph of SnO_2 raw material..... | 48 |
| 4.7 SEM micrograph of Sb_2O_3 raw material..... | 48 |
| 4.8 SEM micrographs of SnO_2 doped with 1.0 wt% Sb_2O_3 pellets..... | 51 |
| 4.9 TEM micrographs of SnO_2 doped with 1.0 wt% Sb_2O_3 | 53 |
| 4.10 EDX analysis which show the comparison of EDX spectra taken from the grain and grain boundary of sample doped with 0.5 wt% Sb_2O_3 , sintered in air..... | 54 |
| 4.11 EDX analysis which show the comparison of EDX spectra taken from the grain and grain boundary of 0.5 wt% Sb_2O_3 -doped SnO_2 , sintered in N_2 | 55 |
| 4.12 SEM micrographs of SnO_2 doped with (a) 0.3 wt% Sb_2O_3 and (b) 0.5wt% Sb_2O_3 sintered in air at 1000 °C..... | 57 |
| 4.13 SEM micrographs of SnO_2 doped with 0.8 wt% Sb_2O_3 sintered in air at 1000°C..... | 59 |
| 4.14 SEM micrograph of SnO_2 doped with 0.8 wt% Sb_2O_3 sintered in N_2 at 1000°C..... | 61 |
| 4.15 Electrical response of SnO_2 doped with 0.3wt% Sb_2O_3 added with 3.0wt% PVA binder sintered in air and N_2 atmosphere at 1000°C for 1 hour..... | 62 |
| 4.16 Electrical response of SnO_2 doped with 0.3, 0.5 and 0.8 wt% Sb_2O_3 sintered in air at 1000°C for 1 hour..... | 64 |
| 4.17 Electrical response of SnO_2 doped with 1.0 wt% Sb_2O_3 sintered in air at 1000°C for 1 hour..... | 64 |
| 4.18 Sensitivity as a function of operating temperature of SnO_2 doped with 0.3, 0.5, 0.8 and 1.0 wt% Sb_2O_3 sintered in air and N_2 atmosphere at 1000°C for 1 hour..... | 65 |

LIST OF FIGURES (continued)

| Figure | Page |
|--|------|
| 4.19 Electrical response of SnO ₂ doped with 0.3, 0.5, 0.8 and 1.0 wt% Sb ₂ O ₃ sintered in N ₂ atmosphere at 1000°C for 1 hour..... | 68 |
| 4.20 Electrical response of SnO ₂ doped with 0.8wt% Sb ₂ O ₃ and added with various concentration of PVA binder sintered in air at 1000°C for 1 hour..... | 69 |
| 4.21 Electrical response of SnO ₂ doped with 0.8wt% Sb ₂ O ₃ , 1.0 mm and 2.0mm thickness, sintered in air at 1000°C for 1 hour..... | 70 |
| 4.22 XPS spectrum of SnO ₂ doped with 1.0wt% Sb ₂ O ₃ sintered in air at 1000°C... | 73 |
| 4.23 XPS spectrum of SnO ₂ doped with 1.0wt% Sb ₂ O ₃ sintered in N ₂ at 1000°C... | 74 |
| 4.24 XPS spectra of Sn 3d peak of SnO ₂ doped with 1.0wt% Sb ₂ O ₃ sintered in air and N ₂ atmosphere at 1000°C..... | 75 |
| 4.25 XPS spectra of Sn 3d5/2 line..... | 75 |
| 4.26 UPS spectra of SnO ₂ which is undoped and doped with 1.0wt% Sb ₂ O ₃ sintered in air and N ₂ | 77 |

CHAPTER 1

INTRODUCTION

1.1 Applications and technology of gas sensor

Gas sensors are required for domestic, automotive and industrial applications due to the implication of gases in environmental control or dangerous emissions. So, major reasons for the need of gas sensors are monitoring of environmental pollutants and controlling their emission. At this respect, the market, based on the new regulations, demands a higher reliability in domestic and environmental gas sensors for the detection of combustible and toxic gases. For gas monitoring, different kinds of sensor systems can be used: Spectroscopic, Optical and Solid State are the three main families of gas sensors. Spectroscopic systems are those based on the direct analysis of fundamental gas properties, such as molecular mass or vibrational spectrum; optical sensor systems are based on the measurement of the absorption spectra after light stimulation; and solid-state ones are based on the change of physical and/or chemical properties of a sensing material after gas exposure. These last changes depend on the gas sensing material and usually involve changes in its electrical properties.

Metal oxide based sensors have been used extensively for chemical and gas detection, which include toxic and pollution gases (CO , H_2S , Cl_2 , NO_x , SO_2 , CO_2 , etc.) and combustible gas (H_2 , CH_4 and flammable organic vapors). Many metal oxide materials, such as ZnO , TiO_2 , SnO_2 , WO_3 , Ga_2O_3 , have been examined for gas sensing application.

Stannic oxide (tin dioxide, SnO_2) gas sensor is a widely used material for gas sensor application, its response being a change in conductance on exposure to oxidising or reducing gas¹. It is used under various form, as sintered pellets and “thick” or “thin” film. To improve selectivity and sensitivity, the oxide is doped with various cations (e.g. Al, Cu, In, Sb), or modified with elements (e.g. Au, Pd, Pt) that exert a catalytic effect². A chemical reaction between oxygen and the combustible gases occurs at the surface of the solid, leading to a change in conductance brought about through a change in charge-carrier concentration, namely electrons.

1.2 Material of interest

Tin oxide has recently received a great scientific interest because of its wide range of applications. It has been studied as overcoat for thin film magnetic recording media overcoat, as transparent electrode in panels and other electronic devices, and also in photoelectrochemical studies and those related to the development of solar cells³⁻⁸. Efficiency in these applications is usually improved by suitably doping the tin oxide substrate but, once doped, newer applications are also reported, as for example doping with Sb, Cl and F increases the conductivity of tin oxide, while doped tin oxide deposited on titanium presents high overpotentials for the oxygen generation reaction, thereby giving good anodes for the electrochemical oxidation of both organic pollutants and cyanide⁹⁻¹¹. It is also investigated as material for Li-ion batteries¹²⁻¹⁴.

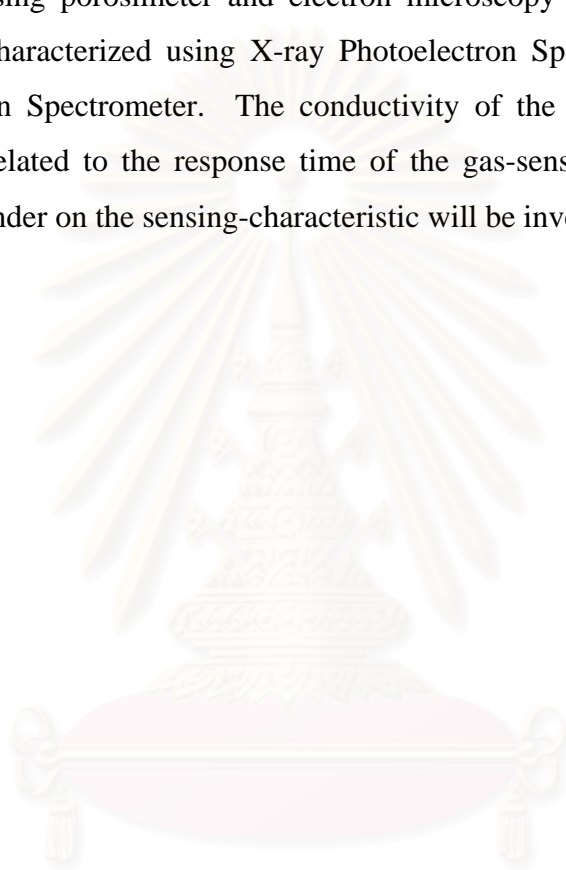
The study of SnO₂ as gas sensing material is due to its suitable physicochemical properties as, for example, it has a high reactivity to reducing gases at relatively low operating temperatures thanks to the easy adsorption of oxygen at its surface because of the natural non-stoichiometry of SnO₂. Moreover, SnO₂ has a lower cost when compared to actual available materials for similar applications. Nowadays, the research on these materials is focused to increase their sensitivity, selectivity and stability, and one of the main issues to accomplish these is the presence of metals at low concentrations. Thus, the present of a certain metal on the SnO₂ surface improves the properties of the material with respect to certain gases, which are different depending on the added metal. Moreover, the chemical state and the dispersion of the added metal on the SnO₂ surface also influence the gas sensing response of these materials.

Stannic oxide is “intrinsically” an n-type semiconductor, the evidence indicating the cause being non-stoichiometry arising through oxygen vacancies. The oxygen vacancies are charge-compensated by electrons, at low temperatures occupying n-type, donor state. The addition of Sb⁵⁺ state increases the electron concentration, just as the Pd dopant in Si does. The function of a gas sensor depends on redox reactions at the sensor surface. Therefore, the condition of the surface layer is of crucial importance. The chemistry of this layer can be quite different from that of

the bulk, and it can be modified in the sintering stage, almost certainly by the sintering atmosphere/temperature conditions.

1.3 Objective and the scope of this study

The proposed thesis is aimed to study the effects of microstructure on the response time of antimony-doped stannic oxide. The particle and pore structure will be characterized using porosimeter and electron microscopy studies. The surface structure will be characterized using X-ray Photoelectron Spectrometer and Ultra-violet Photoelectron Spectrometer. The conductivity of the samples will be then measured and correlated to the response time of the gas-sensor. Furthermore, the effect of organic binder on the sensing-characteristic will be investigated.



สถาบันวิทยบริการ
จุฬาลงกรณ์มหาวิทยาลัย

CHAPTER 2

LITERATURE REVIEW

In this chapter, the fundamental characteristics of stannic oxide gas sensor such as the physics of stannic oxide gas sensor, electrical properties of stannic oxide gas sensor and mechanisms underlying the sensitivity will be reviewed. Moreover, the fabrication of stannic oxide gas sensor and sensitivity modification using catalysts and additives will be discussed.

2.1 Introduction

Stannic oxide based gas sensors are of particular interest due to their high sensitivity at relatively low operating temperature. The first stannic oxide devices were based on a thick film or ceramic layer of stannic oxide¹⁵. Commercial devices are now available; they use the conductance variations of stannic oxide semiconductor for detecting low concentrations of flammable gases like CH₄, LPG and H₂ or toxic gases like CO, NO_x.

Nowadays, combustible hydrocarbon gases such as liquefied petroleum gas (LPG) are being widely used as a fuel for domestic heating and industrial use to provide a clean source of energy for burning. However, they are potentially hazardous due to high possibility of explosion accidents caused by leakage or by human error. This has resulted in an increasing demand to develop sensors in order to detect these hydrocarbon gases. The term LPG is applied to those hydrocarbons, the chief component of which consists of butane (70-80%), propane (5-10%) and propylene, butylene, ethylene, methane (1-5%). In order to meet the high standards set for detection and the sensing of low levels of gases, the sensor should be upgraded in terms of sensitivity, selectivity, reproducibility and stability.

2.2 Fundamental characteristics of stannic oxide gas sensor

2.2.1 Crystal structure of stannic oxide

Tin dioxide is a semiconductor material, transparent, of high chemical and mechanical stability¹⁶. Only one stable phase is known, which has a tetragonal arrangement of the atoms receiving the names of rutile or cassiterite.

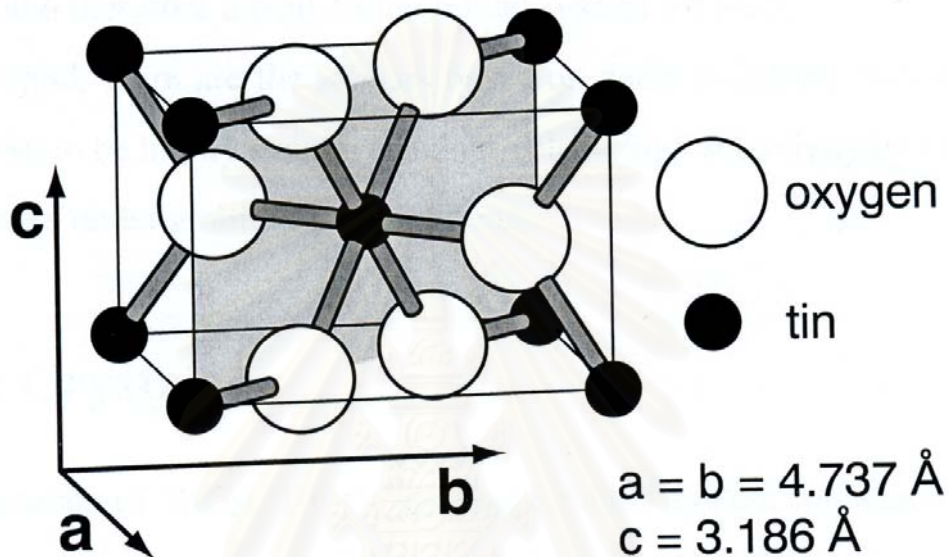


Figure 2.1 Unit cell of the crystalline structure of SnO_2 ¹⁷.

The corresponding heat of formation is $\Delta H = 1.9 \times 10^3 \text{ J mol}^{-1}$, the heat capacity of the material is $C_p = 52.59 \text{ J mol}^{-1} \text{ K}^{-1}$, the density at 300 K is 6.95 g cm^{-3} and the melting point is $1630 \text{ }^\circ\text{C}$. This crystalline structure contains metal atoms in octahedral coordination and oxygen in planar three-coordination (see Figure 2.1.). Lattice parameters are $a = 4.737 \text{ \AA}$ ($a = b$ in the tetragonal structure) and $c = 3.186 \text{ \AA}$ ¹⁸.

2.2.2 Electrical properties of stannic oxide gas sensor

Electrical properties of SnO_2 single crystals are, of course, the starting point for the understanding of the conductance response of sintered thick films and bulk type (the transducer function). SnO_2 is a semiconductor crystallizing in the rutile structure. Its tetragonal unit cell contains two tin and four oxygen atoms, as shown in

Figure 2.1. The structure is 6:3 coordinate and has a relatively strong ionic character¹⁹.

Stannic oxide in its pure form is an n-type wide band semiconductor. Its electrical conduction results from point defect which are negative (oxygen vacancies) or foreign atoms that act as donors or acceptors (traps). Some unique properties of SnO₂ such as electrical and optical properties, make it useful for many applications, like for gas detection.

The conductivity of SnO₂ single crystals is not always homogeneous through the crystal. Samson and Fonstad²⁰ have found, as also Negasawa and Shionoya²¹ that heat treated crystal (especially under high oxygen pressure) have high resistivity surface layer (five or more orders of magnitude higher than the bulk resistivity). Studies in ultrahigh vacuum (< 10⁻⁹ Torr) by Semancik and Fryberger²², on the other hand, have shown that the conductivity of the near-surface region of SnO₂ single crystals can be enhanced by three orders of magnitude when compared with the bulk material.

The gas sensitivity S_G of a sensor is commonly defined as the ratio of its resistance in air R_a to that in gas R_s .

$$S_G = \frac{R_a - R_s}{R_a} \quad (\text{Eq. 2.1})$$

2.3 The Mechanisms underlying sensitivity

2.3.1 The Surface oxidation of combustible gases

It is well-known that in clean air, oxygen chemisorbs (that is, chemically adsorbs) onto the surface of a metal oxide catalyst and removes electrons from the conduction or valence band depending upon whether the oxide is n-type or p-type, so that its resistivity will either rise or fall. In the case of stannic oxide, which is an n-type semiconductor, electrons are removed from the conduction band, leading to a rise in resistivity. Then, when a combustible gas subsequently chemisorbs onto the surface, it is oxidized by the oxygen already there, so reinjecting the electrons and

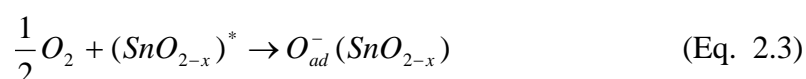
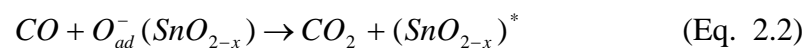
decreasing the resistivity as catalysis proceeds. The experimental results to confirm this has been reported as follows²³.

1. The high resistance condition of the ceramic depends upon adsorbed oxygen.
2. The catalytic oxidation of isobutane occurs at the ceramic surface, leading to the removal of adsorbed oxygen and also lattice oxygen in the surface.
3. The resistance of the ceramic decreases as its adsorbed oxygen is removed.

2.3.2 Gas sensitivity

Simplistically, it might be thought that the fall in resistance of a stannic oxide ceramic sensor in the presence of combustible gas could be explained as follows: Initially, the resistance is high because the oxygen ion species on the surface have been negatively charged by receiving electrons from the crystal. Then, when a combustible gas comes into contact with these adsorbed oxygen species, it reacts with them to form such products as CO_2 and H_2O ²⁴. It could then be assumed that electrons are returned to the crystal surfaces and grain boundaries and, hence, decrease the resistance.

Figure 2.2 illustrates a mechanism which involves a reaction cycle consisting of the catalytic oxidation of a gas (carbon monoxide in this illustrative case) on the surface resulting in the consumption of adsorbed surface oxygen. This is followed by replacement of the oxygen from the surrounding air²⁵. The equilibrium density of the adsorbed surface oxygen with the concentration of ambient gas would then define the sensor resistance.



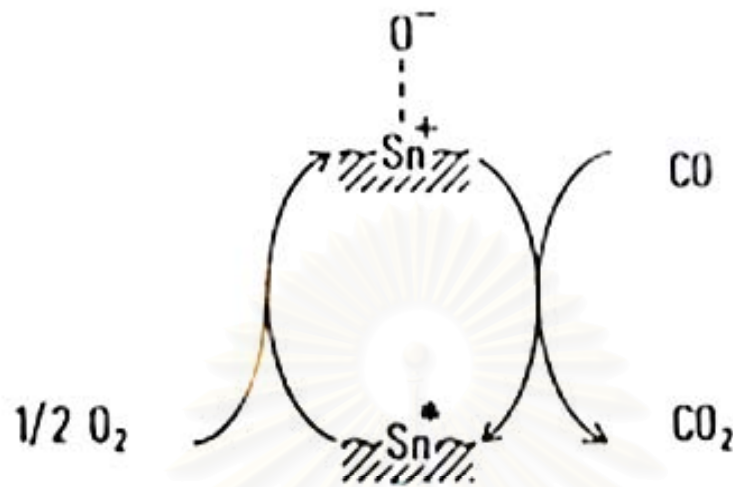


Figure 2.2 Possible scheme of CO oxidation on SnO_{2-x} .

Oxygen atom received electrons from SnO_{2-x} crystal and changes to oxygen ion adsorb on the surface, resistance is high. Then, when a combustible gas comes into the surface and reacts with oxygen ion, CO_2 and H_2O are produced and electron are returned to the crystal surface and grain boundaries, hence resistance is decreased.

2.3.3 Mechanism of conductance change

The stannic oxide crystal is fundamentally an n-type semiconductor containing oxygen lattice defects which act as electron donor²⁶. When oxygen atoms remove electrons from the donor near the surface to become adsorbed as negative ion, a space charge layer is formed, along with a concomitant adsorbed oxygen. The relevant energy band diagram is given in Figure 2.3, and the concept may be extended to give a potential barrier diagram between grain boundaries as shown in Figure 2.4-2.5.

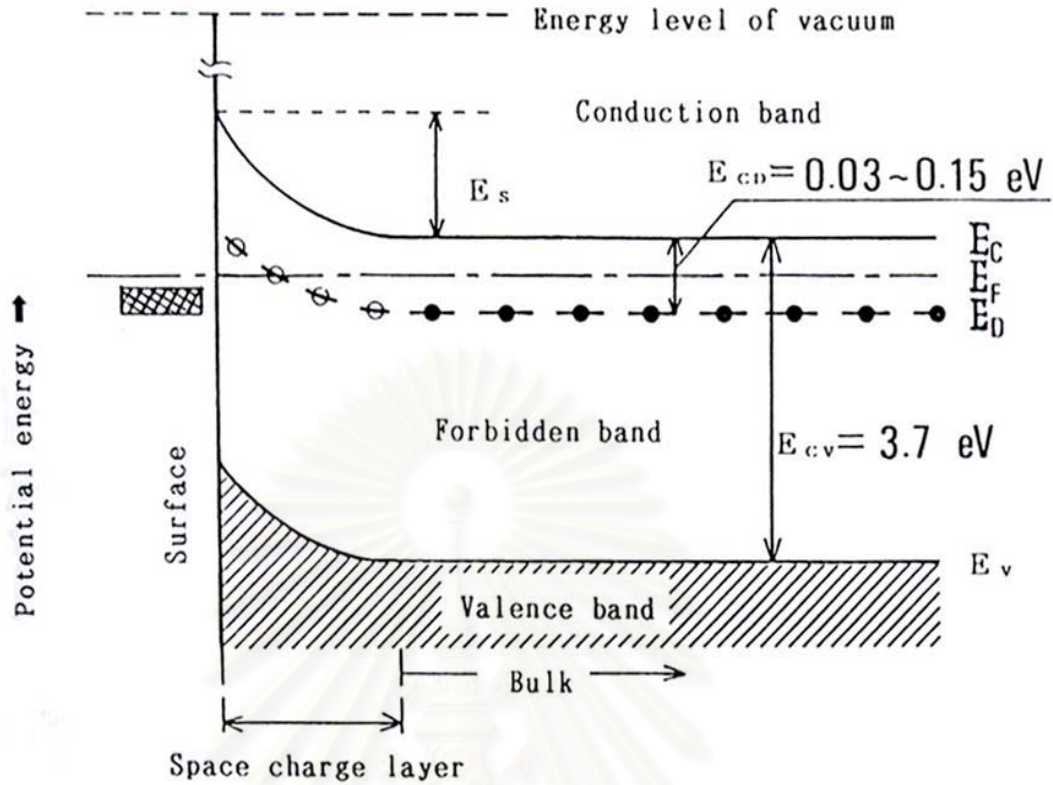
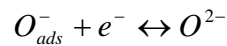


Figure 2.3: Band diagram for SnO_{2-x} with negatively charged adsorbed oxygen²⁷. Surface potential is caused by adsorbed O_2^- or O^- from the reactions ($\text{O}_2 + e \leftrightarrow \text{O}_{2ad}^-$ or $\frac{1}{2}\text{O}_2 + e \leftrightarrow \text{O}_{ad}^-$). E_s : potential barrier; E_F : Fermi level; E_D : donor level; E_C : lowest level of conduction band; E_V : highest level of valence band; E_{CD} : depth of donor level; E_{CV} : energy gap between E_C and E_D .

The donor states are usually associated with the oxygen bulk vacancies. The first step of the sensing mechanism is the "sensitizing" chemisorption of oxygen. The oxygen molecules are adsorbed in various sites on the tin dioxide surface:



As in the SnO_2 lattice, the oxygen appears as O^{2-} , the oxygen adsorption creates surface acceptor states O/O^- and O^-/O^{2-} on which conduction electrons will be trapped. This electronic states are placed on the band diagram below the Fermi level (Figure 2.3)



Further on, it will also be assumed that two conduction electrons are trapped on all the adsorbed oxygen species, in other words that all chemisorbed oxygen from the SnO_2 surface became O^{2-} ions. The effect of the reducing gas is to reduce the chemisorbed oxygen. As a consequence, the surface net charge is lowered and the trapped electrons are released back to the conduction band. The reaction corresponding to this process is:



where R = reducing gas

The operation principle of the SnO_2 sensor is shown in Figure 2.4 and 2.5. When SnO_2 is heated at a certain high temperature in air, oxygen is adsorbed on the crystal surface with a negative charge. Then donor electrons in the crystal surface are transferred to the adsorbed oxygen, resulting in leaving positive charges in a space charge layer. Thus, surface potential is formed to serve as a potential barrier against electron flow (Figure 2.4).

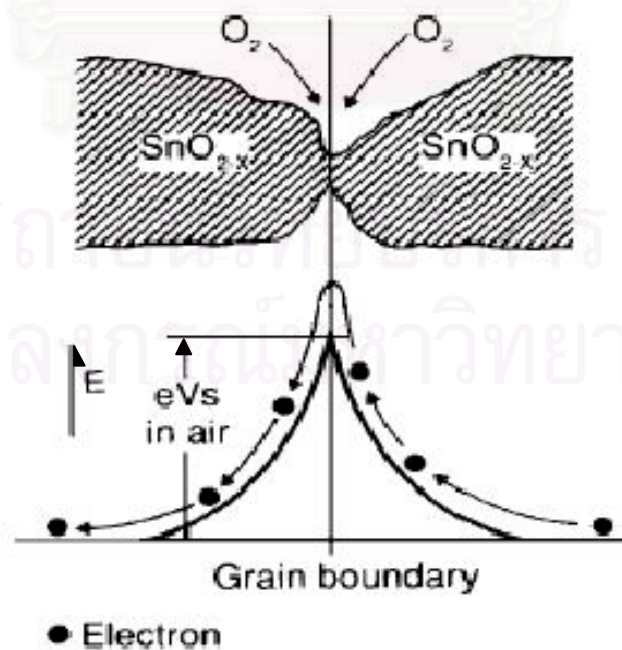


Figure 2.4 Model of inter-grain potential barrier (in the absence of air)²⁷.

Inside the sensor, electric current flows through the conjunction parts (grain boundary) of SnO₂ micro crystals. At grain boundaries, adsorbed oxygen forms a potential barrier which prevents carriers from moving freely. The electrical resistance of the sensor is attributed to this potential barrier. In the presence of a reducing gas, the surface density of the negatively charged oxygen decreases, so the barrier height in the grain boundary is reduced (Figure 2.5). The reduced barrier height decreases sensor resistance. The relationship between sensor resistance and the concentration of reducing gas can be expressed by the following equation over a certain range of gas

concentration:

$$R_s = A[C]^{-a}$$

where: R_s = electrical resistance of the sensor

A = constant

$[C]$ = gas concentration

a = slope of R_s curve

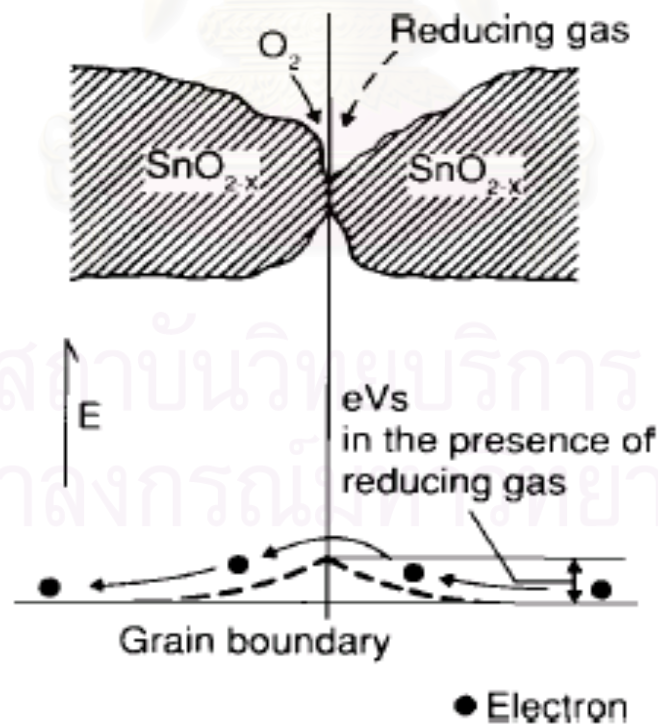


Figure 2.5 Model of inter-grain potential barrier (in the presence of gases).

From Figure 2.4 and 2.5, it can be suggested that in air condition the density of the negative adsorbed oxygen ions is large, the potential barrier is high, resulting in a high resistance. In reducing gas, the density of negative adsorbed oxygen ions is reduced. By the presence of combustible gas, the potential barrier falls, as resistance decreased.

Consideration of the mechanism of conduction by porous ceramic sensor need to take account of the structural inhomogeneity, which implies lower resistance paths through the bulk of crystallites alternating with higher resistance constrictions at the point of contact²⁸.

Three general cases may be considered and in each of them the depletion layer represents a substantial fraction of the material comprising the intergrain contact²⁹. The different case imply different dependences of conductance activation energy on the partial pressure of oxygen and of the combustible gas.

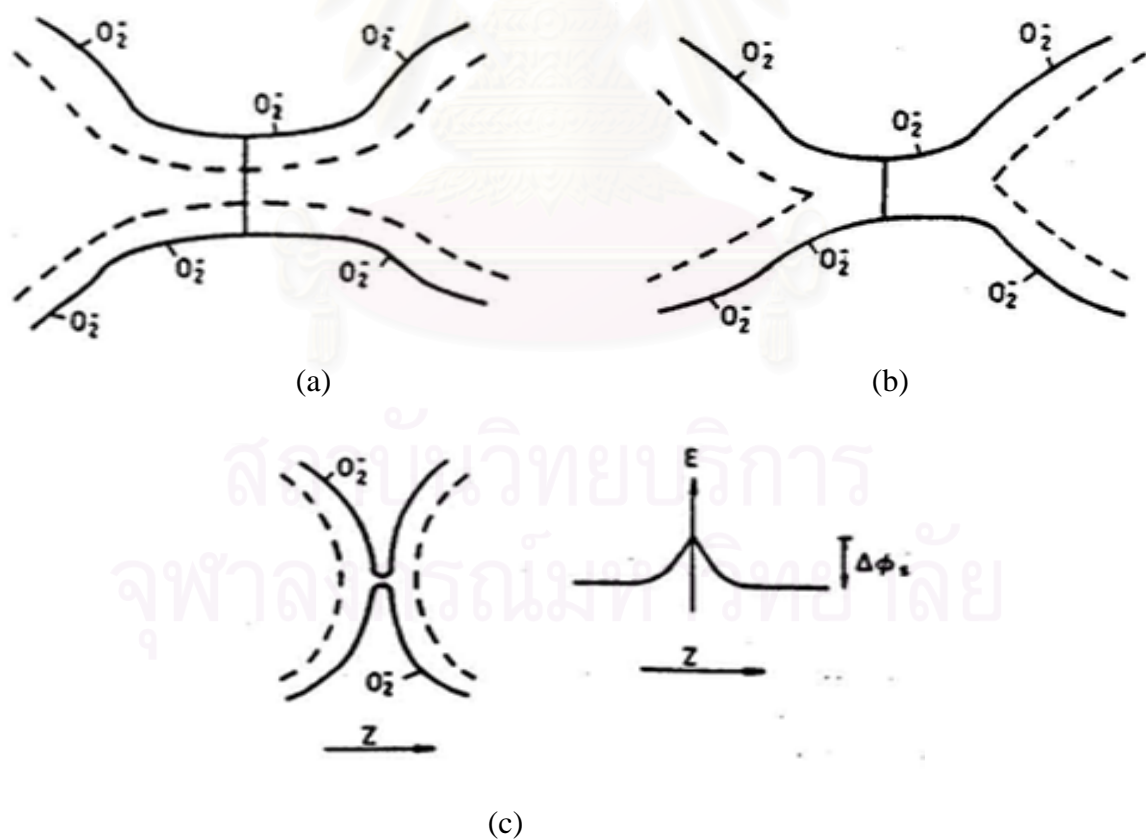


Figure 2.6 Three models for conductance limited by intergrain constriction, (a) open neck, (b) close neck, (c) porous ceramic.

Figure 2.6 (a) shows the well-sintered case with a fully open ‘neck’ between adjacent grains. Surface states (here drawn as O_2^-) cause a depletion zone extending to a depth marked by the dashed line on both sides of the neck. In this case, the conductivity would be largely that of the undepleted layer in the centre of the neck. The conductance would be determined by activation of electrons from donor states in the bulk (bulk-trap-limited regime), activation energy E_D , and would be affected by gaseous atmosphere through changes in the effective width of the channel only.

Figure 2.6 (b) shows the case of a ‘close’ neck where the depletion zones from the two surface overlap, leaving a higher resistance ohmic path through the centre. This geometry can arise because less complete sintering by alterations in the composition of the atmosphere, causing a change in the depletion layer thickness.

In this case, the conductance in the neck would be determined by activation of electron from surface states into the conduction band (surface-trap-limited regime), activation energy E_S , and would be directly affected by the influence of the gaseous atmosphere on the occupancy of the surface states. The transition from open to constricted necks is analogous to the operation of a field-effect transistor: under circumstances where the depletion length is comparable to the channel width, the conductance becomes very sensitive indeed to variations in the surface charge³⁰.

The situations depicted in Figure 2.6 (a) and (b) imply that a porous body would respond in the same way as a thin film gas sensor. Figure 2.6 (c) shows a third situation applicable in a porous mass, but not in a thin film sensor. Within the two grains shown there is ohmic behavior but at the point of contact a schottky barrier forms, arising out of charge trapped in the surface states. In this case, conductivity would be limited by charge transport across the barrier and would be

$$\sigma \sim (const.) \exp(-e\Delta\phi_s / kT) \quad (\text{Eq.2.4})$$

where σ = electrical conductivity
 e = electron
 $\Delta\phi_s$ = potential barrier
 k = Boltzmann's constant
 T = temperature (K)

The situation occurs as a limiting case as the necks between the grains get shorter and narrower and it gives effects on the conductance which are, in principle, distinctly different from the two other cases. For example, the activation energy for conductance would be $e\Delta\phi_s$. It would be directly affected by the charge and fractional coverage of the surface species and hence a function of the composition of the gaseous atmosphere.

It should also be noted that each of the three cases illustrated in Figure 2.6 contains a grain boundary across the contact. Grain boundary trapping states can themselves establish a depletion layer around the boundary. If the grain size was small enough, then the grains might be depleted of conduction electrons, resulting in a conductance limited by excitation from grain boundary traps³¹.

If the electrical resistance of barrier-type contacts is much greater than that of neck-type contacts, then it becomes interesting to consider the consequence of the following theoretical argument. In a three-dimensional mass, in which each crystallite is contacted to several neighbours by contacts which may be either 'neck' or 'barrier', there will exist a percolation limit pertaining to the proportion of contacts which are barriers. If the proportion is higher than the limit, then current carriers must necessarily cross a barrier somewhere. With a proportion of barriers greater than the limit, an effective domain size can be defined, which is a function of the proportion of barrier.

In a porous body, a second sort of percolation limit exists, determined by the access of the gas phase to all parts of the interior of the body: not all of the interior of a porous mass may be easily accessible to a gas. The effect of closed porosity, or of

extremely fine porosity, might also be to define domains, such that the gas sensitivity of conductance arises from connections between domains.

Both of these considerations (percolation of the charge carriers and percolation of the gas phase) imply that, if the microstructure is not stable (for example, if thermal expansions and contractions, or reactions with moisture at the elevated temperature of operation cause interparticle contacts either to break or to sinter further), then the effective domain size will change with time and an ‘aging’ of the sensor will be observed.

Finally, in this discussion, the possibility of effects due to a Schottky barrier formed at the contact with the metal electrodes should also be noted. There is certainly the possibility that some gas response may arise simply as a result of the modulation of the contact barrier³².

2.4 Sensitivity modification using catalysts and additives

Semiconductor gas sensors are normally operated at constant temperatures above about 300°C obtained by connecting a constant voltage over a heating resistor intergrated into the sensor construction. In this mode of operation, the sensors are sensitive to a wide range of gases, including CO, NO_x and many organic and vapours³³⁻³⁴. Besides these gases, the sensors are sensitive to variation in the ambient humidity. Various approaches, such as the use of different sensing materials and catalysts, thermal treatments of the sensing material, variation of the thickness of the gas-sensing layer and various particle sizes and dopants on SnO₂-based gas sensors have been used to improve selectivity³⁵⁻³⁷.

A semiconductor material like SnO₂ in sensors serves as the catalyst for many chemical reaction. The reactions with semiconductor sensors used in air are primarily oxidation reactions, where a reducing agent in the atmosphere reacts with an oxygen species (including the lattice oxygen) on the surface of the semiconductor or its catalyst. The central role of the Fermi level E_F in heterogeneous catalysis on semiconductor surfaces is discussed below.

On the basis of the central role of the Fermi level for both the catalytic activity and the electrical properties of a semiconductor, it is possible to understand the relationship between catalytic activity and electrical conductivity. Thus the many “impurities”, broadly mean foreign atoms or local imperfections in the lattice or on the surface which may shift the Fermi level at the surface of the crystal, may influence both the catalytic activity and electrical conductivity of the sample. Thus, they may act as promoters for catalytic reactions. A donor impurity (like Sb in SnO₂), for instance, moving the Fermi level upward, may behave as a promoter depending on the effect of the increase of E_F on the reaction rate. In the case of acceleration of the reaction (acceptor reaction), the donor impurity behaves as a promoter, while in the case of deceleration of the reaction (donor reaction), the donor impurity has hamper reaction.

The most popular supported catalysts in semiconductor gas sensors are noble metals (Pd, Pt, Au, Ag) which are used in order to increase both the selectivity and sensitivity. With Pd catalysts, for instance, CH₄ and aliphatic hydrocarbons are selectively detected at high temperature (400-450°C), on the other hand, CO detection is possible at low temperature (50°C)³⁸.

The influence of many different additives on the electronic structure of SnO₂ thin films to H₂ was described by Wei Liu³⁹, the kind of dopant Pd, Sb, Pt or In hardly changed the grain size of SnO₂ thin films within low doping amount, but they did change the Fermi level of SnO₂. The dopant Sb increased the Fermi level by ~ 0.25 eV, but In and Pd decreased it by ~0.2 eV and ~0.1 eV, respectively and Pt did not change the Fermi level. In another study by Shokr⁴⁰, the effect of antimony doping on the optical and electrical properties of the electron beam evaporated Sb-Sn-O films were studied. The result was, with increasing Sb content, the resistivity slightly decreased and then increased with further addition of Sb. Besides, the doping of Sb inside the SnO₂ lattice was associated with the increase in the film transmission at solar maximum wevelength and width of optical band gap; which was interpreted in terms of the interaction between the two oxidation states of antimony, Sb³⁺ and Sb⁵⁺ and increase of atomic bond energy, respectively.

There are many observations in sensitivity, response and recovery time of SnO₂ based thick-film sensor for H₂, CO, CH₄ and LPG⁴¹, the result is, Pd-doped sensors possesses better sensitivity for all the test gases. The response and recovery time of the Pd-doped sensor has been found to depend on type of gas and its concentration (up to 400 ppm). The response time is minimum for CO and maximum for H₂ while recovery time is maximum for LPG and approximately the same for H₂ and CO. In another study by Phani⁴², sensors based on SnO₂ doped with various palladium and aluminum silicate not only improved the sensitivity toward LPG but also the selectivity in the presence of CO and CH₄.

2.5 Fabrication of stannic oxide gas sensor

Two typical structures for stannic oxide ceramic gas sensors are shown in Figure 2.7 and Figure 2.8. The first is a directly heated type in which two heater coils are bonded inside the ceramic element itself. These separate heater coils also act as electrodes to detect changes in the conductance of the stannic oxide ceramic. The second is an indirectly heated type in which the single heater coil is separated from the ceramic by a tubular alumina substrate.

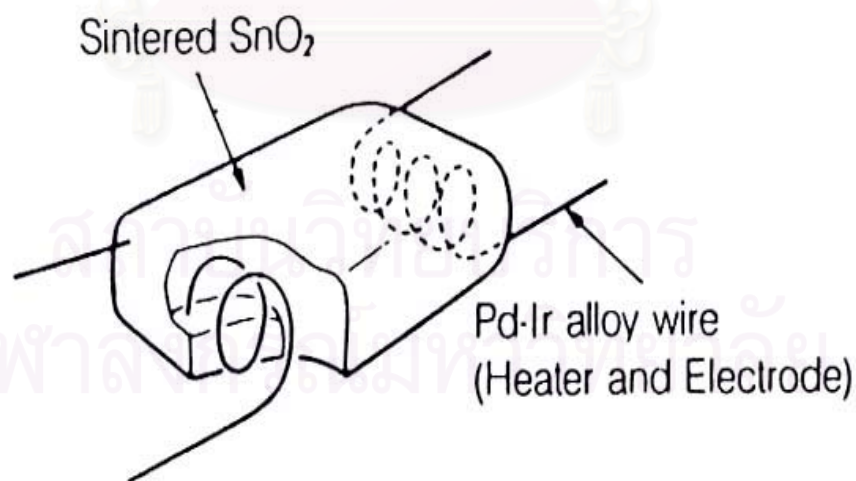


Figure 2.7 A gas sensing element of the directly heated SnO₂ ceramic type.⁴³

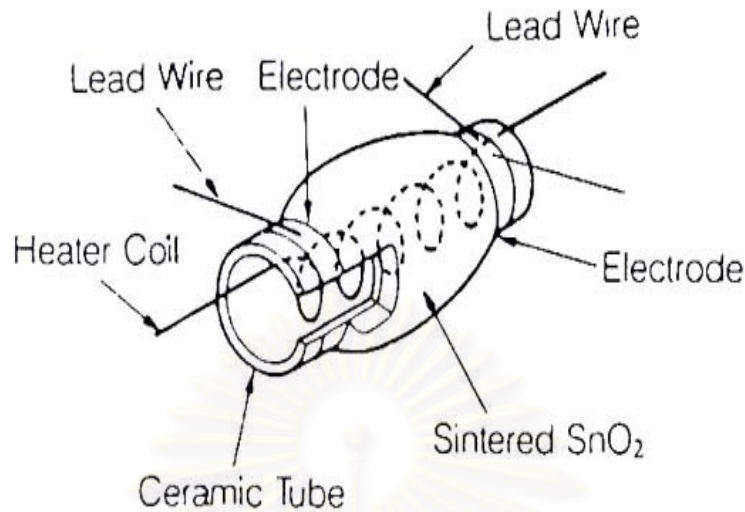


Figure 2.8 A gas sensing element of the indirectly heated SnO₂ ceramic type.⁴³

2.6 Summary

According to the above review, SnO₂ gas sensors has been used for detecting flammable gases such as CH₄, LPG and H₂ or toxic gases like CO and NO_x. Normally, a gas sensor composed of SnO₂ has a limited sensitivity to chemically stable gases such as methane. Therefore the response characteristics of SnO₂ sensor can be modified in many ways; for example, addition of additive and fabrication of sensor.

The most popular supported additives in SnO₂ gas sensor are noble metals like Pd, Pt, Au and Ag, which are used in order to increase both the sensitivity and selectivity. In addition, a donor impurity like Sb in SnO₂ moves the Fermi level upward which may influence the electrical conductivity of the sample. One of the objectives of this study is to investigate the effects of Sb additive on the sensitivity of SnO₂ gas sensors.

CHAPTER 3

EXPERIMENTAL PROCEDURES

Gas sensor used in this study was SnO₂ type. Antimony (Sb₂O₃) was selected as dopant. It was found to enhance the sensitivity of SnO₂⁴⁰. The highest dopant concentration used was 1.0 wt% Sb₂O₃ doped SnO₂, sintered at 1000°C for 1 hr in air and N₂ atmosphere.

The effects of Sb₂O₃ dopant and sintering atmosphere on the microstructure and electronic structure of SnO₂ were studied. Observations of the microstructure of undoped SnO₂ and Sb-SnO₂ were performed by scanning electron microscopy (SEM) and transmission electron microscopy (TEM). Investigations of the crystalline phases present in Sb-SnO₂ after sintering were carried out using X-ray diffraction technique (XRD). Chemical composition of the surface was studied by X-ray photoelectron spectroscopy (XPS) and ultra-violet photoelectron spectroscopy (UPS). Surface area of sintered SnO₂ added with various binder concentrations was studied by Brunauer, Emmett and Teller (BET) technique. Finally, the electrical property and sensitivity of Sb-SnO₂ to iso-butane were measured.

3.1 Raw materials

Oxides and binders as listed in Table 3.1 were used as starting raw materials for conventional oxide mixing method. The purity for each material was received from the suppliers.

Table 3.1 Chemicals used in preparation of gas sensor elements.

| Materials | Purity (%) | Particle size | Manufacturers |
|---|------------|---------------|---------------|
| Stannic oxide (SnO ₂) | 99.9 | < 44 μm | Aldrich |
| Antimony(III) oxide (Sb ₂ O ₃) | 99 | < 5 μm | Aldrich |
| Poly(viny alcohol) hydrolyzed | 80 | - | Aldrich |
| Diethylene glycol monobutyl ether | 99 | - | Sigma-Aldrich |

3.2 Methodology

The flow chart for oxide mixing technique used in this study is shown in Figure 3.1.

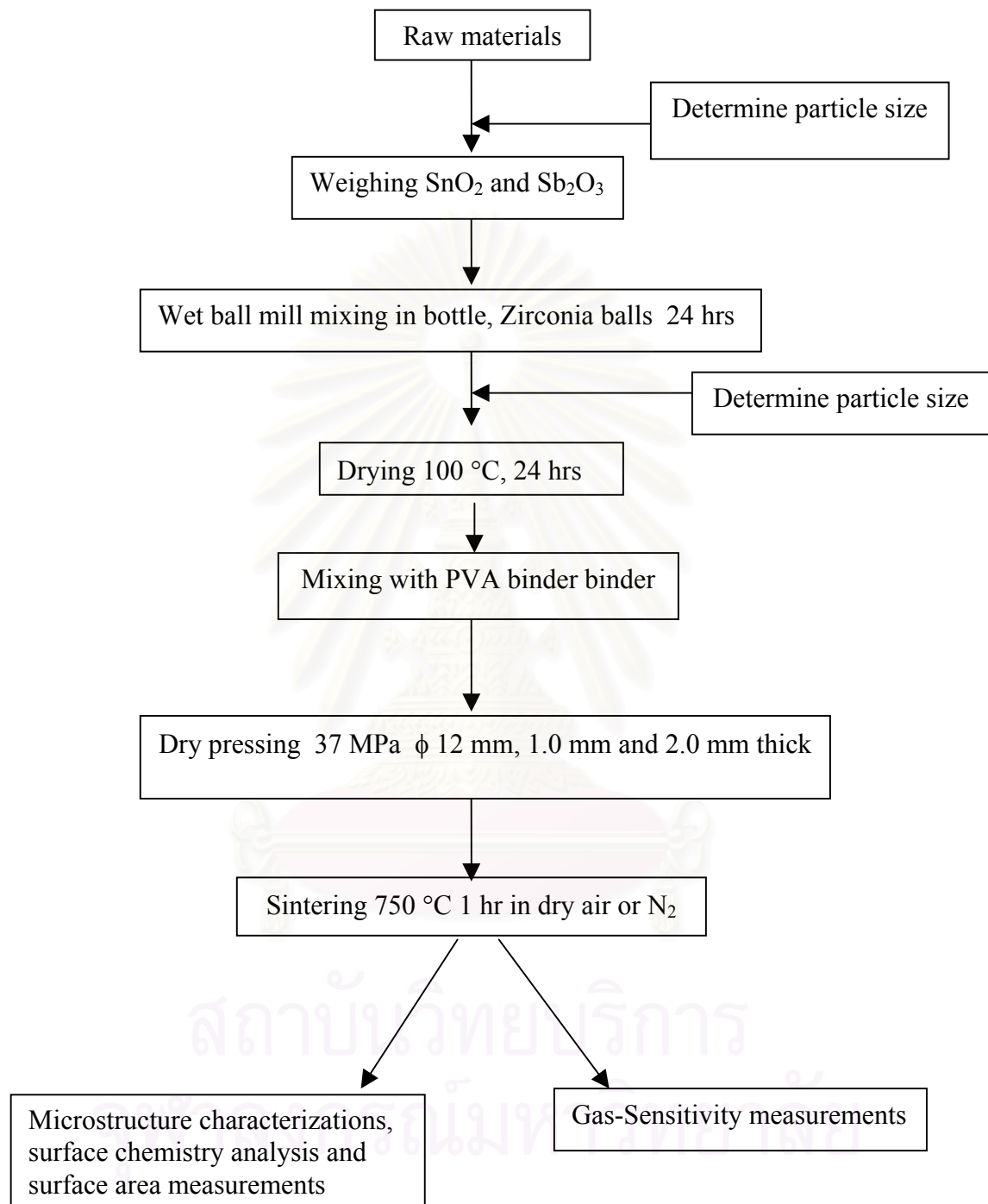


Figure 3.1 Flow diagram of sample preparation of ceramics gas sensor by a conventional oxide mixing process.

3.3 Material characterizations

3.3.1 Particle size and particle size distribution of the starting powder

The study of particle size of the starting powder is useful as a reference data and can be used to compare with the particle size of the powder after wet ball milling.

3.3.1.1 Principles of the technique

Particle size and particle size distribution determination of starting materials were studied using radiation scattering methods by Mastersizer instrument shown in Figure 3.2. The Mastersizer employs two forms of optical configurations to provide its unique specification. The first is the well known optical method, called “conventional Fourier optics”^{Apx.A}. The second is called “reverse Fourier optics”^{Apx.B}. Radiation scattering method utilizes the interaction between a radiation beam and an assembly of particles suspended in a fluid medium. When a beam of radiation strikes an assembly of particles, some of it is scattered (diffracted), some is absorbed, and some is transmitted. In a typical laser diffraction based instrument, a He-Ne laser emits a beam of 632.8 nm, the flux of which is enlarged by a beam expander and radiated upon the particles suspended in the liquid. After being diffracted and dispersed by the particles, the laser beam passes through the condenser lens, and its image is formed at the photocell detector located at the focal point of the lens. The diffraction pattern that appears at the detector is pattern of light and dark concentric rings that corresponds to the particle size distribution. The intensity values are then used to calculate the particle size distribution of the sample. [Mastersizer Reference Manual]

สถาบันวิทยบริการ
จุฬาลงกรณ์มหาวิทยาลัย

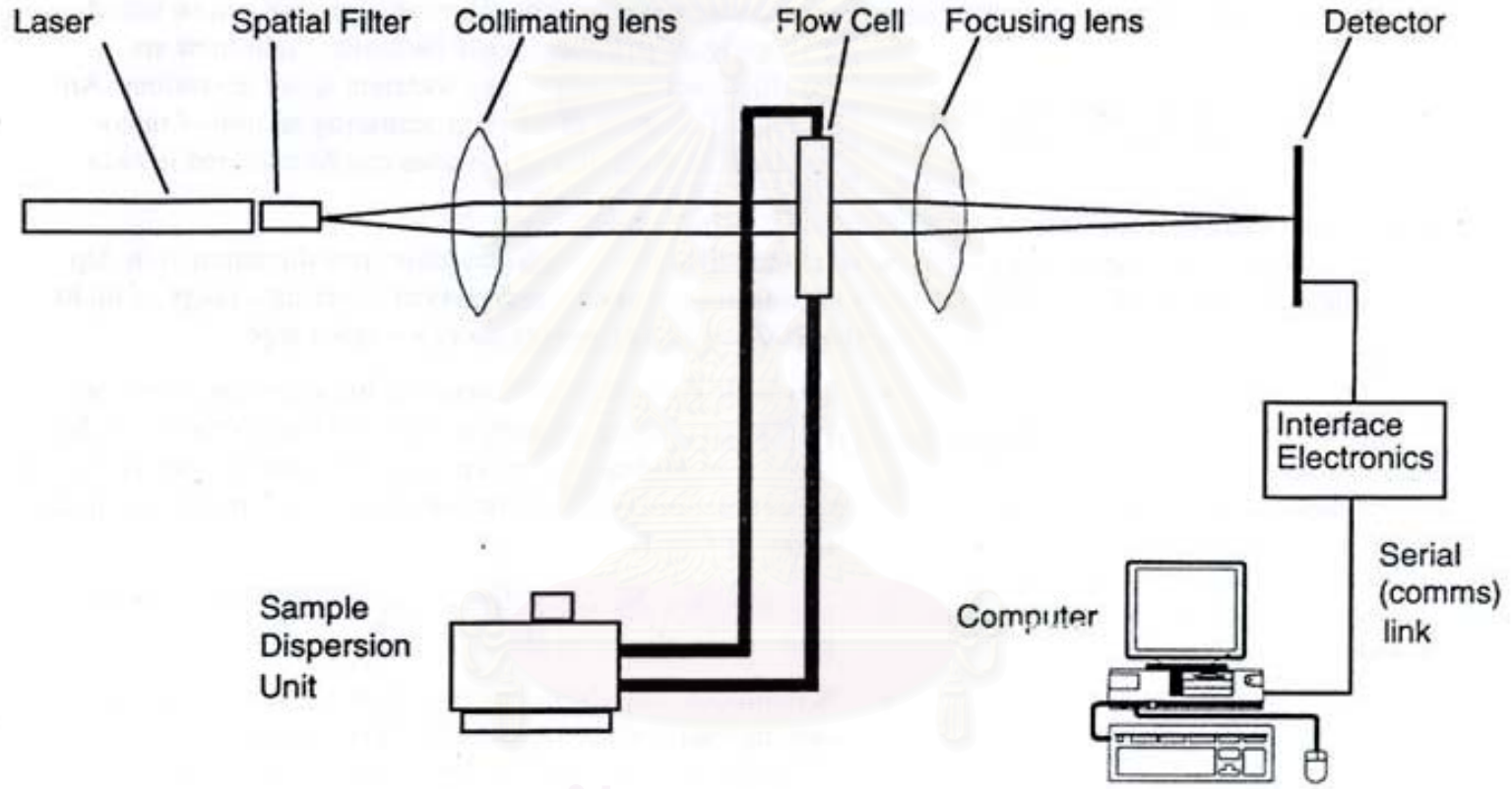


Figure 3.2 Schematic diagram of the Mastersizer system for measuring particle size and particle size distribution

3.3.1.2 Experimental details

In this experimental procedure, particle size and particle size distribution were determined using radiation scattering method. The dispersing medium is distilled water, added with Na-hexametaphosphate, which was treated by stirring and ultrasonic bath.

3.3.2 Phase determination

An X-ray diffractometer (JEOL, model JDX-8030) was used to determine the crystal structure of stannic oxide sensor.

3.3.2.1 Principle of the X-Ray Diffraction (XRD) technique

X-ray crystallography is one of the most useful methods for exploring the nature of matter. X-ray diffractometry (XRD) is used to determine the phase content in many minerals and materials. It is used as an adjunct to chemical analysis in the identification of the constituents of mixtures of crystalline phases, e.g., in minerals, cements and alloys; for measurements of the lattice parameters of artificially produced structures such as the epitaxially grown materials in modern electronic materials.

In the macroscopic version of X-ray diffraction, a certain wavelength of radiation will constructively interfere when partially reflected between surfaces (i.e., the atomic planes) that produce a path difference equal to an integral number of wavelengths. This condition is described by the Bragg law:

$$2 d \sin \theta = n\lambda \quad (\text{Eq. 3.1})$$

where n is an integer, λ is the wavelength of the radiation, d is the spacing between surfaces and θ is the angle between the radiation and the surfaces. This relationship demonstrates that interference effects are observable only when radiation interacts with physical dimensions that are approximately the same size as the wavelength of the radiation. Since the distances between atoms or ions are on the order of 10^{-10} m (1Å).

3.3.2.2 Experimental details of X-ray diffraction analysis

The existing phases in stannic oxide powder and antimony(III) oxide (Sb_2O_3) powder were investigated using X-ray diffraction technique. The powder was mounted in a sample holder and subjected to the room temperature X-ray diffractometer (JEOL, model JDX-8030), using CuK_α radiation ($\lambda = 1.5418\text{\AA}$) and operating at 45.0 kV and 35.0 mA. The XRD data were collected in the range of $2\theta = 5\text{-}90^\circ$, using the step scan of 0.04° and the count time of 1 minute.

Additionally, pellets of stannic oxide doped with 0.3 wt% Sb_2O_3 sintered in air and N_2 atmosphere at 750°C and 1000°C were characterized by X-ray diffraction (XRD) to determine the crystal structure. The pellet samples were examined using the same conditions as stated above.

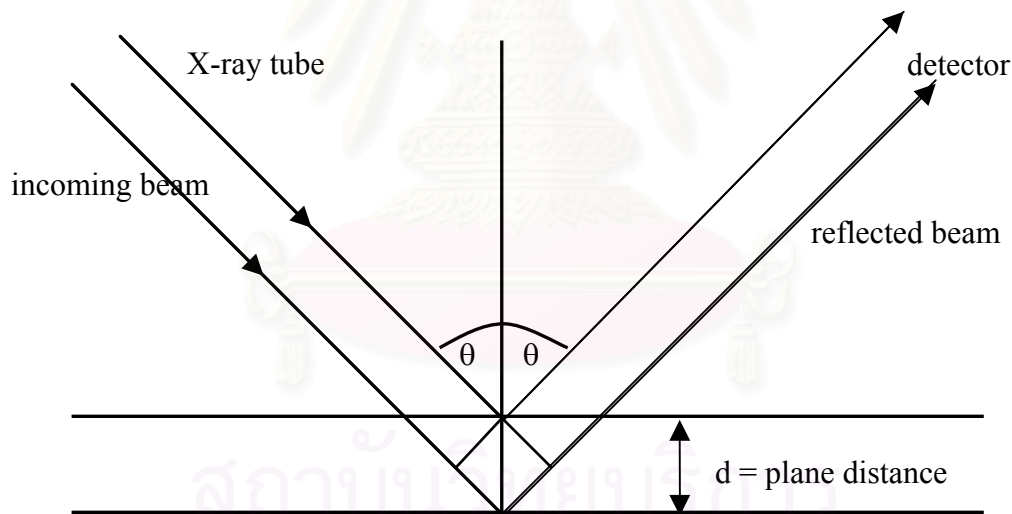


Figure 3.3 XRD measurement.

3.3.3 Porosity determination

Samples of SnO₂ gas sensor were prepared by convention oxide mixing method. Samples were prepared as a highly porous compact and after processing were porous ceramics. Therefore, the porosity is the property of much interest and is correlated with other property, such as electrical resistivity and strength, etc.

3.3.3.1 Principle of the technique

Mercury porosimetry and gas adsorption technique are recognized methods for determination of open pore size distribution (PSD) from which also can be derived surface area and pore size frequency.

Mercury porosimetry and gas adsorption technique are conducted by first preparing a sample of size dependent on the material porosity and with pore volume measurable by the equipment. The sample is placed in a holder called a penetrometer, evacuated, and then immersed in mercury at a low pressure. Increasing pressures are applied on the mercury and corresponding volumes of intruded mercury are determined. The diameter, d , of a cylindrical pore being intruded by mercury of surface tension γ at pressure P at the contact angle θ with the sample, is determined from the Washburn equation :

$$d = \frac{-4\gamma \cos \theta}{P} \quad (\text{Eq. 3.2})$$

where

- d = diameter (cm)
- γ = surface tension (N/cm)
- θ = contact angle
- P = pressure (N/cm²)

The total pore volume can be calculated if all pores have been filled at the maximum pressure. If the true specific gravity of the sample is known, the porosity and apparent density, ρ_a , can be calculated from the total pore volume

$$\rho_a = \frac{1}{V_p} + \frac{1}{\rho_t} \quad (\text{Eq. 3.3})$$

where ρ_a = apparent density
 V_p = the total pore volume per gram
 ρ_t = the true specific gravity

Surface area distribution can also be determined by intergrating the volume-diameter curve, assuming that pores are a series of cylinders of decreasing diameter. Assuming n number of cylindrical pores of length l, these relationships follow :

$$\text{Pore Volume : } V = \frac{n\pi d^2 l}{4} \quad (\text{Eq. 3.4})$$

$$\text{Surface Area : } S = n\pi dl \quad (\text{Eq. 3.5})$$

$$S = \frac{4V}{d} \quad (\text{Eq. 3.6})$$

A convenient single value from the PSD is the mid-pore diameter where half of the pore volume has been intruded by mercury.

3.3.4 Microstructure characterizations

The microstructures of the sintered samples were characterized using scanning electron microscope (JEOL, model JSM-5410) and transmission electron microscope (JEOL 2010). The TEM analysis is used for observing the microstructure of SnO₂ grain at higher resolution more often than SEM analysis.

3.3.4.1 Principle of scanning electron microscopy (SEM)

In a typical SEM configuration which is shown schematically in Figure 3.4, electrons are thermionically emitted from a tungsten or LaB₆ cathode filament towards an anode. The electron beam, which typically has an energy ranging from a few keV to 50 keV, is focused by two successive condenser lenses into a beam with a very fine spot size (~ 5nm). The "Virtual Source" at the top represents the electron gun, producing a stream of monochromatic electrons. The stream is condensed by the first condenser lens. This lens is used to both form the beam and limit the amount of current in the beam. It works in conjunction with the condenser aperture to eliminate the high-angle electrons from the beam. The beam is then constricted by the condenser aperture, eliminating some high-angle electrons. The second condenser

lens forms the electrons into a thin, tight, coherent beam and is usually controlled by the "fine probe current knob". A user selectable objective aperture further eliminates high-angle electrons from the beam. A set of coils then "scan" or "sweep" the beam in a grid fashion (like a television), dwelling on points for a period of time determined by the scan speed (usually in the microsecond range). The final lens, the objective, focuses the scanning beam onto the part of the specimen desired. Schematic diagram showing the basic principles of the scanning electron microscope is shown in Figure 3.5, when the beam strikes the sample interactions occur inside the sample and are detected with various instruments. Before the beam moves to its next dwell point these instruments count the number of interactions and display a pixel on a CRT whose intensity is determined by this number (the more reactions the brighter the pixel). This process is repeated until the grid scan is finished and then repeated, the entire pattern can be scanned 30 times per second.

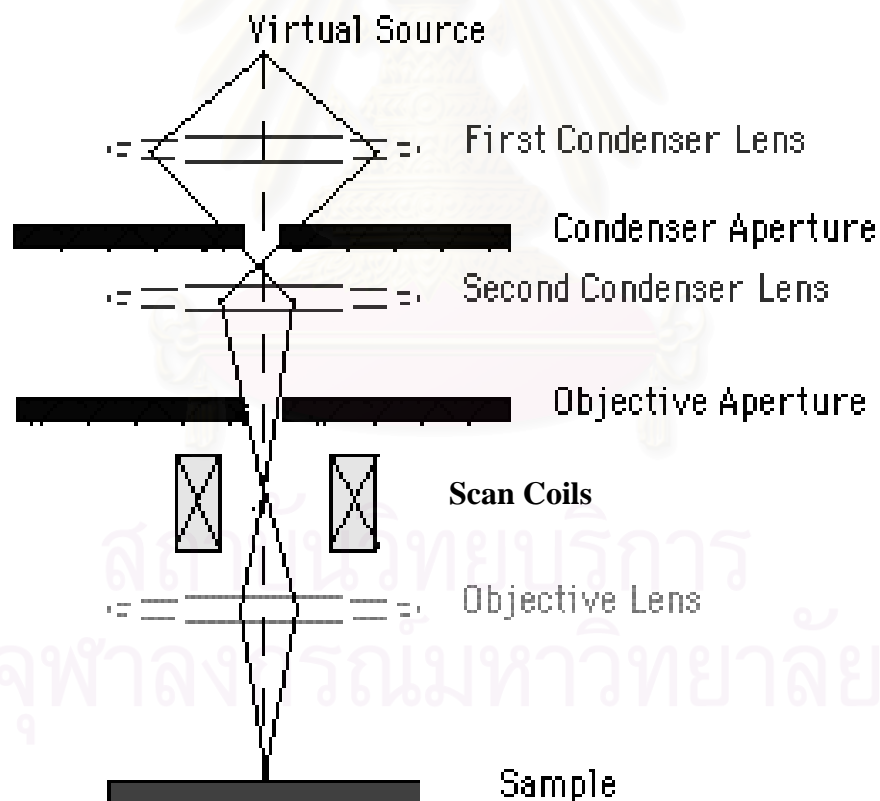


Figure 3.4 Basic principles of the scanning electron microscope (SEM).

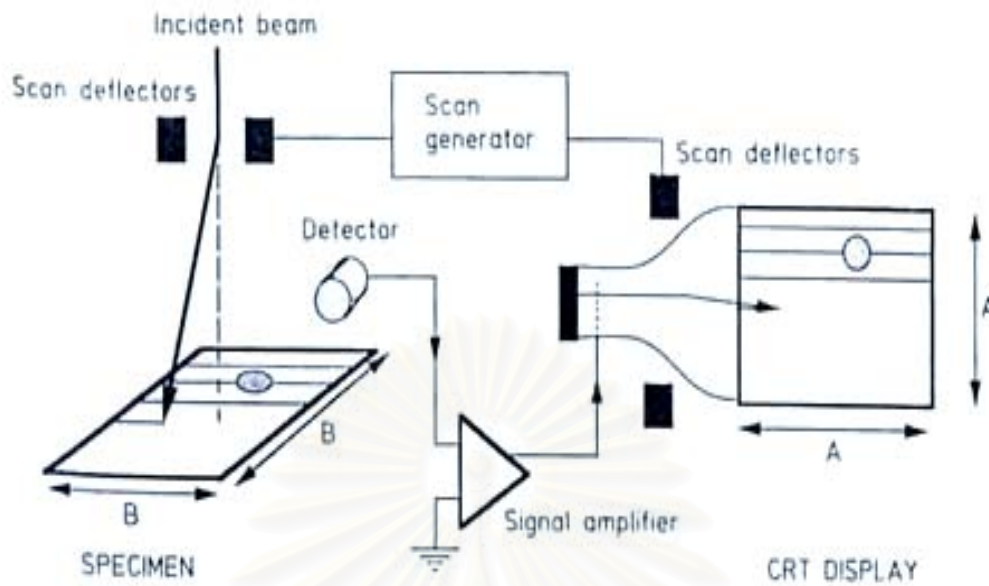


Figure 3.5 Schematic diagram showing the basic principles of the scanning electron microscope (SEM).

3.3.4.2 Experimental details of SEM analysis

Scanning electron microscope (JEOL, model JSM-5410) was used to investigate the microstructure of tin oxide doped with antimony sintered in air and nitrogen atmosphere. SEM digitized micrographs were obtained with a magnification range between 7,500 – 50,000 X.

The antimony-doped tin oxide pellets 13.0 mm in diameter were adhered on a brass-stub using an adhesive tape. The samples on stub were examined by scanning electron microscope operating at acceleration voltage of 25 kV. In addition, the presence and amount of Sb_2O_3 dopant was studied by Energy dispersive X-Ray spectroscopy (EDS) analysis on SEM.

3.3.4.3 Principle of transmission electron microscopy (TEM)

In Figure 3.6, the TEM configuration is shown. The "Virtual Source" at the top represents the electron gun, producing a stream of monochromatic electrons. This stream is focused to a small, coherent beam by the use of condenser lenses 1 and 2. The first lens (usually controlled by the "spot size knob") largely determines the "spot

size"; the general size range of the final spot that strikes the sample. The second lens actually changes the size of the spot on the sample; changing it from a wide dispersed spot to a pinpoint beam. The beam is restricted by the condenser aperture. The beam strikes the specimen and parts of it are transmitted. This transmitted portion is focused by the objective lens into an image. The image is passed down the column through the intermediate and projector lenses, being enlarged all the way. The image strikes the phosphor image screen and light is generated. The darker areas of the image represent those areas of the sample that fewer electrons were transmitted through (they are thicker or denser). The lighter areas of the image represent those areas of the sample that more electrons were transmitted through (they are thinner or less dense).

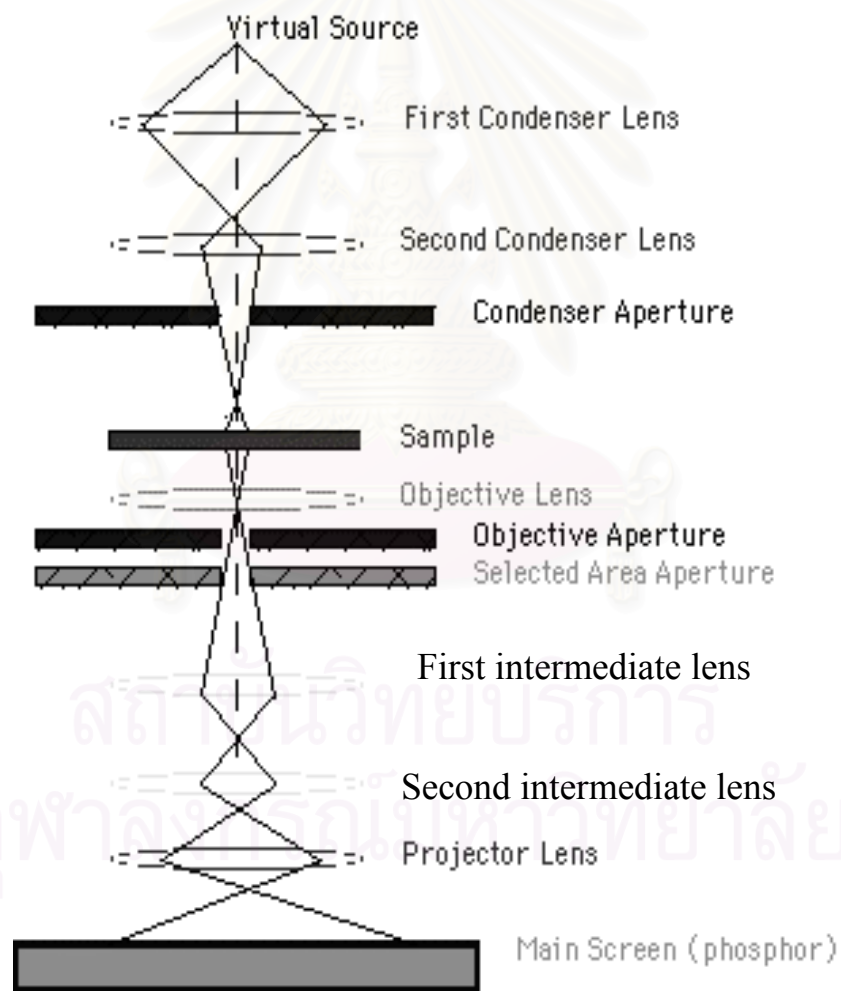


Figure 3.6 Schematic diagram showing the basic principles of the transmission electron microscope (TEM).

3.3.4.4 Experimental details of TEM analysis

The microstructure of the sample was studied using a JEOL 2010 TEM operated at an accelerating voltage of 200kV. In particular, the effect of dopant on the microstructure of SnO₂ sensors was investigated at the grain boundary.

Plane-view TEM specimens were prepared by cutting 4 mm diameter discs with the ultrasonic disc cutter (Gatan 601). Grinder polisher was used to polish the discs. Final thinning for electron transparency was carried out using twin ion beam thinning at an impingement angle of 4° using argon beam with energy of 3-5 kV.

3.3.4 Surface analysis

In this section, the focus is mainly put on the influence of dopant on the electronic structure of SnO₂, because the conduction electrons in SnO₂ played major role in gas sensing. The XPS and UPS were used for study the surface chemistry of undoped and Sb-doped SnO₂.

3.3.5.1 Principle of X-ray photoelectron spectroscopy (XPS)

In an XPS analysis, the sample is irradiated with electromagnetic radiation of energy $h\nu$ and it emits electrons because of the photoelectric effect. These electrons have kinetic energy of the form:

$$E_k = h\nu - E_B \quad (\text{Eq. 3.7})$$

Where E_k is the kinetic energy

$h\nu$ is energy of photon

E_B is the binding energy

The incident radiation has energy greater than 1 KeV and then the electrons come from the inner levels. The most usual source of X-rays is a sample of Mg or Al. Electrons from a cathode produce ionisation of the inner levels of these elements and then X-rays are emitted. Usually the K_α emission is the most important and its energy in Al is 1.487 KeV with a width of 1eV and, in the case of Mg, it has energy of 1.254 KeV with a width of 0.8 eV. An XPS spectrum is obtained as a plot of the number of

detected electrons per energy interval versus their kinetic energy and the minimum width of the lines comes from the uncertainty in the radiation energy.

The electron binding energies are dependent on the chemical environment of the atom, making XPS useful to identify the oxidation state and ligands of an atom.

XPS instruments consist of an X-ray source, an energy analyzer for the photoelectrons, and an electron detector. The analysis and detection of photoelectrons requires that the sample be placed in a high-vacuum chamber. Since the photoelectron energy depends on X-ray energy, the excitation source must be monochromatic. The energy of the photoelectrons is analyzed by an electrostatic analyzer, and the photoelectrons are detected by an electron multiplier tube or a multichannel detector such as a microchannel plate.

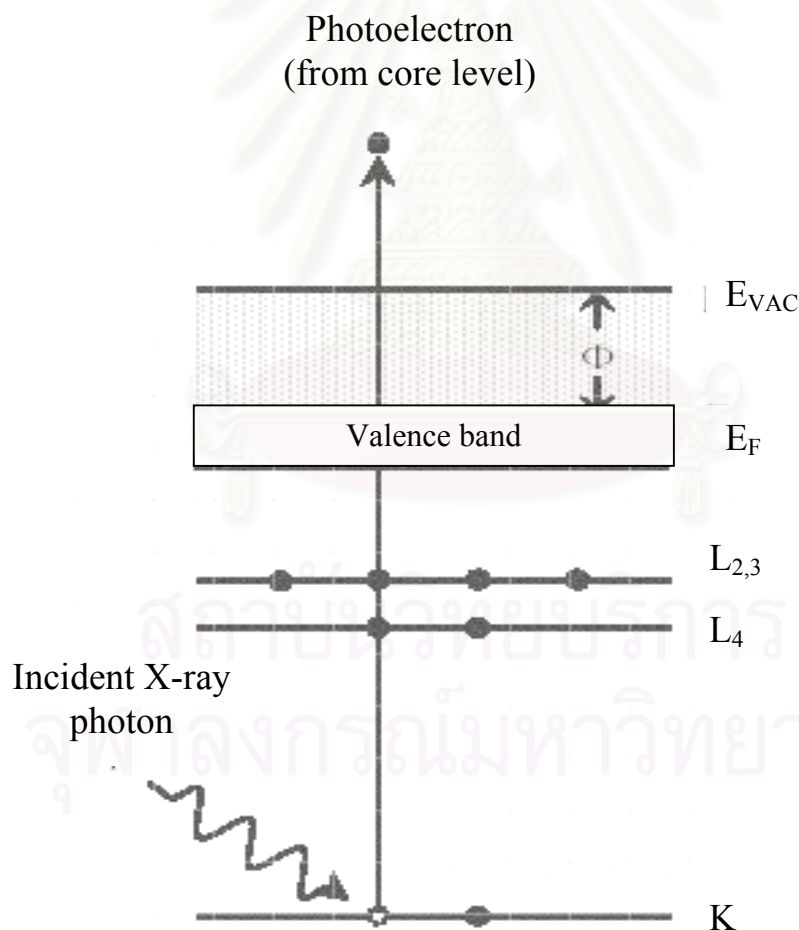


Figure 3.7 Energy-level diagram showing the electron transitions that form the basic for X-ray photoelectron spectroscopy (XPS).

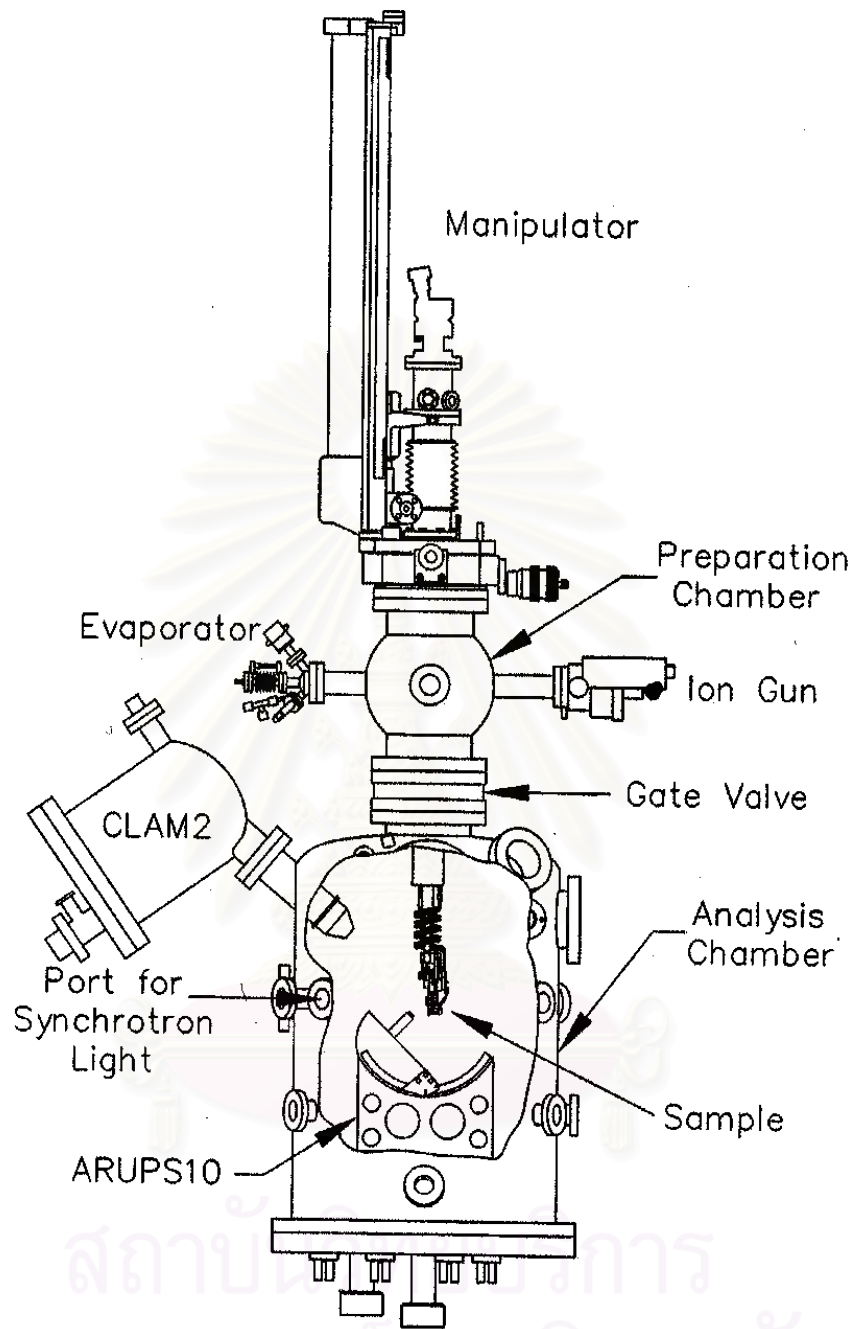


Figure 3.8 X-ray Photoelectron Spectrometer at Siam Photon Laboratory. The station consist of sample preparation section and analysis section.

3.3.5.2 Experimental details of XPS analysis

For XPS analysis at the Siam Photon Laboratory, MgK_{α} source, which produced photons with an energy of 1253.6 eV and working distance 60 mm was used. Surfaces of samples were cleaned by Ar^{+} sputtering, using ion energy of 120 eV for 40 min. XPS data were collected and analyzed in CLAM 2 and ARUPS 10 spectrometer (Figure 3.8), working at a vacuum pressure of 1.3×10^{-6} Torr.

3.3.5.3 Principle of Ultraviolet photoelectron spectroscopy (UPS)

Ultraviolet light is shone at the sample using a Helium lamp emitting at 21.2 eV (He I radiation) or 40.8 eV (He II radiation). The low photon energy in UPS means that deep core electron levels cannot be excited, and only photoelectrons emitted from the valence band or shallow core levels are accessible. Angle resolved UPS can be used to determine the band structure of the material under investigation. UPS can also be used to identify molecular species on surfaces by identifying characteristic electron energies associated with the bonds of the molecules. Comparing with XPS, the resolution of the UPS is rather high ($\sim meV$), so this is adequate for studying band structures though it is more surface sensitive than XPS.

3.3.5.4 Experimentaled details of UPS analysis

For UPS analysis at the Siam Photon Laboratory, He(I) source was used, which produced photons with an energy of 21.21 eV. Surface of samples were cleaned by Ar^{+} sputtering, using ion energy of 120 eV for 40 min. UPS data were collected and analyzed in CLAM 2 and ARUPS 10 spectrometer, working at a vacuum pressure of 1.3×10^{-6} Torr.

Table 3.2 Comparison of XPS and UPS techniques.

| | XPS | UPS |
|------------------------------|-------------------------------------|-------------------------------------|
| Source | Mg K_{α} | He (I) |
| Photons energy | 1253.6 eV | 21.2 eV |
| Photo electrons emitted from | Core level | Valence band |
| Useful for identification of | Oxidation state and ligands of atom | Characteristic of electron energies |

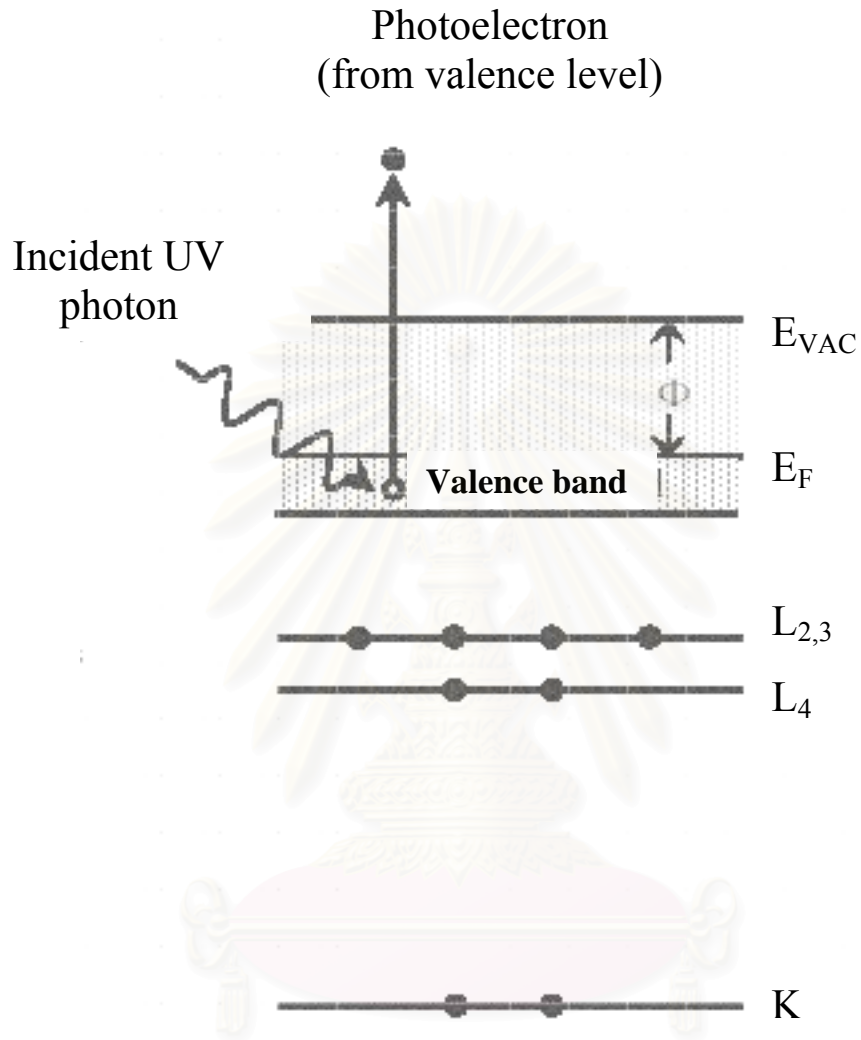


Figure 3.9 Energy-level diagram showing the electron transitions that form the basic for Ultraviolet photoelectron spectroscope (UPS).

3.4 Conductivity Measurement

The SnO₂ sensing element was tested for gas response by measuring the resistivity change when exposed to dry air and iso-butane. The SnO₂ sensing elements with platinum electrodes were placed in a tube furnace and gas flow meter was used to control the flow rate of sample gases.

The gas-sensing properties were examined in a heated chamber through which dry air or 0.51%iso-butane was allowed to flow at a rate of 300 ml/min. The operating temperature was varied from 300-400°C to determine the optimum sensitivity (*S*). The gas sensitivity (*S*) is defined as:

$$S = \frac{(R_a - R_s)}{R_a} \quad (\text{Eq. 3.8})$$

Where *R_a* is the electric resistance in air and *R_s* is the electric resistance in sample gas.

The gas test system is shown in Figure 3.8 and the measurement cell of SnO₂ sensor contacted with electrode is shown in Figure 3.9. First, SnO₂ sensor was put on to the sample support connected with the platinum electrode as shown in Figure 3.9, after that the sample was placed into the gas chamber system as shown in Figure 3.8. The operating temperature was set between 300-400°C and dry air was let into the chamber at flow rate of 300 ml min⁻¹. Before measuring the gas response, the sensor was stabilized at the operating temperature for at least 2 hr. After that, expose to the 0.51% iso-butane for 15 min, follow by 30 min recovery in dry air. Finally, the resistance change of SnO₂ sensor was measured when exposed to air or iso-butane and the sensitivity of SnO₂ sensor was determined by Eq.3.8.

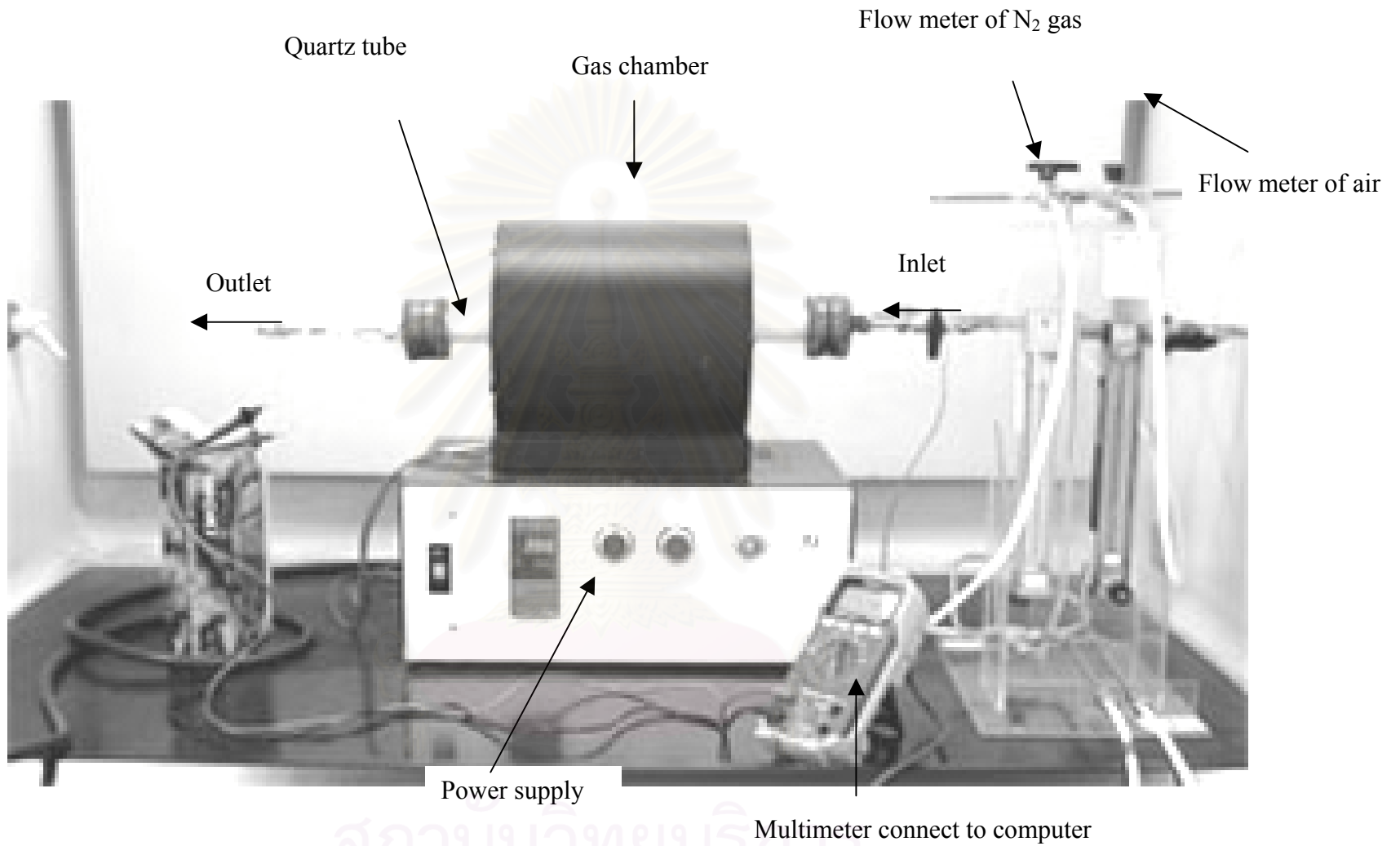


Figure 3.10 Gas sensor test system

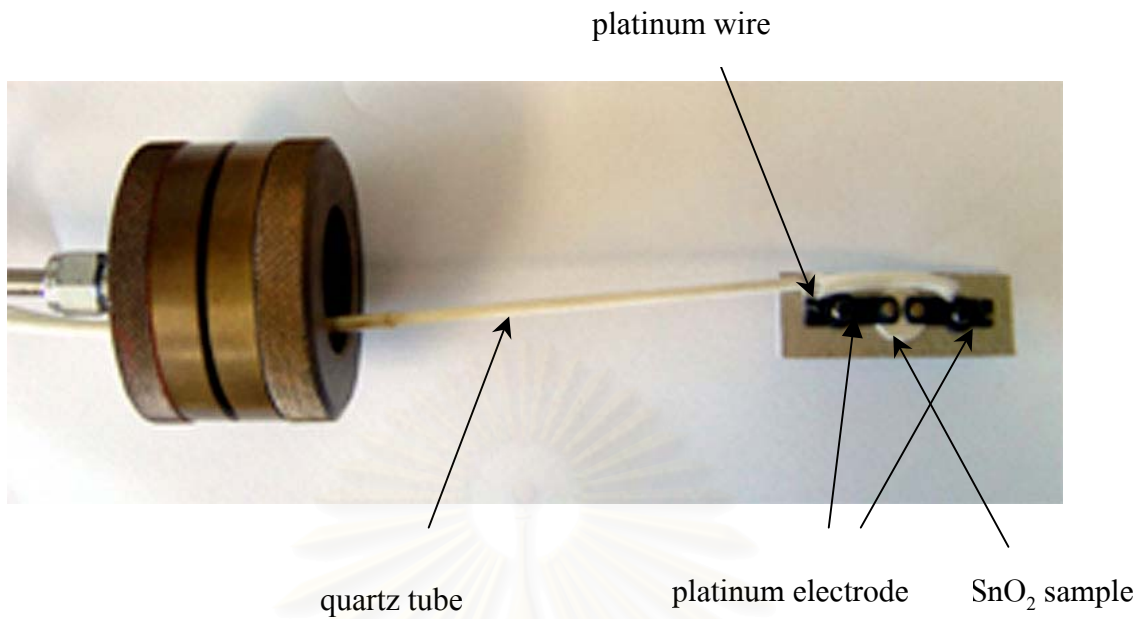


Figure 3.11 Configuration of test sample in the gas chamber system.

สถาบันวิทยบริการ
จุฬาลงกรณ์มหาวิทยาลัย

CHAPTER 4

RESULTS AND DISCUSSIONS

In this chapter, the influences of dopant concentration on the microstructure, electronic structure and sensitivity to iso-butane of sintered SnO₂ gas sensors are investigated. Sb-doped SnO₂ gas sensors were prepared by a conventional mixed oxide method. SnO₂ was doped with various concentrations of Sb₂O₃ (0.3-1.0wt%) and sintered in air or in N₂ atmosphere. Structural and morphological changes of the samples were characterized by X-ray diffraction study (XRD), scanning electron microscopy (SEM) and transmission electron microscopy (TEM). XRD study reveals that sintered Sb-SnO₂ contains a cassiterite phase. SEM and TEM investigations of the samples sintered in air and N₂ atmosphere show porous polycrystalline structure with grain size ranging from 50-300 nm. X-ray photoelectron spectroscope (XPS) analysis was carried out in order to investigate the oxidation states of Sn and Sb in the system and the Fermi level of Sb-doped SnO₂. Ultraviolet photoelectron spectroscope (UPS) study was used to investigate the valence state of Sb-SnO₂. From the XPS analysis, the splitting of Sn 3d peak could not be observed and thus suggesting that the oxidation state of Sb-doped SnO₂ be 4⁺ and/or 2⁺. Gas sensitivity was measured at temperature range of 300-400°C as iso-butane vapor was introduced into flowing dry air and correlated with the response time of gas-sensor. It was found that the gas sensitivity increased with the operating temperature and SnO₂ doped with 0.8wt% Sb₂O₃ exhibited the highest sensitivity to iso-butane.

4.1 Particle size and particle size distribution

This section presents the data on particle size and particle size distribution of tin oxide (SnO₂) powder raw material as shown in appendix A and Figure 4.1 and antimony oxide (Sb₂O₃) powder raw material as shown in appendix .B and Figure 4.2.

Sample preparations were performed by the conventional mixed oxide method. The raw materials were wet mixed in a polyethylene bottle for 24 hr, using zirconia balls (ZrO₂) as grinding media and isopropanol as solvent. The purpose of this process was to reduce the particle size of the starting materials and to mix together. After mixing, to remove the solvent, the mixture was filtered and dried at

100°C for 24 hr. Then the particle size and particle size distribution of the mixture were determined again. The analysis results of the mixture are shown in Table 4.3^{Apx.C} and Figure 4.3.

In all the presented data, the first two columns show the particle size of SnO₂ powder between the smallest and the largest size distribution. The middle column shows the percentage of mass of SnO₂ powder which is between the smallest and the largest size of distribution. The fourth column shows the cumulative size distribution which is obtained by summing the fractions of particle that are larger than specific size (between the smallest and largest sizes of distribution). And the last column shows the cumulative size distribution which is obtained by summing the fractions of particle that are finer than specific size.

From the particle size distribution data shown in appendix A, a corresponding curve can be constructed as shown in Figure 4.1. Data presented in Figure 4.1 were used to analyse and compare the mean size and the distribution of sizes. The results show that the mean particle size diameter of SnO₂ is 0.78 µm and the particle size distribution is normal or gaussian distribution.

The data analysis of Sb₂O₃ powder is shown in appendix B. The details shown in appendix B are the same as stated above in appendix A.

From the particle size distribution data of Sb₂O₃ shown in appendix B, the corresponding curve can be constructed and shown here in Figure 4.2. The mean particle size of Sb₂O₃ is 5.69 µm and the particle size distribution is normal or gaussian distribution.

Appendix C and Figure 4.3 show the particle size distribution of SnO₂ powder doped with 0.3 wt% Sb₂O₃ after wet ball milling. The result shows that the mean particle size is 0.17 µm and the particle size distribution is normal or gaussian distribution.

From the analysis result shown in Figure 4.1-4.3, the mean particle size of mixed powder that was milled for 24 hr is 0.17 μm , which is smaller than the mean particle size of tin oxide raw material about 22%. The particle size distributions of both starting raw materials and mixed powder are normal or gaussian distributions.



สถาบันวิทยบริการ
จุฬาลงกรณ์มหาวิทยาลัย

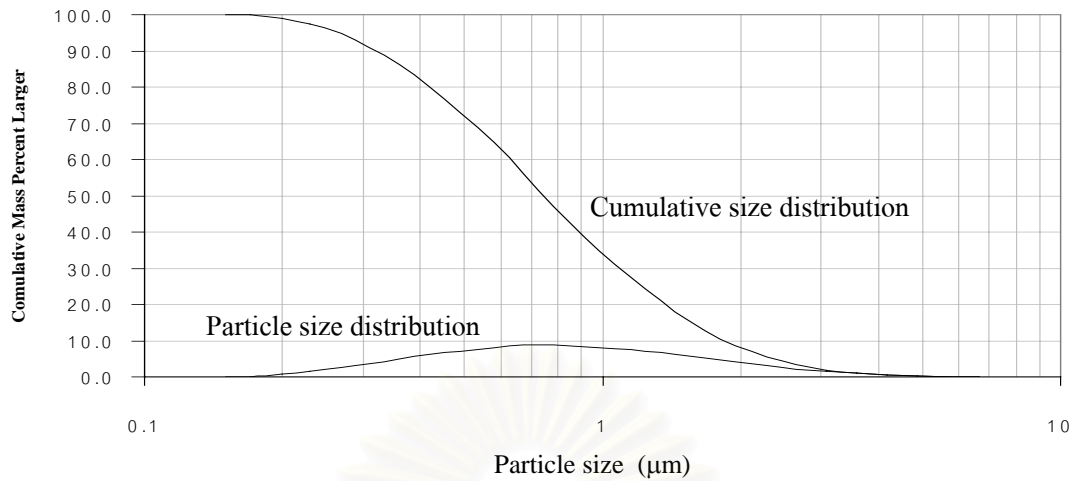


Figure 4.1 Cumulative and sizes distribution of SnO_2 powder. The distribution in ln-normal curve.

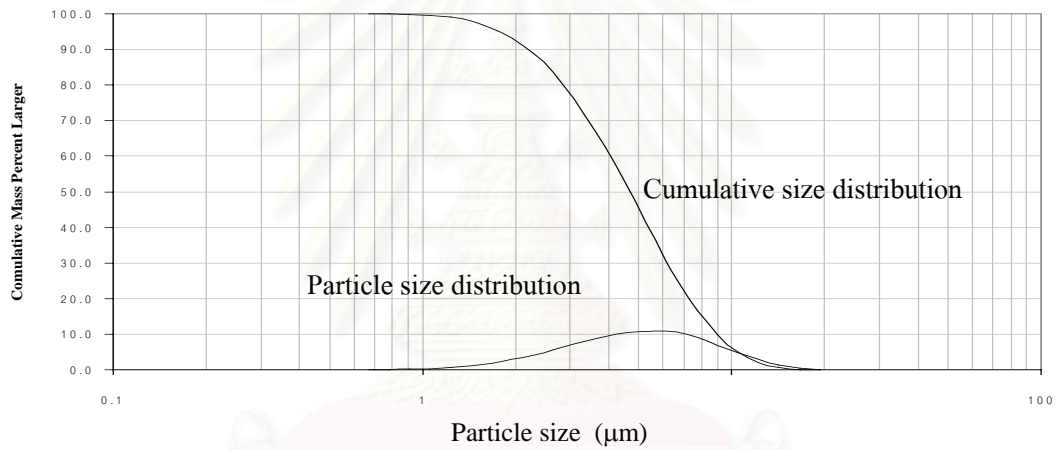


Figure 4.2 Cumulative and sizes distribution of SnO_2 powder. The distribution in ln-normal curve.

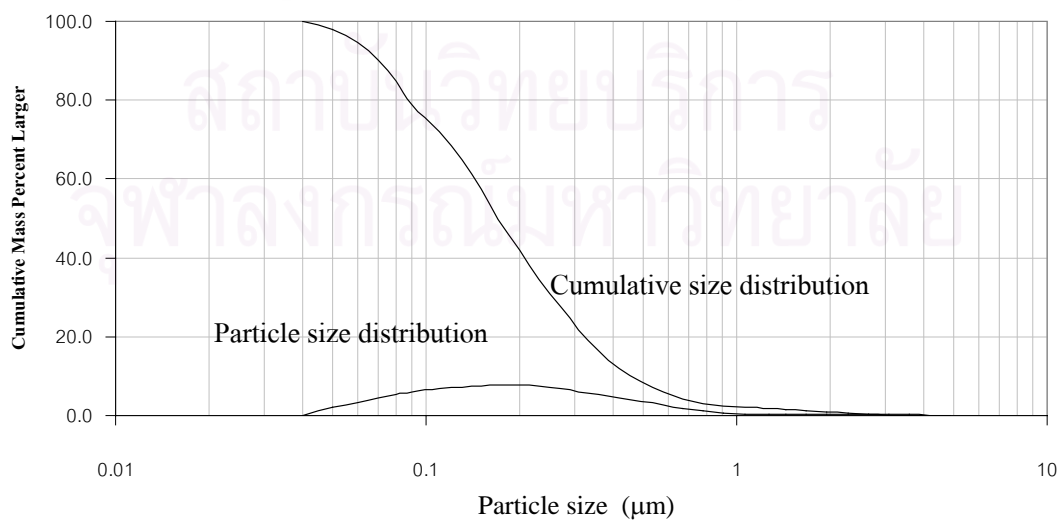


Figure 4.3 Cumulative and sizes distribution of SnO_2 powder with 0.3 wt % Sb_2O_3 dopant. The distribution in ln-normal curve.

4.2 Physical properties of tin oxide sensor

In this section, the crystal phase and the microstructure of SnO₂ raw material and SnO₂ doped with Sb₂O₃ sintered in air and N₂ atmosphere at 1000°C will be studied. The comparison of the crystal phase of SnO₂ pellet before and after sintering will be determined by X-Ray diffraction (XRD) technique. The microstructure will be characterized by scanning electron microscopy.

4.2.1 XRD analysis of crystal phase

The phases present in commercial raw materials and in SnO₂ doped with Sb₂O₃, sintered in air and N₂ atmosphere at 1000 °C, were identified by XRD analysis. By comparing to the JCPDS file (Appendix C), the XRD results show a single phase as illustrated in Figure 4.4.

From phase analysis shown in Figure 4.4 and Table 4.1, the XRD patterns of SnO₂ and Sb₂O₃ raw materials correspond to the cassiterite phase (JCPDS No.22150) and senarmonite phase (JCPDS No.50534), respectively. XRD patterns of SnO₂ doped with 0.3 wt% Sb₂O₃ before and after sintering in air and N₂ atmospheres at 1000°C exhibited a cassiterite phase, which is the same as the starting stannic oxide raw material (corresponding to JCPDS No.22150).

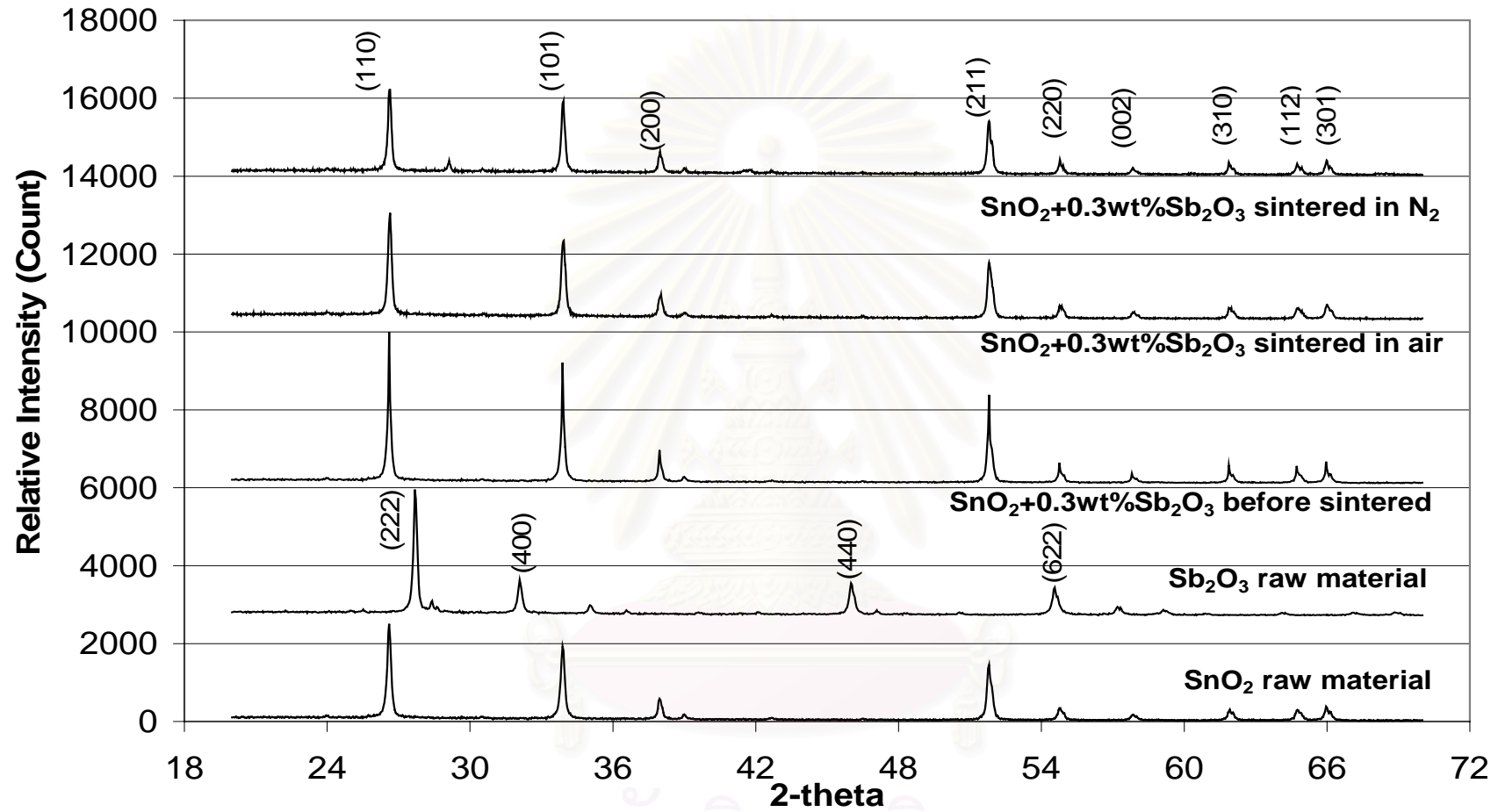


Figure 4.4 XRD patterns of as received raw materials and stannic oxide powder doped with 0.3 wt% Sb₂O₃ before and after sintering in air and in N₂.

Table 4.4 XRD data of raw materials, mixed powder before sintering and after sintering in air and N₂ from JCPDS file.

| SnO ₂ standard | | | SnO ₂ raw material | | | SnO ₂ doped with 0.3wt% Sb ₂ O ₃ before sintered | | | SnO ₂ doped with 0.3wt% Sb ₂ O ₃ sintered in air at 1000°C | | | SnO ₂ doped with 0.3wt% Sb ₂ O ₃ sintered in N ₂ at 1000°C | | |
|---------------------------|---------|-------|-------------------------------|---------|-------|--|---------|-------|--|---------|-------|---|---------|-------|
| I/I ₀ | 2-theta | (abc) | I/I ₀ | 2-theta | (abc) | I/I ₀ | 2-theta | (abc) | I/I ₀ | 2-theta | (abc) | I/I ₀ | 2-theta | (abc) |
| 100 | 26.54 | (110) | 100 | 26.60 | (110) | 100 | 26.6 | (110) | 100 | 26.64 | (110) | 100 | 26.62 | (110) |
| 81 | 33.86 | (101) | 77 | 33.88 | (101) | 80 | 33.88 | (101) | 78 | 33.92 | (101) | 86 | 33.9 | (101) |
| 63 | 51.69 | (211) | 57 | 51.80 | (211) | 59 | 51.80 | (211) | 55 | 51.8 | (211) | 63 | 51.80 | (211) |
| 24 | 37.93 | (200) | 24 | 37.96 | (200) | 22 | 37.96 | (200) | 24 | 38.00 | (200) | 26 | 37.97 | (200) |
| 17 | 64.73 | (301) | 15 | 65.96 | (301) | 15 | 65.96 | (301) | 14 | 66.00 | (301) | 17 | 65.98 | (301) |
| 17 | 54.76 | (220) | 14 | 54.80 | (220) | 14 | 54.76 | (220) | 14 | 54.78 | (220) | 17 | 54.78 | (220) |
| 15 | 65.89 | (112) | 12 | 64.76 | (112) | 12 | 64.72 | (112) | 12 | 64.76 | (112) | 16 | 64.75 | (112) |
| 13 | 61.83 | (310) | 12 | 61.92 | (310) | 12 | 61.88 | (310) | 12 | 61.9 | (310) | 15 | 61.88 | (310) |

From Figure 4.4 , which shows the XRD patterns of SnO₂ doped with 0.3wt% Sb₂O₃ before and after sintering in air or N₂ at 1000°C, and those of the raw materials, characteristic peaks of SnO₂ doped with 0.3wt% Sb₂O₃ corresponding to the cassiterite phase of SnO₂ standard are observed. However, no significant peaks corresponding to Sb₂O₃ are observed, suggesting that the concentration of Sb₂O₃ in SnO₂ be smaller than expected from its loading in the oxide mixing method.

Another possibility is that, a considerable amount of Sb₂O₃ may dissolve into the structure of SnO₂. Energy Dispersive Spectroscopy (EDS) is a standard procedure for identifying and quantifying elemental composition of a sample. The characteristic X-rays are produced when a material is bombarded with electrons in an electron beam instrument, such as a scanning electron microscope (SEM). Detection of these X-rays can be accomplished by an energy dispersive spectrometer. EDS involves measuring these X-rays as a function of energy with a solid-state detector and specific peaks in the spectra reflect the presence of specific elements in the sample surface.

EDS analysis of SnO₂ doped with 0.5wt% Sb₂O₃ shows that the doping concentration of Sb₂O₃ in SnO₂ is 0.15wt%, as shown in Table 4.2 and Figure 4.5.

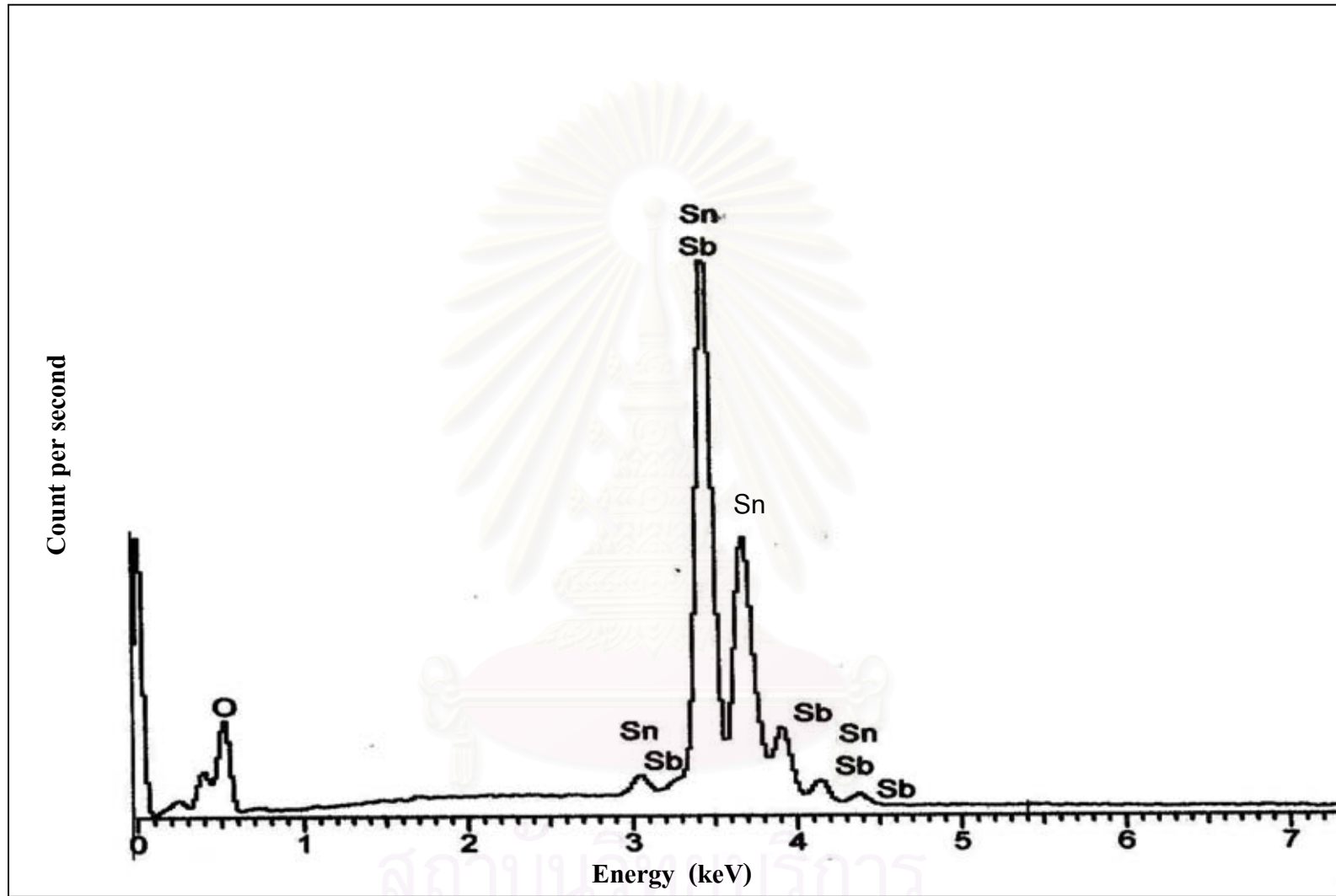


Figure 4.5 EDS spectrum of SnO_2 doped with 0.5wt% Sb_2O_3 sintered in air.

From the EDS spectrum of SnO₂ doped with 0.5wt% Sb₂O₃ shown in Figure 4.5, the X-ray spectrum features visible are Sn at energy of 3.05, 3.45, 3.67, 4.15 keV, Sb at energy of 3.07, 3.46, 3.90, 4.15, 4.4 keV and O at energy of 0.5 keV.

Quantitative analysis was made from the heights of peaks compared to calibration standard elemental spectra as shown in Table 4.2.

Table 4.2 The composition of SnO₂ doped with 0.5wt% Sb₂O₃ from EDS analysis.

| Element | Apparent concentration | Intensity correction | Weight % |
|---------|------------------------|----------------------|----------|
| O K | 24.52 | 0.3897 | 27.99 |
| Sn L | 149.90 | 0.9279 | 71.87 |
| Sb L | 0.31 | 0.9304 | 0.15 |
| Total | - | - | 100 |

From Table 4.2, the composition of SnO₂ sample consists of 71.87wt%Sn, 27.99wt%O and 0.15wt%Sb. From the EDS analysis of SnO₂ doped with 0.5wt% Sb₂O₃, it is found that the doping concentration of Sb₂O₃ dissolved into the structure of SnO₂ is 0.15 wt%.

4.2.2 Microstructure

The microstructure of SnO₂ and Sb₂O₃ raw materials and Sb₂O₃-doped SnO₂ (0.3-1.0 wt%) before and after sintering in air and N₂ were studied by SEM and TEM and are shown here in Figure 4.6 - 4.7.

สถาบันวิทยบริการ
จุฬาลงกรณ์มหาวิทยาลัย



Figure 4.6 SEM micrograph of SnO₂ raw material. The average particle size of SnO₂ raw material is in the range of 50-200 nm and the shape of SnO₂ powder is spherical.

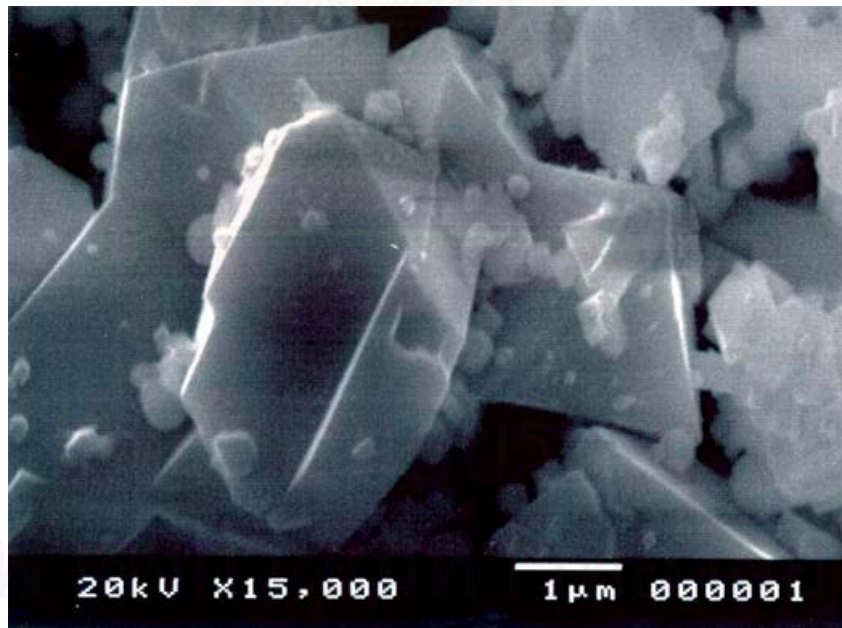


Figure 4.7 SEM micrograph of Sb₂O₃ raw material. The large particle size of Sb₂O₃ raw material is in the range of 1 – 4 μm and the fine particle is in the range of 0.2 - 0.4 μm. The shape of Sb₂O₃ powder is irregular.

The microstructures of SnO₂ and Sb₂O₃ raw materials are shown in Figure 4.6 - 4.7. SEM observations of SnO₂ raw materials show that the commercial powder consisted of particles that are inhomogeneous in size. The particles are fine but the size distribution is large. The average particle size of SnO₂ raw material is in the range of 50-200 nm. The shape of SnO₂ powder is spherical.

SEM observations of Sb₂O₃ raw materials show that the commercial powder is made of particles that are inhomogeneous in size and the size distribution is very large. The large particle size of Sb₂O₃ raw material is in the range of 1 – 4 μm and the fine particle is in the range of 0.2 - 0.4 μm. The shape of Sb₂O₃ powder is irregular.

4.3 Effect of sintering atmosphere on the microstructure of tin oxide gas sensor

The purpose of this section is to study the microstructure of SnO₂ doped with Sb₂O₃ pellet before and after sintering in air and N₂ atmospheres. Moreover, the effect of sintering atmosphere on the microstructure of SnO₂ sample is also studied.

Figure 4.8 (a)-(d) show the SEM micrographs of SnO₂ doped with 1.0wt%Sb₂O₃ pellet before and after sintering in air and N₂ atmospheres. Figure 4.8 (a) and (b) show the SEM micrographs of SnO₂ doped with 1.0wt%Sb₂O₃ pellet before sintering, almost of particles are small (~ 30 nm) but the size distribution size is large with some large grains (250nm). The average particle size of SnO₂ doped with 1.0wt%Sb₂O₃ before sintering is in the range of 30-200 nm.

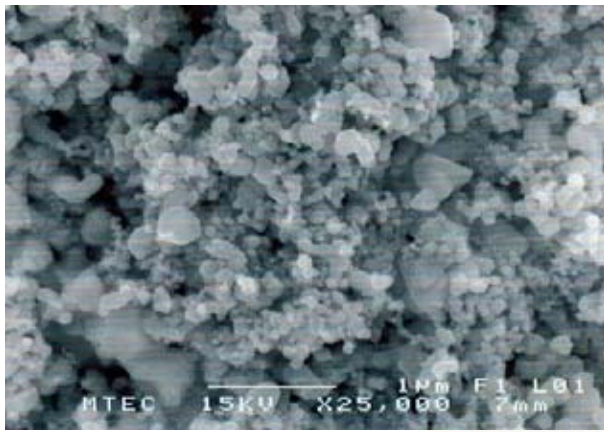
After sintering, it was found that the amount of small grains decreases and the grain growth occurs. The average grain sizes of SnO₂ doped with 1.0wt%Sb₂O₃ sintered in air and N₂ atmosphere are in the range of 50-350 nm and 50-300 nm, respectively, as shown in Figure 4.8 (c)-(d). The samples exhibit a porous polycrystalline structure with a wide distribution of grain size. The variation of grain size and other parameters such as porosity and surface area are shown in Table 4.2. The porosity and the surface area were measured by Brunauer, Emmett and Teller (BET) technique.

Table 4.3 Influence of the sintering condition on the surface area and grain size of SnO₂ samples.

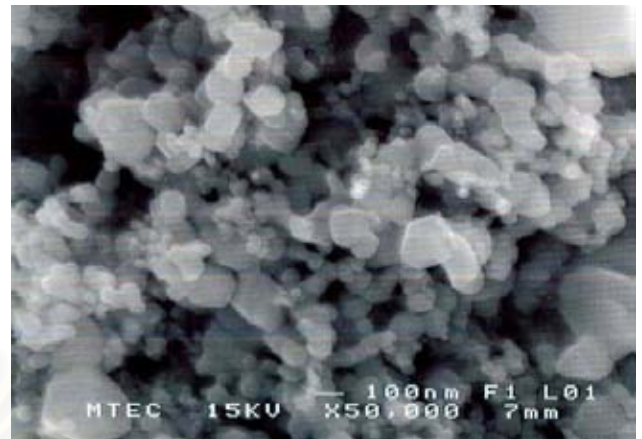
| Sintering condition | Surface area (m ² g ⁻¹) | Grain size (nm) |
|---------------------------------|--|-----------------|
| Before sintering | 6.5 | 30-200 |
| 1000°C – 1 hr in air | 3.76 | 50-350 |
| 1000°C – 1 hr in N ₂ | 3.29 | 50-300 |

From Table 4.3, it is found that the surface area of SnO₂ doped with 1.0wt% Sb₂O₃ pellet before sintering is 6.5 m²g⁻¹ and grain sizes is between 30-200 nm. However, the surface areas of SnO₂ doped with 1.0wt%Sb₂O₃ sintered in air and N₂ atmospheres are 3.76 m²g⁻¹ and 3.29 m²g⁻¹, respectively. The grain sizes of SnO₂ doped with 1.0wt%Sb₂O₃ sintered in air and N₂ are larger than the grain size of SnO₂ before sintering. From this result, the sintered SnO₂ sample has less surface area than that of the SnO₂ sample before sintering because of the grain growth.

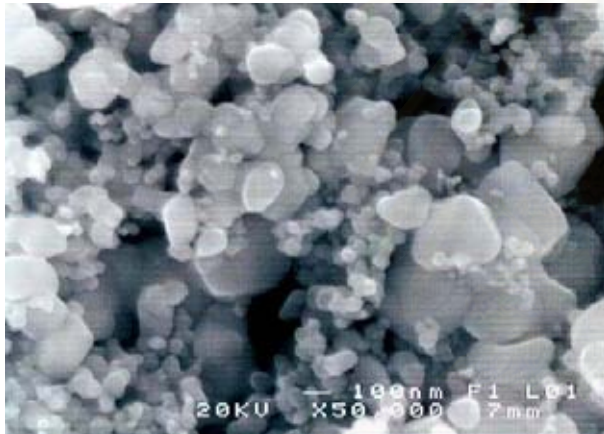
From the study about the effect of sintering atmosphere on the microstructure of the sample, it is found that sample sintered in air has higher surface area than sample sintered in N₂ atmosphere. Therefore, it was suggested that the sintering condition have an effect on the surface area of SnO₂ sample. Surface area of the SnO₂ sample sintered in air is higher than the sample sintered in N₂ because the PVA binder contained in the sample sintered in air is burnt out better than the SnO₂ sample sintered in N₂ atmosphere.



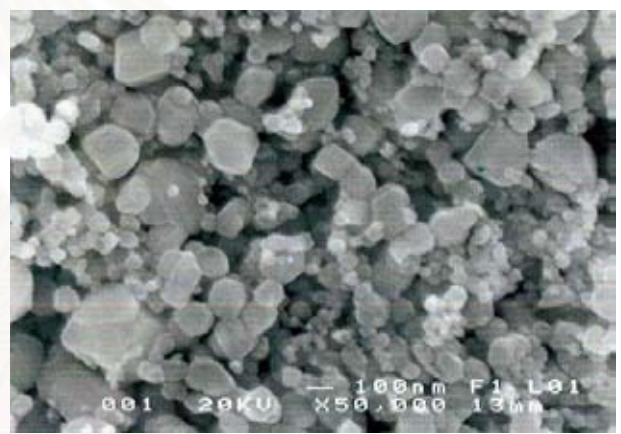
(a)



(b)



(c)



(d)

Figure 4.8 SEM micrographs of SnO₂ doped with 1.0 wt% Sb₂O₃ pellets, (a) –(b) before sintering. The average particle size is in the range of 30-200 nm, (c) after sintering in air at 1000°C. The average grain sizes are in the range of 50-350 nm and (d) after sintering in N₂ at 1000°C, the average grain size is in the range of 50-300 nm.

Furthermore, the microstructures of the SnO₂ sensors were studied by transmission electron microscopy (TEM) technique at high resolution. The shape of grain and small grain size in the order of nanometer can be observed. Moreover, the elemental composition of SnO₂ doped with Sb₂O₃ at grain and grain boundary can be detected by Energy Dispersive X-ray spectroscopy analysis on TEM.

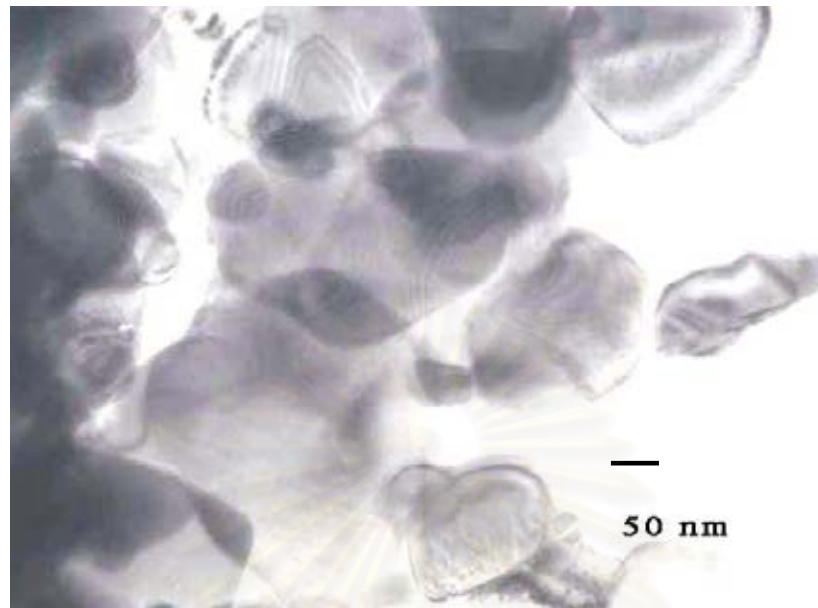
Energy dispersive X-ray spectroscopy (EDS) is a chemical microanalysis technique. The technique utilizes X-rays that are emitted from the sample during bombardment by the electron beam to characterize the elemental composition of the analyzed volume. The EDS X-ray detector measures the number of emitted X-rays versus their energy. The energy of the X-ray is characteristic of the element from which the X-ray was emitted. A spectrum of the energy versus relative counts of the detected X-rays is obtained and evaluated for qualitative and quantitative determinations of the elements present in the sampled volume.

EDS was used to identification of elemental composition of SnO₂ doped with 1.0wt%Sb₂O₃ sintered in air and N₂ atmosphere at grain and grain boundary.

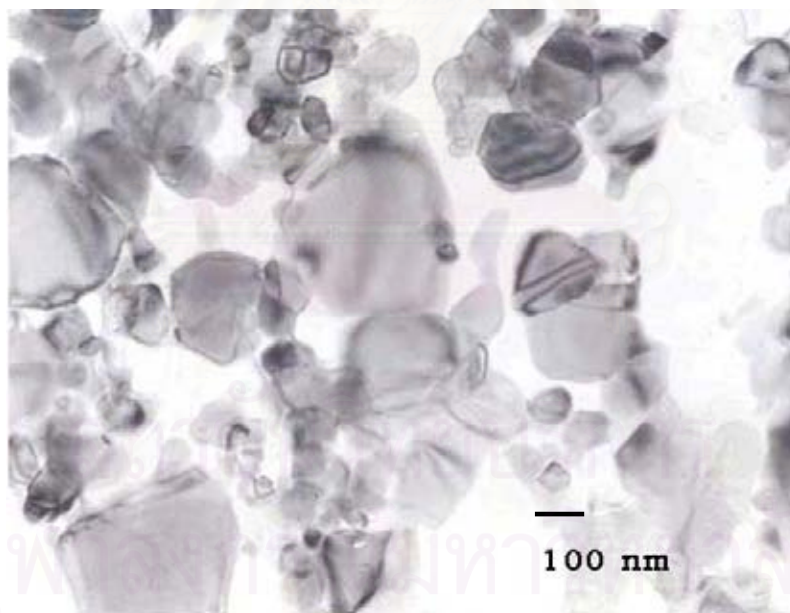
Figure 4.9 shows TEM micrographs of SnO₂ doped with 0.5wt%Sb₂O₃ sintered in air and N₂ atmospheres at 1000 °C for 1 hr. EDS spectrum of SnO₂ doped with 1.0wt% Sb₂O₃ sintered in air and N₂ atmosphere at grain and grain boundary are shown in Figure 4.10-4.11, respectively.

The samples exhibit a porous polycrystalline structure with a wide distribution of grain size. The average grain size of SnO₂ powder doped with 0.5wt%Sb₂O₃ is 50-375 nm.

It was found that the microstructure which is highly porous is similar in both specimens sintered in air and in N₂ atmosphere.



(a)



(b)

Figure 4.9 TEM micrographs of SnO₂ doped with 0.5 wt% Sb₂O₃; (a) sintered in air and (b) sintered in N₂ at 1000°C.

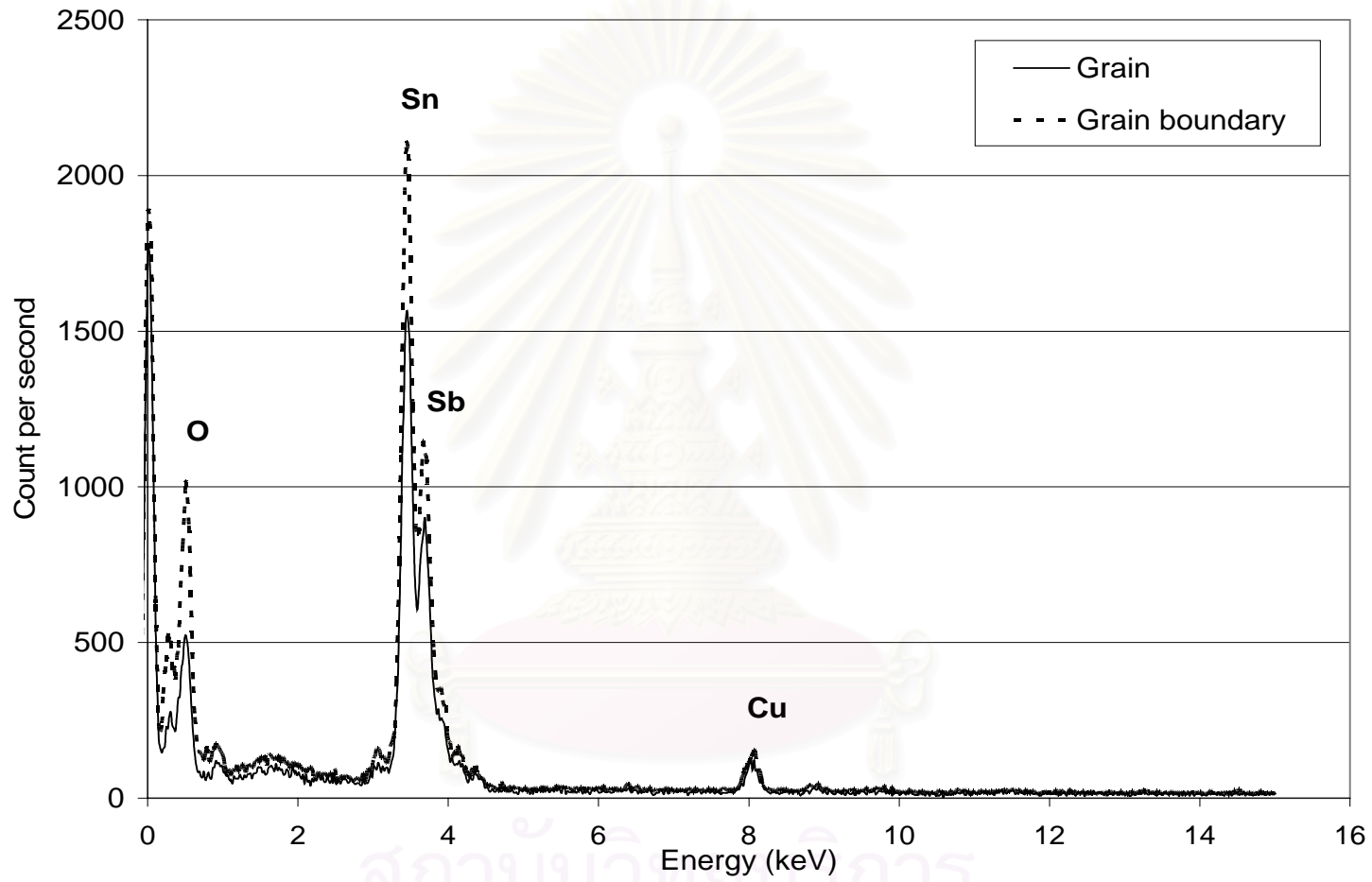


Figure 4.10 EDX analysis which show the comparison of EDX spectra taken from the grain and grain boundary of sample doped with 0.5 wt% Sb_2O_3 , sintered in air.

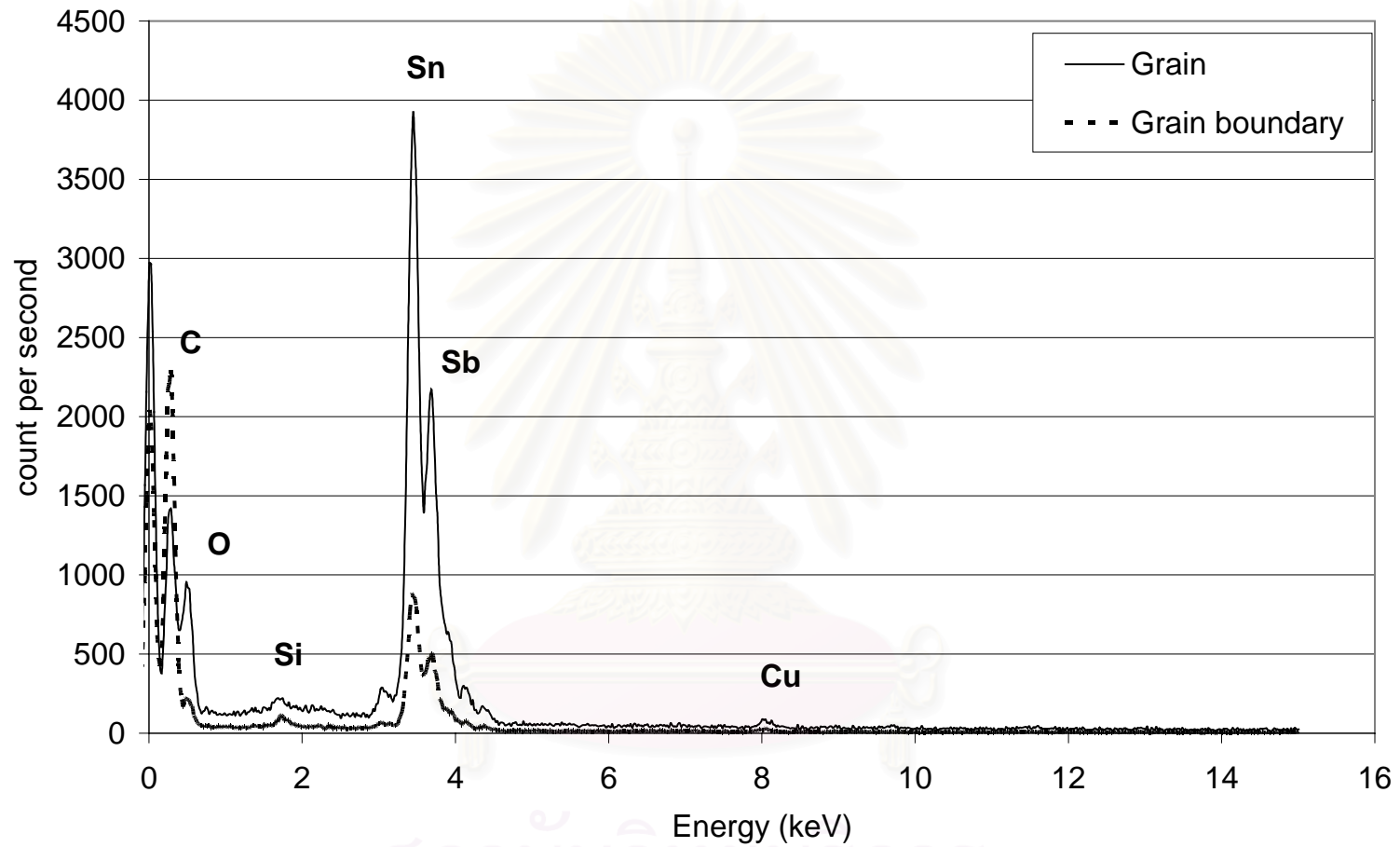


Figure 4.11 EDX analysis which show the comparison of EDX spectra taken from the grain and grain boundary of 0.5 wt% Sb_2O_3 -doped SnO_2 , sintered in N_2 .

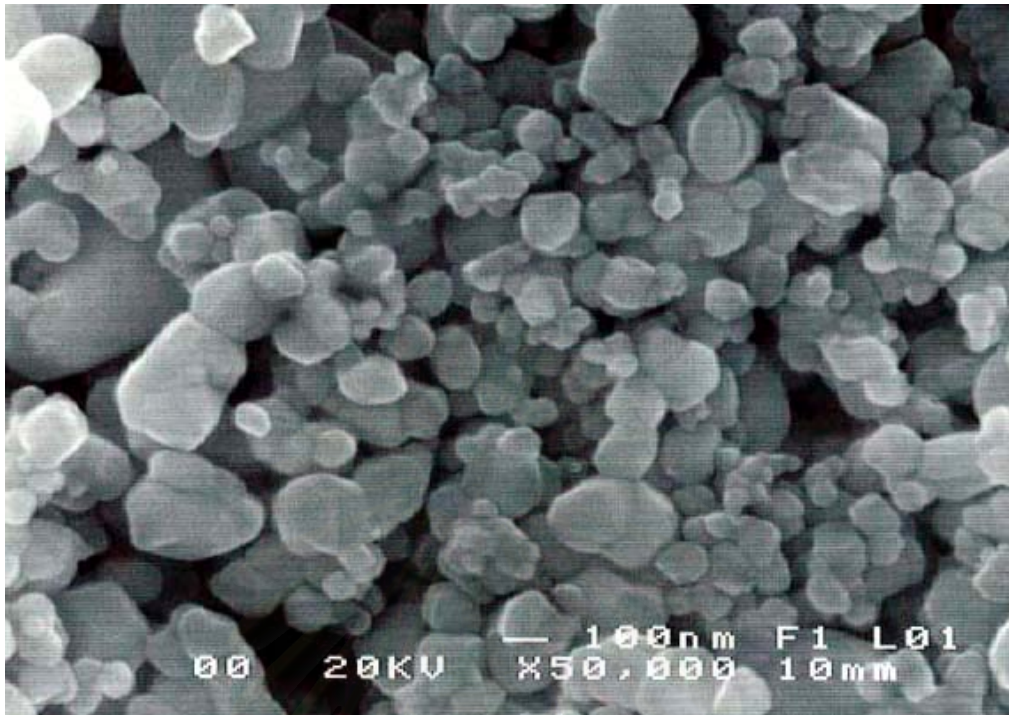
Figure 4.10 shows the EDS spectra of SnO₂ doped with 0.5wt% Sb₂O₃ sintered in air at grain and grain boundary. From the EDS spectrum of SnO₂ doped with 0.5wt% Sb₂O₃ sintered in air taken from grain and grain boundary shown in Figure 4.10, the X-ray spectrum features visible are Sn at energy of 3.447 keV, Sb at energy of 3.667 keV, O at energy of 0.507 keV and Cu at energy of 8.087 keV. The X-ray intensities of Sn, Sb and O peaks at grain boundary are higher than the intensities from inside the grain. This suggests that the amounts of Sn, Sb and O at grain boundary are higher than the amounts of Sn, Sb and O inside the grain. The presence of Cu came from the copper grid which supports the specimen.

From the EDS spectrum of SnO₂ doped with 0.5wt% Sb₂O₃ sintered in N₂ atmosphere taken from grain and grain boundary shown in Figure 4.11, the X-ray spectrum features visible are Sn at energy of 3.447 keV, Sb at energy of 3.687 keV, O at energy of 0.527 keV, Cu at energy of 8.147 keV, Si at energy of 1.767 keV and C at energy of 0.287 keV. EDS spectra taken from the grain and grain boundary of the sample sintered in N₂ atmosphere show that the X-ray intensities of Sn, Sb and O peaks inside the grain are higher than those at the grain boundary. This suggests that the amounts of Sn, Sb and O inside the grain are larger than the amounts of Sn, Sb and O at the grain boundary. Si peak detected came from the contamination and C peak came from carbon in PVA binder which remains in the SnO₂ sample.

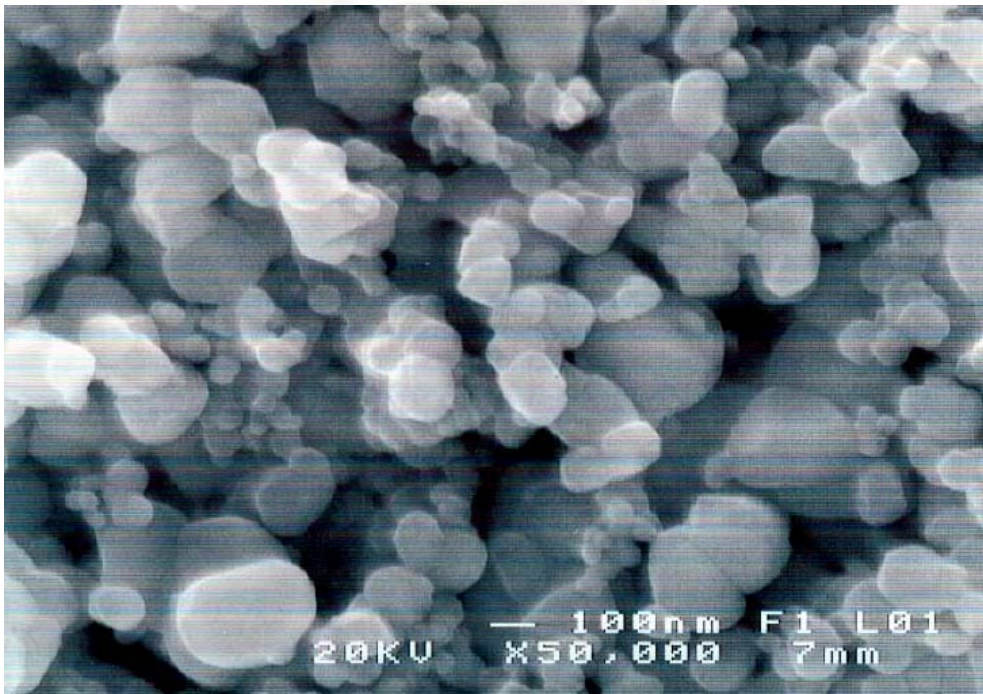
4.4 Effect of antimony oxide dopant concentration on the microstructure of tin oxide gas sensor

The purpose of this section is to study the effect of antimony oxide dopant concentration on the microstructure of tin oxide gas sensor. Figure 4.12 (a) and (b) show SEM micrographs of SnO₂ doped with 0.3wt%, and 0.5wt% Sb₂O₃ sintered in air at 1000 °C.

Both samples exhibit a porous polycrystalline structure with a wide distribution of grain size. The average grain size of SnO₂ powder doped with 0.3wt%, and 0.5wt% Sb₂O₃ is 50-250 nm and 50-300 nm, respectively. From this result, although the concentration of Sb₂O₃ dopant increases, the average grain size of the two samples are in the same range.



(a)



(b)

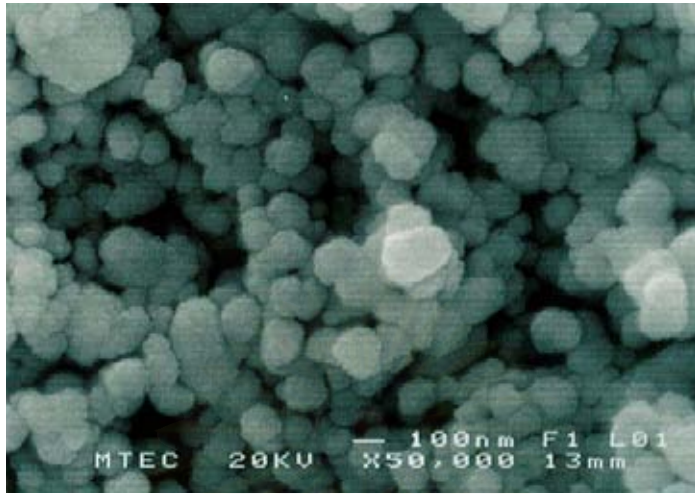
Figure 4.12 SEM micrographs of SnO₂ doped with (a) 0.3 wt% Sb₂O₃ and (b) 0.5wt%Sb₂O₃ sintered in air at 1000 °C.

4.5 Effect of binder concentration on the microstructure of tin oxide sensor

This section presents the study of the effect of binder concentration on the microstructure of SnO₂ sample added with 1.0-3.0 wt% PVA binder. The PVA binder is a polymer used for dry pressing process and it can be burnt out of SnO₂ sample during sintering process.

The microstructures of SnO₂ doped with 0.8wt%Sb₂O₃ added with 1.0-3.0 wt% PVA binder, sintered in air and N₂ atmospheres, are characterized by SEM and illustrated in Figure 4.13-4.14.

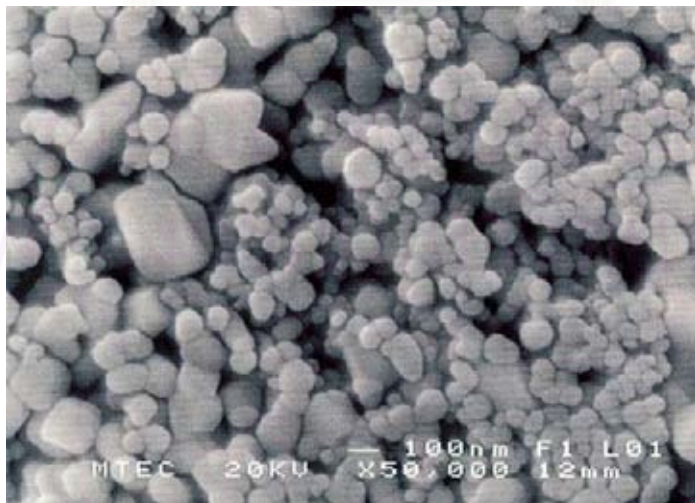
Figure 4.13 shows SEM micrographs of SnO₂ powder doped with 0.8wt%Sb₂O₃, sintered in air at 1000°C, (a) without binder, (b) added with 1.0wt%PVA and (c) added with 3.0wt%PVA. In Figure 4.13 (a) and (b), the samples exhibit a porous polycrystalline structure with grain size ranging from 50-250 nm. However, when the PVA binder increased to 3.0 wt% as shown in Figure 4.13(c), it is found that the sample exhibits a porous polycrystalline structure and average grain size is 50-350 nm. From this result, it is shown that the binder concentration has some effects on the microstructure. Moreover, the result of mercury porosimetry technique used for measuring of the surface area was performed and data taken from SnO₂ added with 1.0-3.0 wt% PVA binder, is shown in Table 4.4.



(a)



(b)



(c)

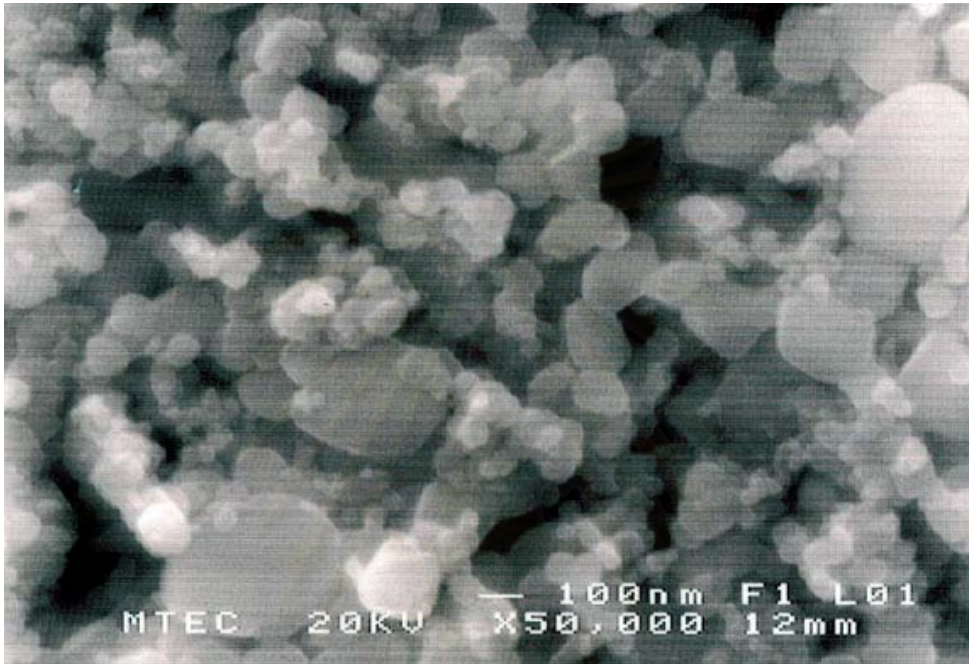
Figure 4.13 SEM micrographs of SnO₂ doped with 0.8 wt% Sb₂O₃ sintered in air at 1000°C, (a) without binder, (b) added with 1.0 wt% PVA and (c) added with 3.0 wt% PVA.

Table 4.4 Influence of the binder concentration on the surface area of SnO₂ samples.

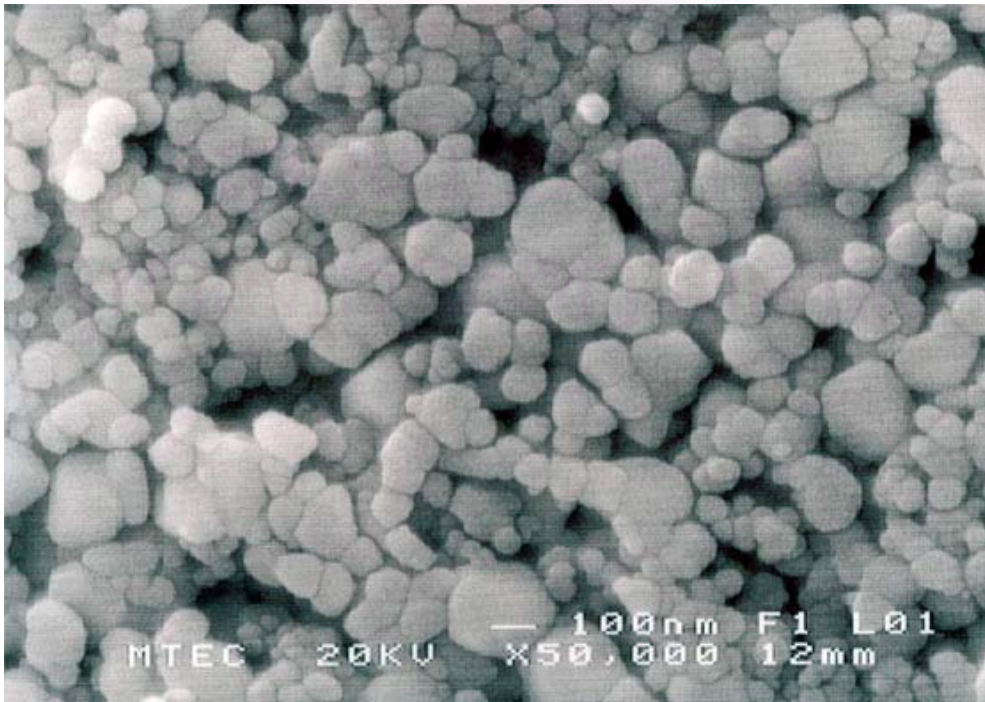
| Sample | Surface area (m ² g ⁻¹) |
|---|--|
| SnO ₂ without binder sintered in air | 2.96 |
| SnO ₂ added with 1.0wt%PVA binder sintered in air | 3.56 |
| SnO ₂ added with 3.0wt%PVA binder sintered in air | 3.75 |
| SnO ₂ added with 3.0wt%PVA binder sintered in N ₂ | 3.29 |

From Table 4.4, the surface area of SnO₂ without binder sintered in air is 2.96 m²g⁻¹. The surface area of SnO₂ sensor increases with concentration of PVA binder as follows : surface area of SnO₂ added with 1.0 wt%PVA sintered in air is 3.56 m²g⁻¹ and surface area of SnO₂ added with 3.0 wt%PVA sintered in air is 3.75 m²g⁻¹. For SnO₂ with 3.0 wt%PVA was sintered in N₂, it is found that the surface area is 3.29 m²g⁻¹ which is less than surface area of SnO₂ with the same amount of PVA sintered in air. The microstructures of SnO₂ added with 1.0 wt% and 3.0 wt%PVA sintered in N₂ are shown in Figure 4.14 (a)-(b).

From this result, it can be suggested that the SnO₂ sensors added with various binder concentrations exhibit a porous polycrystalline structure with a wide distribution of grain size. The average grain sizes of SnO₂ samples added with 1.0 wt% and 3.0 wt%Sb₂O₃ are 50-250 nm and 50-350 nm, respectively. The surface area of SnO₂ sensor sintered in air increases with PVA binder concentration. However, SnO₂ added with 3.0 wt%PVA binder sintered in N₂ has less surface area than samples sintered in air. Because in the SnO₂ sample which was sintered in air, the PVA binder was burnt out more readily than that in N₂ atmosphere.



(a)



(b)

Figure 4.14 SEM micrographs of SnO_2 doped with 0.8 wt% Sb_2O_3 sintered in N_2 at 1000°C , (a) added with 1.0 wt% PVA and (b) added with 3.0 wt% PVA.

4.6 Effect of sintering atmosphere on the gas sensitivity

In this section the effect of sintering atmosphere on the gas sensitivity was studied. From literature review, the SnO_2 sensor is n-type semiconductor and its electrical conduction is resulted from oxygen vacancies. The electrical conductance of SnO_2 sensor sintered in different atmosphere were investigated because different sintering atmosphere have an effect on the amount of oxygen vacancies in SnO_2 sensor. Gas sensitivity at operating temperature 350°C of SnO_2 doped with 0.3 wt% Sb_2O_3 and added with 3.0 wt% PVA binder sintered in air and N_2 atmosphere was studied, and is shown in Figure 4.15.

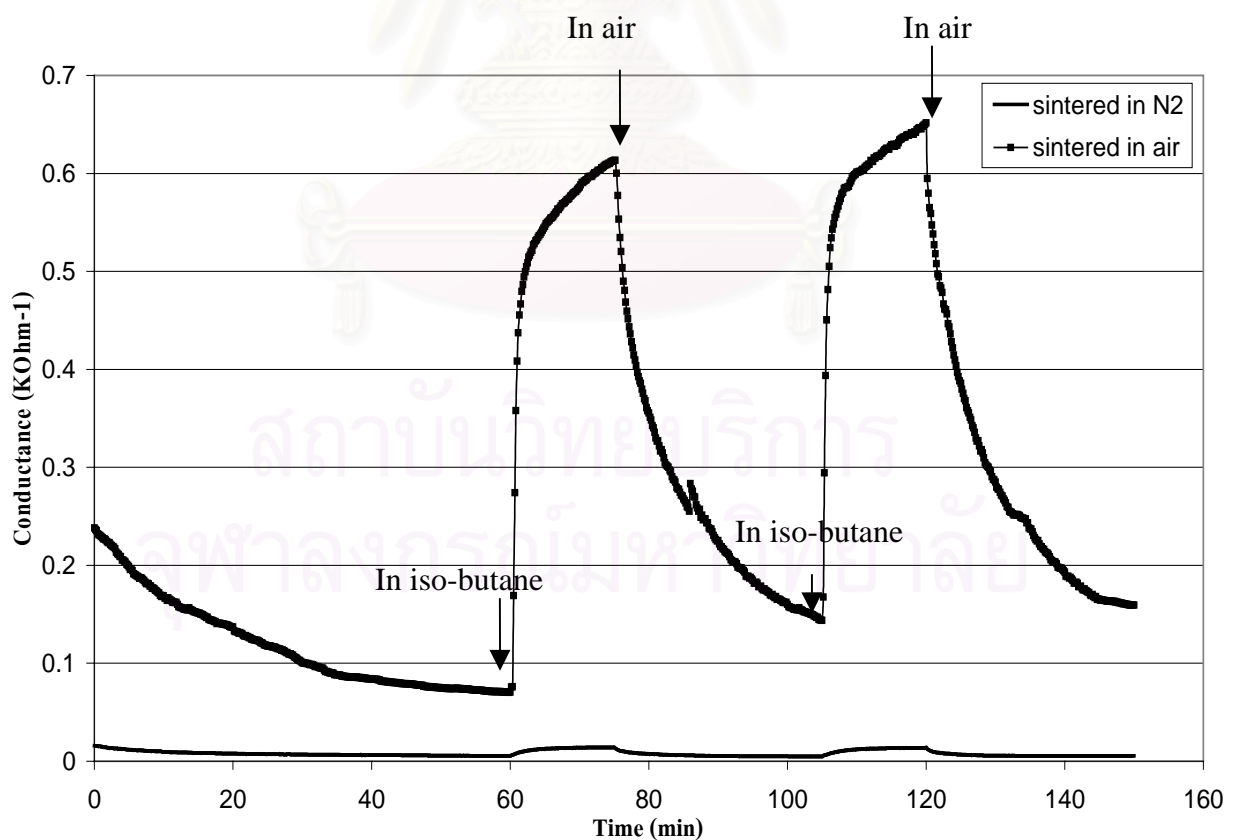


Figure 4.15 Electrical response of SnO₂ doped with 0.3 wt% Sb₂O₃ added with 3.0 wt% PVA binder sintered in air and N₂ atmospheres at 1000°C for 1 hour.

From Figure 4.15, SnO₂ sensor was exposed under dry air for 60 min (at 0-60 min) after that it was exposed to iso-butane gas for 15 min (at 61-75 min) then SnO₂ was exposed to dry air again for 30 min (at 75-105 min).

From these result, the conductance curves of SnO₂ sensor sintered in air and N₂ atmospheres display a change depending on the atmosphere (dry air or iso-butane) because of the reaction of electron in the SnO₂ surface with the molecule of gas as discussed in chapter 2, section 2.3. However, it is found that the SnO₂ sensor sintered in air showed much better gas response to iso-butane than sample sintered in N₂. The response time of SnO₂ sensor sintered in air is 1 min and recovery time is 15 min. From Novel, S.⁴⁶ who studied the influence of grain size and working temperature on the performance of a sensor produced from polycrystalline tin dioxide, the response time of SnO₂ sensor is about 1 min.

The result, it is suggested that the structure of SnO₂ sensor sintered in air be enriched with the oxygen vacancies in the structure. Therefore a larger scale of reaction between molecules of iso-butane gas with oxygen ions adsorbed on the surface occurs. Hence, the ability of gas response of SnO₂ sensor sintered in air to iso-butane gas is much better than the SnO₂ sensor sintered in N₂ atmosphere.

4.7 Effect of antimony oxide dopant concentration on the gas sensitivity

The influence of dopant concentration on the gas response under iso-butane at operating temperature of 350°C for SnO₂ doped with 0.3, 0.5, 0.8 and 1.0wt%Sb₂O₃ sintered in air can be observed in Figures 4.16 - 4.17.

Figure 4.18, the influence of dopant concentration on the sensitivity of SnO₂ sensor sintered in air and N₂ atmospheres when studied in air and in iso-butane gas at temperature of 300, 350 and 400°C.

From Eq. 2.1, the gas sensitivity S_G of a sensor is commonly defined as the ratio of its resistance in air, R_a , to that in gas, R_s .

$$S_G = \frac{R_a - R_s}{R_a}$$

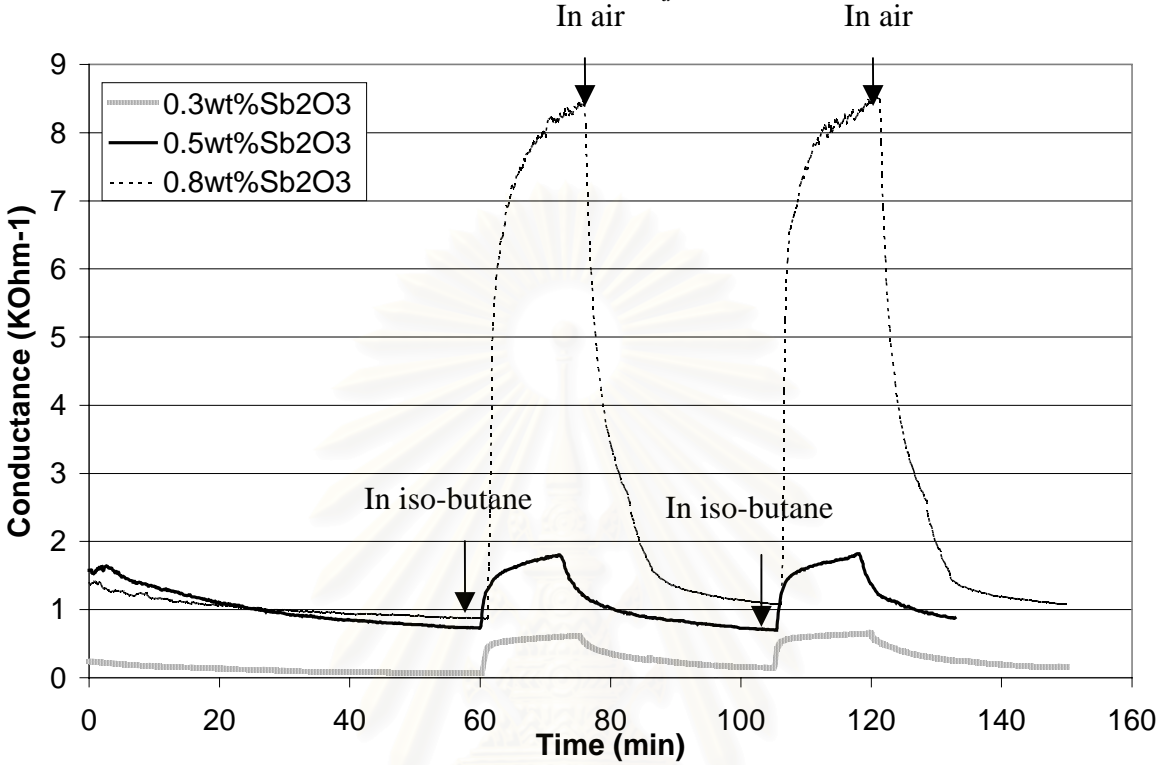


Figure 4.16 Electrical response of SnO₂ doped with 0.3, 0.5 and 0.8 wt% Sb₂O₃ sintered in air at 1000°C for 1 hour.

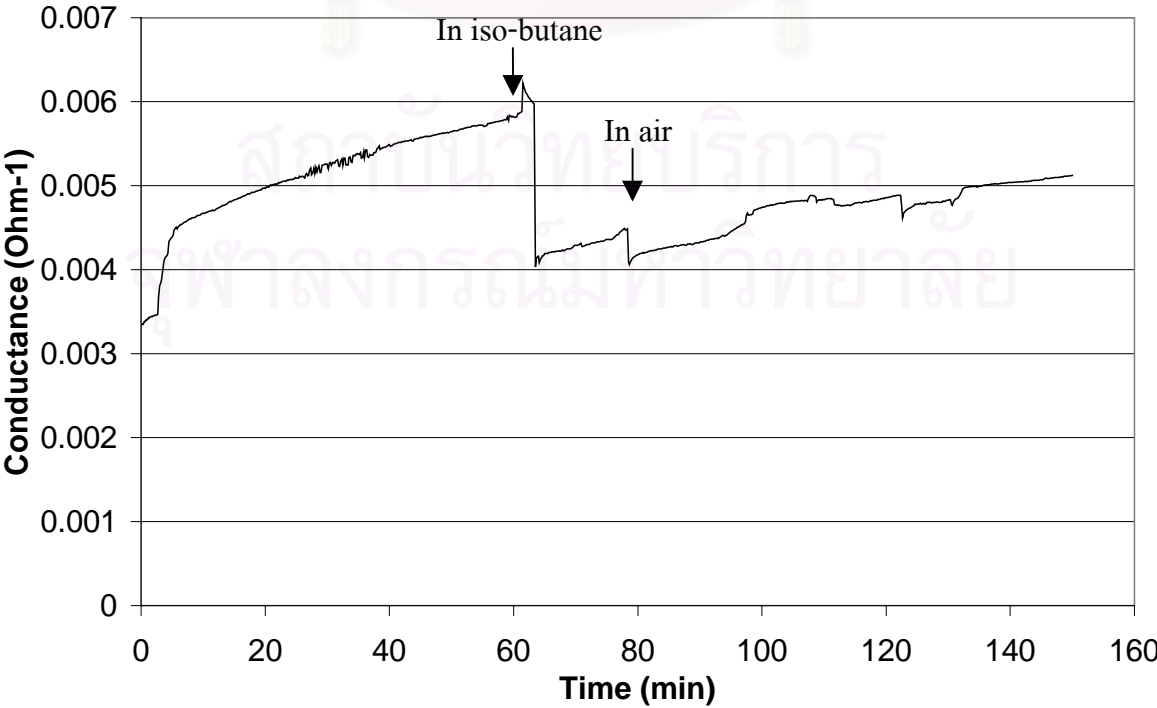


Figure 4.17 Electrical response of SnO₂ doped with 1.0 wt% Sb₂O₃ sintered in air at 1000°C for 1 hour.



สถาบันวิทยบริการ
จุฬาลงกรณ์มหาวิทยาลัย

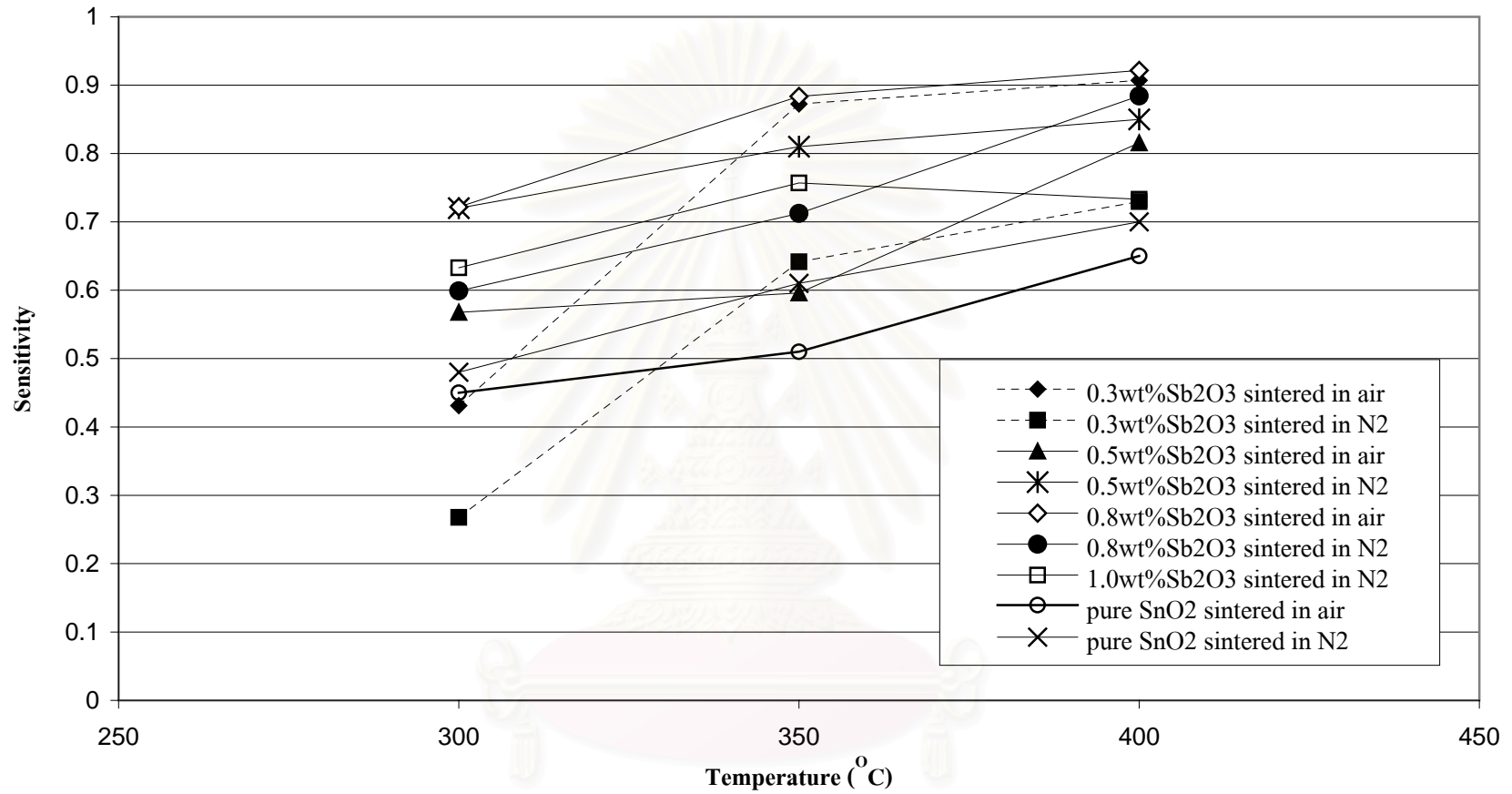


Figure 4.18 Sensitivity as a function of operating temperature of SnO₂ doped with 0.3, 0.5, 0.8 and 1.0 wt% Sb₂O₃ sintered in air and N₂ atmosphere at 1000°C for 1 hour

Figure 4.16-4.17 show the electrical conductivity of Sb_2O_3 -doped SnO_2 , sintered in air. The electrical conductivity was measured in iso-butane at 350°C . From Figure 4.16, it can be seen that the electrical conductance increases under iso-butane atmosphere. The time response is about 3 minutes after exposing to iso-butane gas. Moreover, the SnO_2 doped with 0.8wt% Sb_2O_3 sintered in air shows better gas response than SnO_2 doped with 0.3wt%, 0.5wt% and 1.0wt%, which correlates with the sensitivity characteristics shown in Figure 4.18.

The gas sensitivity of Sb_2O_3 -doped SnO_2 to iso-butane was investigated and the results are shown in Figure 4.18. It is found that the sensitivity increases with the operating temperature. Additionally, it is observed that the SnO_2 doped with 0.8 wt% Sb_2O_3 sintered in air exhibits the highest sensitivity to iso-butane. The sensitivities are 0.92 at 400°C and 0.88 at 350°C . The results show that when the dopant concentration increases from 0.3 wt% to 0.8 wt%, the sensitivity increases. However, when the dopant concentration reaches 1.0 wt%, the sensitivity decreases and does not show good gas response, as shown in Figure 4.17. This results agree well with previous work by Phani A.R.⁴⁴.

Phani A.R.⁴⁴ studied the preparation, characterization and electrical properties of SnO_2 based liquid petroleum gas sensor. This work showed that for SnO_2 sensor prepared by coating of slurry on alumina tube sintered at 800°C , the sensitivity of pure SnO_2 at operating temperature 350°C was 0.57, SnO_2 doped with 0.5 wt%Pd was 0.69 and SnO_2 doped with 1.0 wt% Pd was 0.71. However, it was found that SnO_2 doped with 1.5 wt% Pd had highest sensitivity (0.95) and further increase in Pd concentration drastically decreased the sensitivity towards LPG.

Moreover, Wei Liu³⁹ studied the influence of many different additives on the electronic structure of SnO_2 thin film. It was found that the kind of dopant Pd, Sb, Pt or In hardly changed the grain size of SnO_2 thin films with low doping amount, but they did change the Fermi level of SnO_2 . The dopant Sb increased the fermi level by ~ 0.25 eV, but In and Pd decrease it by ~ 0.2 eV and ~ 0.1 eV, respectively and Pt did not change Fermi level.

The electrical conductance of SnO₂ sensor sintered in N₂ atmosphere under iso-butane is shown in Figure 4.20. It is also found that, when the SnO₂ sensors were exposed to iso-butane gas, the electrical conductance increase like that of SnO₂ sensor sintered in air as shown in Figure 4.16. However, the time response of SnO₂ sensor sintered in N₂ is about 2 minutes after exposure to iso-butane gas, which is less than that of the specimens sintered in air.

From the sensitivity measurements, it is found that doped SnO₂ sintered in air shows better sensitivity than samples sintered in N₂ atmosphere. Furthermore, the conductivity of SnO₂ doped with Sb₂O₃ sintered in air is higher than samples sintered in N₂ atmosphere, as illustrated in Figure 4.19. The conductance of SnO₂ samples sintered in air is 1 - 10 KOhm⁻¹ but the conductance of SnO₂ sample sintered in N₂ atmosphere is 0.001-0.016 KOhm⁻¹. Therefore, the efficiency of gas detection of sample sintered in air to iso-butane gas is higher than the samples sintered in N₂ atmosphere. However, the samples sintered in N₂ atmosphere show quicker response time and recovery time than sample sintered in air.

From the results of gas response shown in Figure 4.16-4.19, it is found that the conductance of SnO₂ increases with Sb₂O₃ dopant concentration conforming with the literature review⁴⁵⁻⁴⁷ that the presence of antimony change the electrical properties of SnO₂. SnO₂ is well known as an oxygen deficient n-type semiconductor, the electronic conduction that has been attributed to oxygen vacancy donor levels can be increased by reduction. The addition of a small percentage (1-3wt%) of antimony results in a dramatic increase in the electrical conductivity. This phenomenon, shown by single crystals, thin films and polycrystalline samples was specifically explained through the increase of the number of free electrons resulting from antimony substitution into SnO₂ lattice. Changes in conductivity of antimony-SnO₂ associated with the interaction with reducing gases provide the basis for application of these systems as sensor for hydrocarbon (ie. iso-butene gas) or Co detection.

The possibility is that, the pentavalent ions (Sb⁵⁺) substitute into the SnO₂ lattice, and the carrier concentration (electrons) would increase. The antimony acts as

an effective donor, so that the Debye length of SnO_2 would decrease and resistivity decrease or conductivity increase.

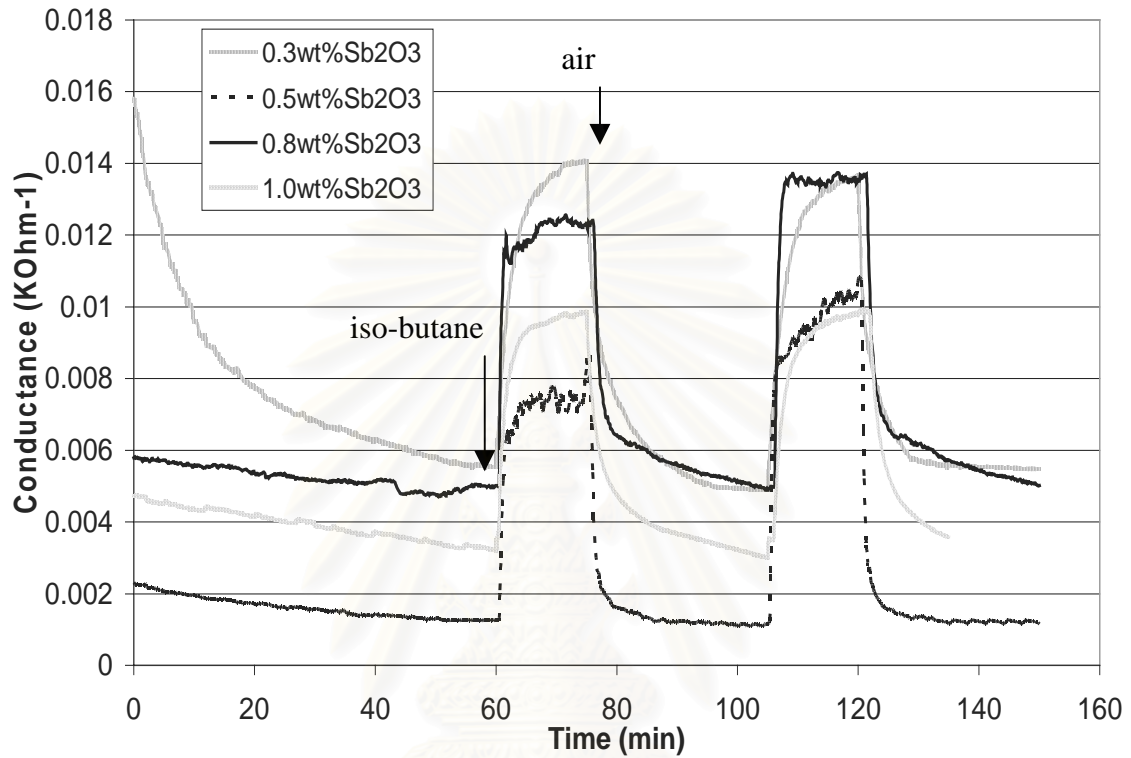


Figure. 4.19 Electrical response of SnO_2 doped with 0.3, 0.5, 0.8 and 1.0 wt% Sb_2O_3 sintered in N_2 atmosphere at 1000°C for 1 hour.

สถาบันวิทยบริการ
จุฬาลงกรณ์มหาวิทยาลัย

4.8 Effect of binder concentration on the gas sensitivity

In this section, the effects of binder concentration on the sensitivity of SnO₂ gas sensor will be investigated.

The gas sensitivities of SnO₂ doped with 0.8 wt% Sb₂O₃ added with various concentrations of PVA are shown in Figure 4.20.

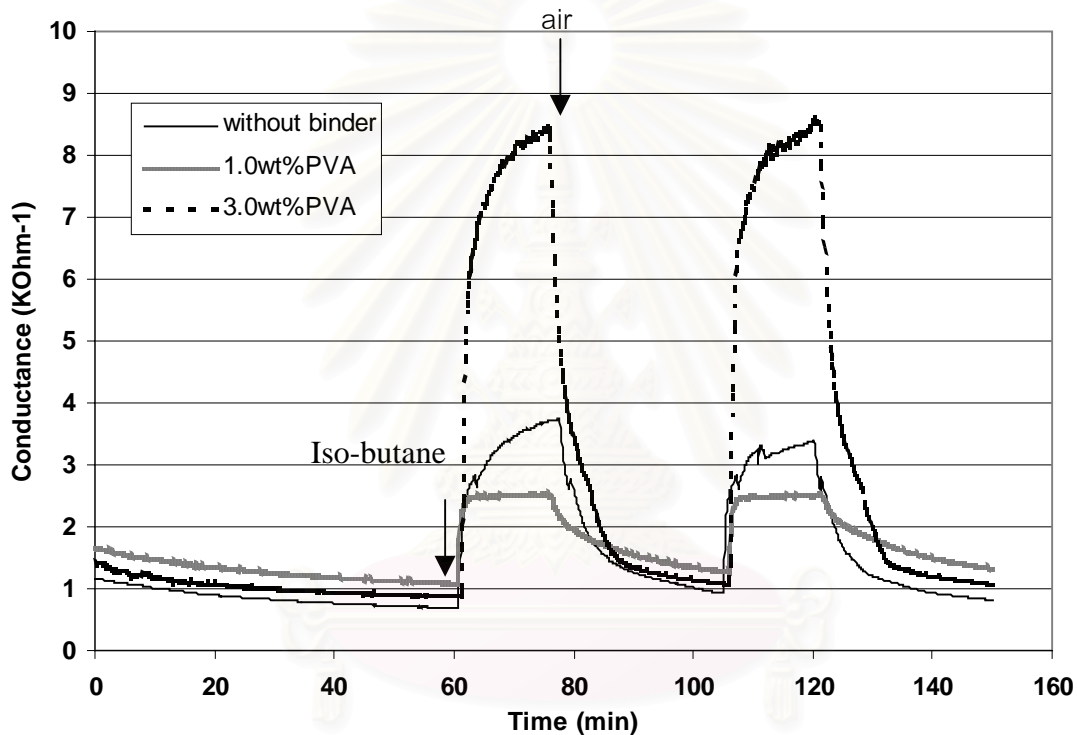


Figure 4.20 Electrical response of SnO₂ doped with 0.8 wt% Sb₂O₃ and added with various concentrations of PVA binder sintered in air at 1000°C for 1 hour.

The gas sensitivities of Sb₂O₃-doped SnO₂ with no binder and with 1.0-3.0wt% PVA binder to iso-butane have been investigated and the results are shown in Figure 4.20. The electrical conductivity was measured in iso-butane at 350°C. From Figure 4.21, it is found that the gas response of samples with 3.0 wt% PVA binder is better than samples without binder and that with 1.0 wt% PVA binder.

The time response of SnO₂ sample added with 3.0wt% binder sintered in air is about 2 minutes after exposure to iso-butane gas. The recovery time is about 10 minutes.

From Figure.4.12 and Table 4.7, it is found that the surface area of SnO₂ sensor increases with PVA binder concentration. Therefore, the SnO₂ sensor added with 3.0 wt% PVA shows the highest gas response because of its high surface area.

4.9 The effect of thickness of SnO₂ sensor on gas sensitivity

In this section, the effect of thickness of SnO₂ sensor (1.0mm and 2.0 mm) on gas sensitivity is studied.

The gas sensitivity of SnO₂ doped with 0.8wt% Sb₂O₃ pellet of 1.0 mm and 2.0 mm thickness sintered in air is shown in Figure 4.21.

From Figure 4.21, it was found that the gas sensitivity of 1.0 mm thickness sintered show curve of gas response change more than SnO₂ sensor, 2.0mm thickness. However, this results show that the thickness of sensor between 1.0 mm and 2.0 mm no high significant on gas sensitivity.

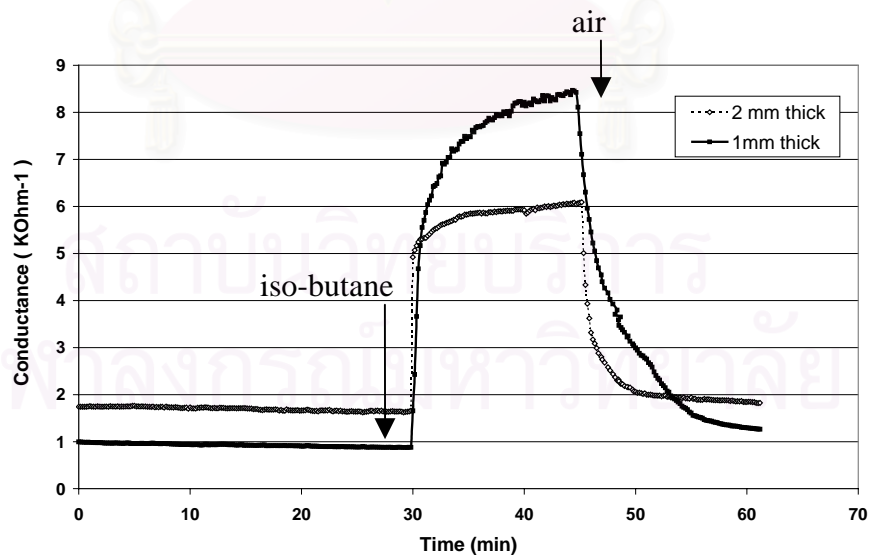


Figure 4.21 Electrical response of SnO₂ doped with 0.8wt% Sb₂O₃, 1.0 mm and 2.0 mm thickness, sintered in air at 1000°C for 1 hour.

4.10 Surface analysis

The ability of a solid state gas sensor to sense the presence of a particular gas depends on the nature of interaction, be it chemical or electrical between the gas molecules and the surface of the sensing material. It is well known that the reactivity of a surface is critically dependent on the condition of the surface, that is, on its doping, impurity constituents, and on its electronic and defect structure. This section will present the study of surface analysis of SnO₂ gas sensor by X-ray Photoelectron Spectroscopy and Ultra-violet Photoelectron Spectroscopy techniques.

4.10.1 XPS analysis

In X-ray Photoelectron Spectroscopy (XPS), the energy of exciting X-radiation is high enough to eject electron from several shallow core levels. The survey XPS scans of the surfaces of SnO₂ doped with 1.0 wt% Sb₂O₃ sintered in air and N₂ atmospheres, using MgK_α radiation, are shown in Figure 4.22 –4.23.

From the XPS spectra taken from SnO₂ doped with 1.0 wt% Sb₂O₃ shown in Figure 4.22-4.23, the photoelectron features visible are the Sn 3s, 3p, 3d and the O 1s peaks from the surface. However, no peak corresponding to Sb is observed, due to the detection limit of the instrument. The detection limit of the instrument is 3.0 wt% of doping concentration.

From the peak intensity shown in Figure 4.22-4.23, it is found that the peak intensity of O 1s the of sample sintered in air is higher than the sample sintered in N₂ atmosphere. Therefore, samples sintered in air has more oxygen atoms than samples sintered in N₂ atmosphere. In addition, when the SnO₂ samples sintered in air are exposed to the combustion gas (i.e. iso-butane) their response to combustion gas is better than SnO₂ samples sintered in N₂. This has already been discussed in more in details in section 4.6.

Figure 4.24 shows a detailed XPS spectrum of the Sn 3d_{5/2} and Sn 3d_{3/2} peaks of sample sintered in air and N₂. The observed Sn 3d_{5/2} and Sn 3d_{3/2} core-level spectra of SnO₂ doped with 1.0 wt% Sb₂O₃ sintered in air and N₂ atmospheres are

similar. The binding energies of Sn 3d_{5/2} and Sn 3d_{3/2} sintered in air are 483.2 eV and 491.8 eV, respectively. The binding energies of Sn 3d_{5/2} and Sn 3d_{3/2} sintered in N₂ atmosphere are 490.4 eV and 498.8 eV, respectively.

From the study of Goggiotti⁴⁹ (Figure 4.25), the two components of Sn 3d_{5/2} line correspond to the Sn⁴⁺ and Sn²⁺ species with binding energy (E_B) of 486.7 eV and 485.4 eV, respectively. In contrast, the splitting of Sn 3d_{5/2} spectrum as shown in Figure 4.24 cannot be observed. From the experimental results, the position of the Sn 3d_{5/2} spectra of SnO₂ doped with 1.0 wt% Sb₂O₃ sintered in air and N₂ atmospheres correspond to the binding energy (E_B) of 483.2 eV and 490.4 eV, respectively. This suggests that oxidation states of SnO₂ sample is 4⁺ and/or 2⁺. The different positions of the Sn 3d peak in doped SnO₂ sintered in air and N₂ atmospheres may be due to the effect of sintering.

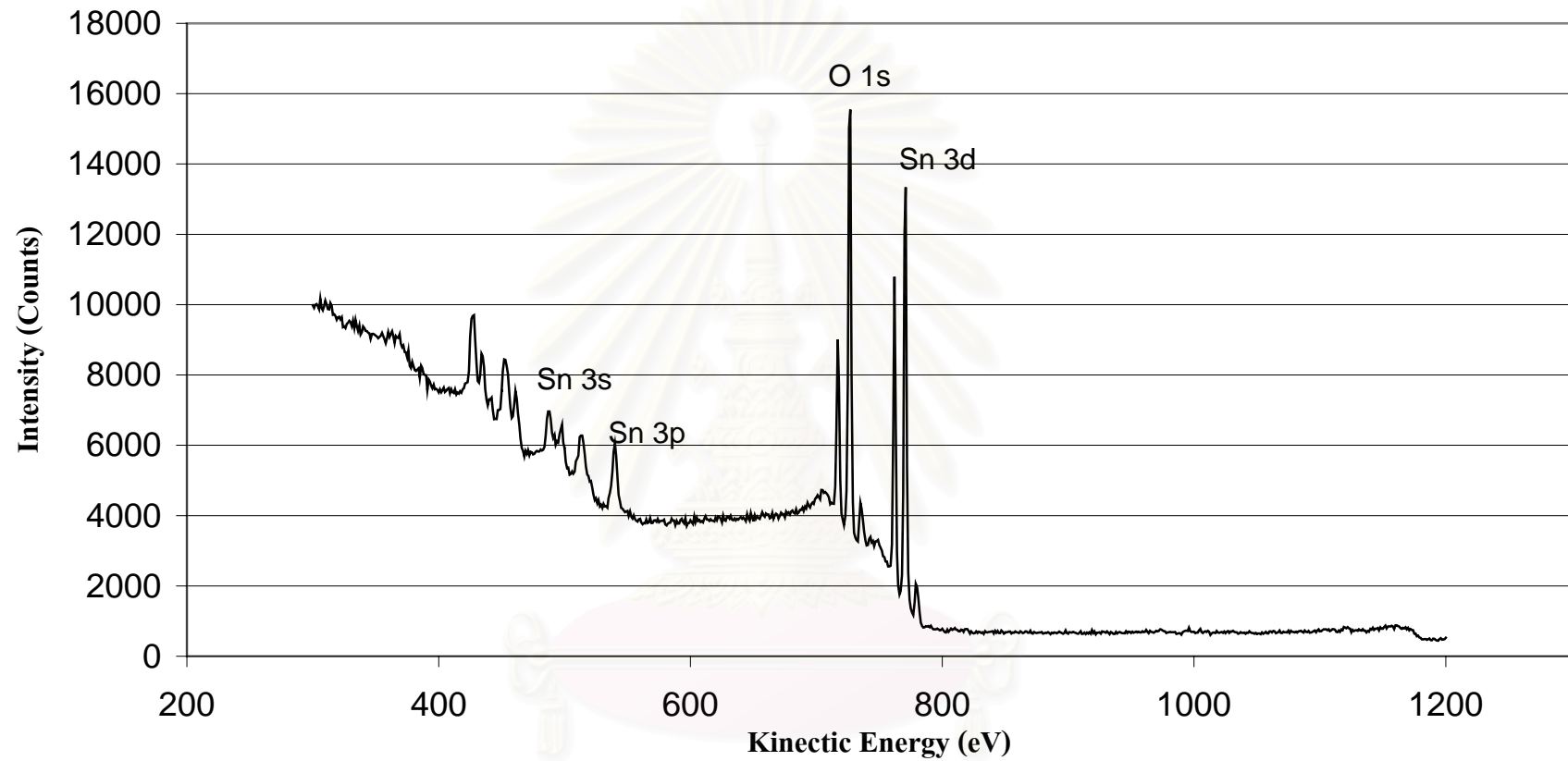


Figure 4.22 XPS spectrum of SnO_2 doped with 1.0wt% Sb_2O_3 sintered in air at $1,000^\circ\text{C}$, shows the photoelectron features visible of the Sn 3s at energy is 498 eV, 3p is 540 eV, 3d is 771 eV and the O 1s is 727 eV peak from the surface.

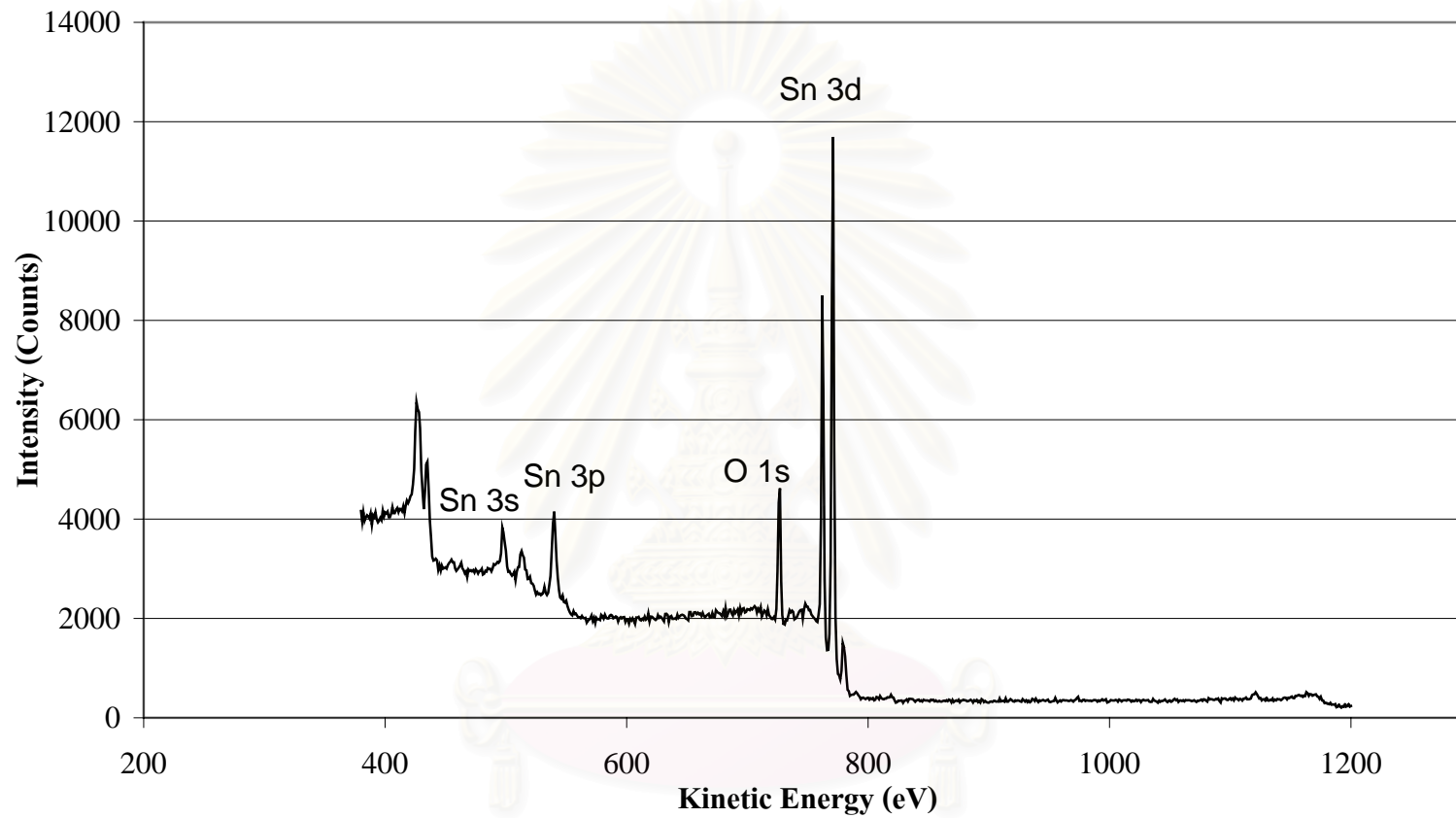


Figure 4.23 XPS spectrum of SnO_2 doped with 1.0wt% Sb_2O_3 sintered in N_2 at $1,000^\circ\text{C}$, shows the photoelectron features visible of the Sn 3s at energy is 498 eV, 3p is 540 eV, 3d is 771 eV and the O 1s is 727 eV peak from the surface.

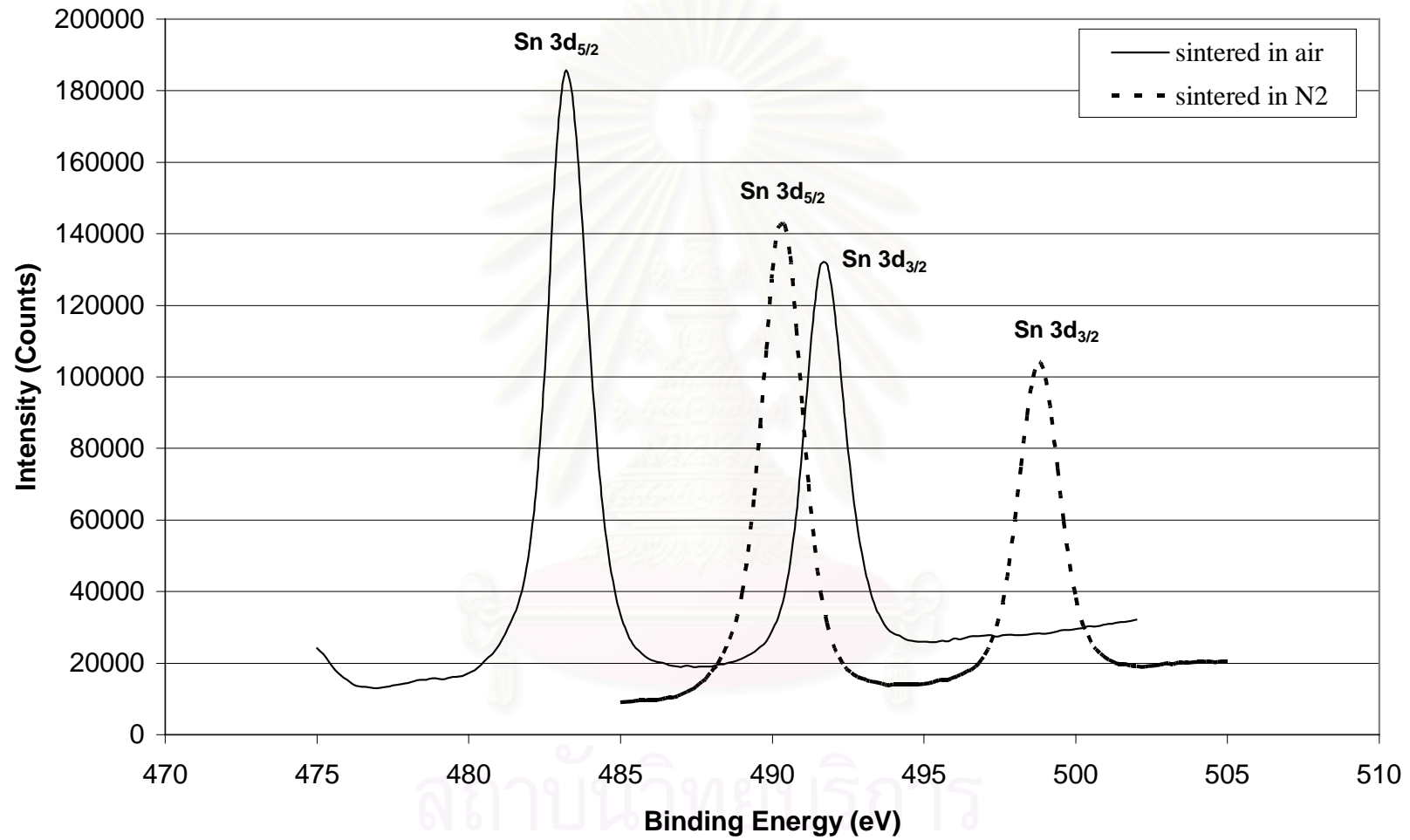


Figure 4.24 XPS spectra of Sn 3d_{5/2} and 3d_{3/2} peak of SnO₂ doped with 1.0wt% Sb₂O₃ sintered in air and N₂ atmosphere at 1000°C

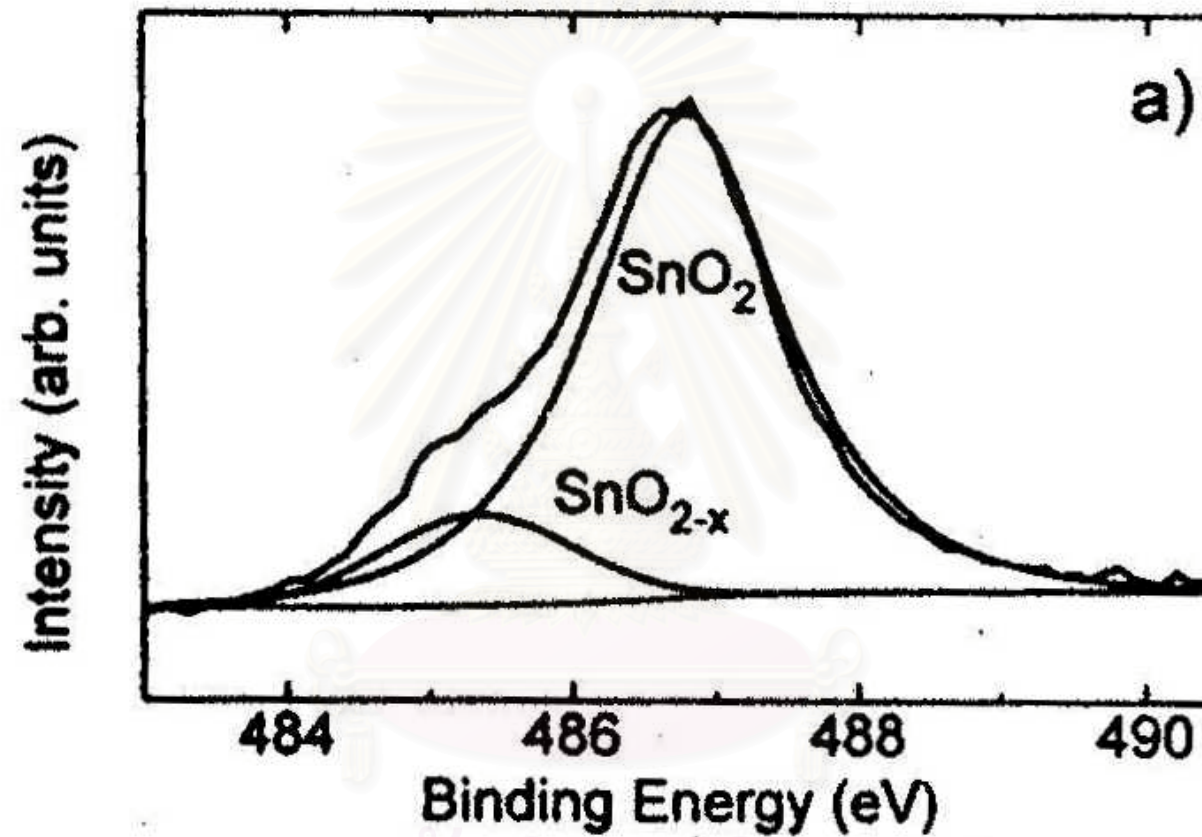


Figure 4.25 XPS spectra of Sn 3d_{5/2} from Pt/SnO_x film.⁴⁹

4.10.2 UPS analysis

In Ultra-violet Photoelectron Spectroscopy (UPS) technique, the energy of the exciting ultraviolet photons is much lower than X-ray in XPS technique and the photoelectrons are ejected from the valence band.

Figure 4.25 shows UPS spectra from the valence-band of undoped SnO₂ and 1.0 wt% Sb₂O₃ doped SnO₂ sintered in air and N₂ atmospheres. In Figure 4.25, the graph is plotted between kinetic energy and the intensity of undoped SnO₂ and doped with 1.0wt%Sb₂O₃ sintered in air and N₂. In this experiment, Helium lamp, emitting at 21.2 eV (He I radiation) was used and the work function of the instrument was 4.2 eV. The Fermi level can be determined by $E_k = h\nu - E_B$ (Eq.3.7); at Fermi level, the binding energy is zero.

$$\begin{aligned} \text{So that; Fermi level } (E_k) &= 21.2 \text{ eV} - 4.2 \text{ eV} \\ &= 17.0 \text{ eV} \end{aligned}$$

In Figure 4.25, the peak near Fermi level (17.0 eV) cannot be observed, due to the detection limit of the instrument.

From a study by Cox *et al* (1982)⁴⁷, the UPS spectra taken from pure SnO₂ and 3.0 wt% Sb doped using He(I) source were shown. In the UPS spectrum, there was no significant differences, except very close to the Fermi level where at high amplification a very small peak in the spectrum from the Sb-doped SnO₂ was found. No such peak under the same conditions was found in pure SnO₂. The additional peak in the doped oxide was attributed to the introduction of electrons into the conduction band by Sb doping.

The zero of binding energy is at the Fermi level. The shapes of all four spectra are similar. But, for sample doped with 1.0 wt% Sb₂O₃, sintered in N₂, the background is high and additional peak around 9-10 eV is observed. Sb doping⁴¹ attributed the additional peak in the doped oxide to the introduction of electrons into conduction band. However, in this study, this peak was not observed which may be due to the detection limit of the instrument.

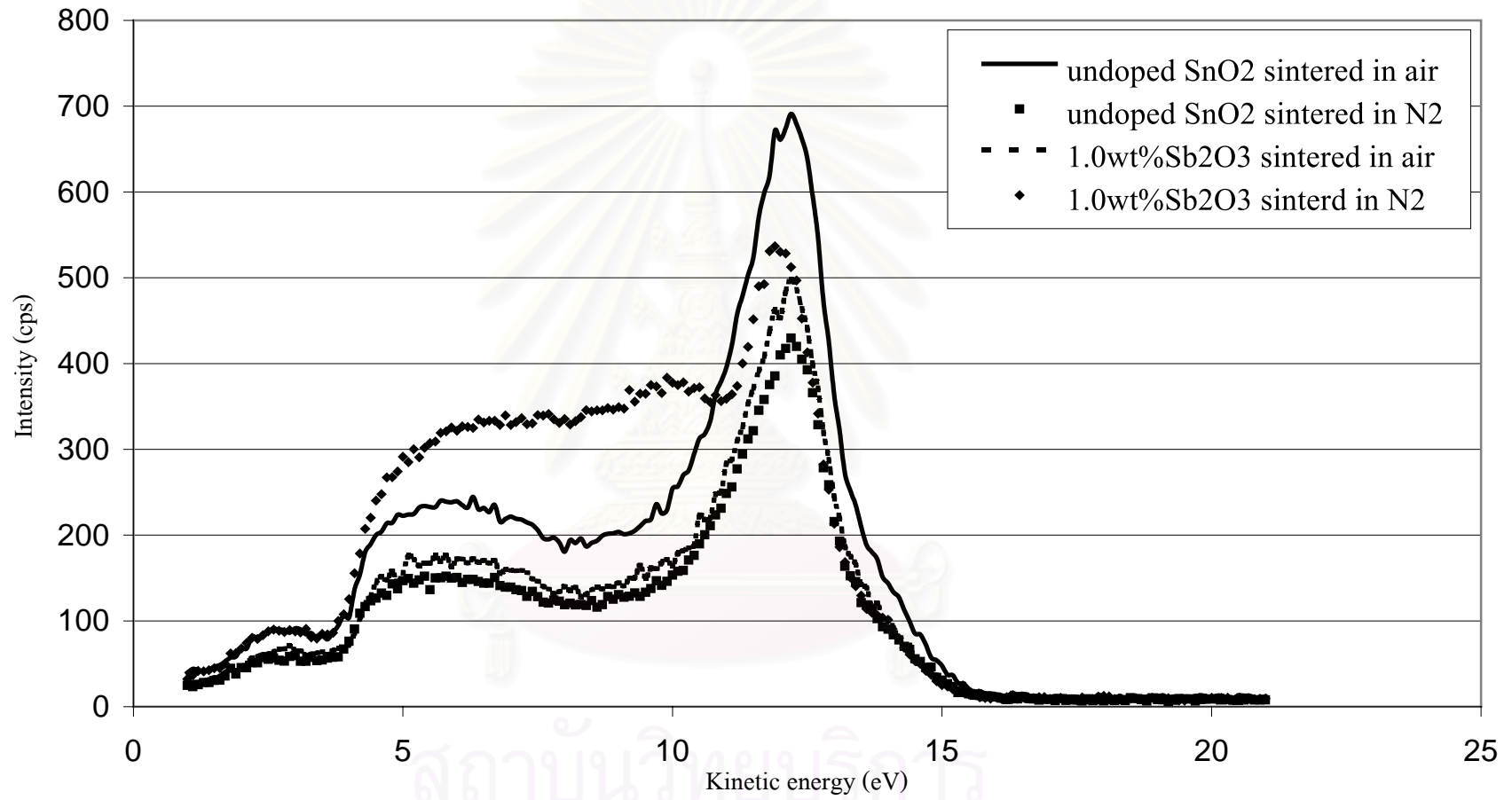


Figure 4.26 UPS spectra of SnO₂ which is undoped and doped with 1.0wt%Sb₂O₃ sintered in air and N₂.

CHAPTER 5

Conclusions and Recommendations

5.1 Conclusions

The conclusions of the present research are the following:

1. From SEM and TEM study, the microstructure of SnO₂ doped with Sb₂O₃ dopant is porous structure.
2. From the gas sensitivity study versus operating temperature and dopant concentration, it was found that the gas sensitivity increases with the operating temperature and Sb₂O₃ dopant concentration increase that the optimal Sb₂O₃ dopant concentration show exhibits the highest sensitivity is 0.8wt%Sb₂O₃.
3. Results from the effect of sintering atmosphere on gas sensitivity indicated that the SnO₂ sensor sintered in air show better gas sensitivity than SnO₂ sensor sintered in N₂ atmosphere. It is thought that the structure of SnO₂ sensor sintered in air is enriched with the oxygen vacancies and the reaction between molecules of iso-butane gas with oxygen ion absorbed on the surface occurs highly.
4. From surface structure analysis by XPS and UPS, it was found that the oxidation state of Sn present is Sn²⁺ and/or Sn⁴⁺.

5.2 Recommendations for future studies

From the previous conclusions, the following recommendations for the future studies are proposed.

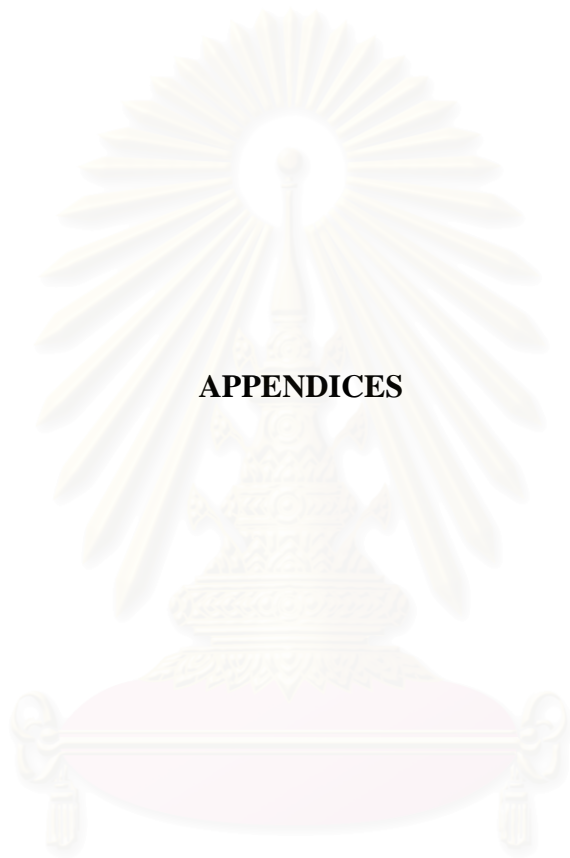
1. Study the phase transformation of Sb-SnO₂ by thermal analysis at various temperatures because at sintering (1000°C) no phase transformation of Sb-SnO₂ was observed.
2. Investigate the effect of other dopants such as Pd or Al to compare the sensitivity characteristic with Sb-doped SnO₂.
3. Apply of new fabrication method such as thick film and thin film besides the conventional oxide mixing method to improve the sensitivity, stability and reproducibility of the sensor element.

References

1. Golpel, W. and Schierbaum, K.D. Sensors and Actuators B26/27 (1995) 1-12.
2. Yamazoe, N. and Miura, N. Sensors and Actuators B20 (1994) 95-102.
3. Novotny, V.J. and Kao, A.S. IEEE Trans. Magnet. 26(5) (1990) 2499.
4. Sanon, G., Rup, R. and Mansingh A. Phys. Stat. Sol. 135 (1993): 581.
5. Iwamoto, M., Shimono, K., Sumi, M., Koyama, K. and Kamo, N. J. Phys. Chem.B 103 (1999) 10311.
6. Ando, E., Suzuki, S., Shimizu, J. and Hayashi, Y. Thin Solid Films 351 (1999) 301.
7. Nasr, C., Hotchandani, S. and Kamat, P.V. J. Phys. Chem.B 102 (1998) 4944.
8. Jana, A.K., J. Photochem. Photobiol. A: Chemistry 132 (2000) 1.
9. Ju, D.U., Chung, J.-H., You, D.-J. and Kim S.-G. Ind. Eng. Chem. Res. 37 (1998) 1827.
10. Shanthi, S., Subramanian, C. and Ramasamy, P. Mat.Sci.Eng.B 57 (1999) 127.
11. Polcado, A.M., Palmas, S., Renoldi, F. and Mascia M. J. Appl. Echem. 29 (1999) 147.
12. Liu, W., Huang, X., Wang, Z., Li, H. and Chen L., J. Electrochem. Soc. 145(1) (1998) 59.
13. Retoux, R., Brousse, T. and Schleich D.M., J. Electrochem. Soc. 146(7) (1999) 2472.
14. Morales, J. and Sánchez, L. J. Electrochem. Soc. 146(5) (1999) 1640.
15. Heiland, G. and Kohl D. Physical and chemical aspects of oxide semiconductor gas sensors. Chemical Sensor Technology 1 (1988) 15-38.
16. Nanthakumar, A. and Armstrong N.R. Semiconductor Electrodes, ed. by H.O. Finklea, chap. 4. Studies in Physical and Theoretical Chemistry 55 (1988) Elsevier, Amsterdam.
17. Cirera A. Ph.D. Thesis. (2000) Universitat de Barcelona.
18. Klein C. and HurlbuC.S. Jr. Manual of Mineralogy J. Wiley & Sons, Inc., 21st Ed. (1997).
19. Robertson, J. Electronic structure of SnO₂, GeO₂, PbO₂, TeO₂ and MgF₂. J.Phys. C 12 (1979) 4767-4776.
20. Samson, S. and Fonstal C.G. Defect Structure and Electronic Donor Levels in Stannic Oxide Crystals. J. Appl. Phys. 44 (1973) 4618-4621.

21. Nagasawa, M. and Shionoya, S. Properties of Oxidized SnO₂ Single Crystals, Japan J. Appl. Phys. 10 (1971) 727-731.
22. Semancik, S. and Fryberg, T.B. Model Studies of Tin Oxide Based Gas Sensors. AIChE Symp. Ser. (267)85 (1989) 46-51.
23. Ihokura, K., Research on sintered tin oxide gas sensors for combustible gases. Ph.D. thesis (1983) Kyushu University.
24. Seiyama, T., et al. Gas detection by activated semiconductive sensors, Denki Kagaku, J. Electrochem. Soc. Japan 40 (1972) 44.
25. Ihokura, K. A tin dioxide gas sensor for deoxidizing gases. New Mater. New Process. Electrochem. Technol. 1 (1981) 43.
26. Kubokawa, Y., et al. The electrical conductivity change caused by the chemisorption of hydrogen on ZnO, ZnO-Cr₂O₃ and ZnO-MoO₃. J. Phys. Chem. 60 (1965) 833.
27. Ihokura, K. and Watson, J. The stannic oxide gas sensor, principles and applications (1993) 71-72.
28. Moseley P.T. and Tofield, B.C. Solid State Gas Sensors (1987) 92-95.
29. Beekmans, N.M. J.Chem. Soc.Faraday Trans.I 74 (1978) 31-45.
30. Nakagawa, M. and Mitsudo, H. Surface. Sci. 175 (1986) 157-176.
31. Van den Broek, J. Phillips Red. Rept. 22 (1967) 367-374.
32. Lalauze, R., Bui, N. and Pijolat, C. Sensors and Actuator 5 (1984) 55-63.
33. Sayago, I., Gutierrez, J., Ares, L., Robla, J. and M.C.Horrillo I. The effect of additive in tin oxide on the sensitivity and selectivity to NO_x and CO. Sensors and Actuators B 26-27 (1995) 19-23.
34. Martinelli, G., Carotta, M.C., Passari, L. and Tracchi, L. A study of the moisture effects on SnO₂ thick films by sensitivity and permittivity measurements. Sensors and Actuators B 26-27 (1995) 53-55.
35. Mcaleer, J.F., Moseley, P.T., Norris, J.O.W., Williams, D.E. and Tofield, B.C. Tin dioxide gas sensors, Part 2-The role of surface additives. J. Chem. Soc., Faraday Tran.I 84 (1988) 441-457.
36. Castro, M.S. and Aldao, C.M. Effects of thermal treatments on the conductance of tin oxide. J. European Ceramic. Soc. 20 (2000) 303-307.

37. Becker, Th., Ahlers, S., Bosch, Chr., Braunmuhl, V., Muller, G. and Kiesewetter, O. Gas sensing properties of thin-and thick-film tin-oxide materials. Sensors and Actuators B 77 (2001) 55-61.
38. Tournier, G., Pijolat, C., Lalauze, R. and Patissier, B. Selective detection of CO and CH₄ with gas sensors using SnO₂ dope with palladium. Sensors and Actuators B 26-27 (1995) 24-28.
39. Liu, W., Cao, X., Zhu, Y. and Cao, L. The effect of dopants on the electronic structure of SnO₂ thin film. Sensors and Actuators B 66 (2000) 219-221.
40. Shokr, E.Kh., Wakkad, M.M., Abd El-Ghanny, H.A. and Ali, H.M. Sb-doping effects on optical and electrical parameters of SnO₂ films, J. Physics and Chemistry of Solids 61 (2000) 75-85.
41. Mishra V.N. and Agarwal R.P. Sensitivity, response and recovery time of SnO₂ based thick-film sensor array for H₂, CO, CH₄ and LPG, J. Microelectronics 29 (1998) 861-874.
42. Phani, A.R., Manorama, S. and Rao, V.J. Preparation, characterization and electrical properties of SnO₂ based liquid petroleum gas sensor. J. Materials Chem and Phys 58 (1999) 101-108.
43. Moseley P.T. Stannic Oxide Gas sensor (1987) 15-16.
44. Jarzebski, Z.M. and Marton, P.J. J. Electrochem.Soc. 123 (1976) 299C.
45. Marley, J.A. and Dockerty, R.K. Phys. Rev. 140 (1965) A304.
46. Nagasawa, M. and Shiniya, S. J. Appl.Phys. 10 (1971) 472.
47. Novel, S., Pijolat, C. And Lalauze, R. Influence of grain size and working temperature on the performance of a sensor proceduced from polycrystalline tin dioxide. Ceramic Today-Tomorrow's Ceramics (1991) 2467-2476.
48. Cox, P.A.and Egdell, R.G. Surf. Sci. 123 (1982) 179-203.
49. Gaoggiotti, G. Surface chemistry of tin oxide based gas sensor. J.Appl.Phys 76(8) (1994) 4467-4471.



APPENDICES

สถาบันวิทยบริการ
จุฬาลงกรณ์มหาวิทยาลัย

APPEXDIX A

The analysis data of particle size distribution of SnO₂ powder obtained by laser light scattering technique.

| size (μm) | | % (mass) | CMPF % ⁽¹⁾ | CMPL % ⁽²⁾ |
|-----------|------|----------|-----------------------|-----------------------|
| 0.15 | 0.17 | 0.00 | 0.00 | 100.00 |
| 0.17 | 0.20 | 0.12 | 0.12 | 99.88 |
| 0.20 | 0.23 | 0.80 | 0.92 | 99.08 |
| 0.23 | 0.27 | 1.64 | 2.56 | 97.44 |
| 0.27 | 0.31 | 2.69 | 5.25 | 94.75 |
| 0.31 | 0.36 | 3.75 | 9.00 | 91.00 |
| 0.36 | 0.42 | 4.88 | 13.88 | 86.12 |
| 0.42 | 0.49 | 6.15 | 20.02 | 79.98 |
| 0.49 | 0.58 | 7.11 | 27.13 | 72.87 |
| 0.58 | 0.67 | 8.11 | 35.24 | 64.76 |
| 0.67 | 0.78 | 8.74 | 43.98 | 56.02 |
| 0.78 | 0.91 | 8.89 | 52.86 | 47.14 |
| 0.91 | 1.06 | 8.36 | 61.22 | 38.78 |
| 1.06 | 1.24 | 7.72 | 68.94 | 31.06 |
| 1.24 | 1.44 | 7.03 | 75.97 | 24.03 |
| 1.44 | 1.68 | 6.16 | 82.13 | 17.87 |
| 1.68 | 1.95 | 5.15 | 87.28 | 12.72 |
| 1.95 | 2.28 | 4.08 | 91.36 | 8.64 |
| 2.28 | 2.65 | 3.06 | 94.43 | 5.57 |
| 2.65 | 3.09 | 2.19 | 96.62 | 3.38 |
| 3.09 | 3.60 | 1.47 | 98.08 | 1.92 |
| 3.60 | 4.19 | 0.92 | 99.00 | 1.00 |
| 4.19 | 4.88 | 0.54 | 99.54 | 0.46 |
| 4.88 | 5.69 | 0.29 | 99.83 | 0.17 |
| 5.69 | 6.63 | 0.12 | 99.95 | 0.05 |
| 6.63 | 7.72 | 0.05 | 100.00 | 0.00 |

- (1) CMPF : Cumulative size distribution which is obtained by summing the fractions of particle that are finer than specific size between the smallest and largest sizes of distribution.
- (2) CMPL : Cumulative size distribution which is obtained by summing the fractions of particle that are larger than specific size between the smallest and largest sizes of distribution.

APPEXDIX B

The analysis data of particle size distribution of Sb_2O_3 powder obtained by laser light scattering technique.

| size (μm) | | % (mass) | CMPF % ⁽¹⁾ | CMPL % ⁽²⁾ |
|------------------------|-------|----------|-----------------------|-----------------------|
| 0.67 | 0.78 | 0.00 | 0.00 | 100.00 |
| 0.78 | 0.91 | 0.05 | 0.05 | 99.95 |
| 0.91 | 1.06 | 0.12 | 0.17 | 99.83 |
| 1.06 | 1.24 | 0.26 | 0.43 | 99.57 |
| 1.24 | 1.44 | 0.57 | 1.00 | 99.00 |
| 1.44 | 1.68 | 1.10 | 2.10 | 97.90 |
| 1.68 | 1.95 | 1.88 | 3.98 | 96.02 |
| 1.95 | 2.28 | 2.85 | 6.83 | 93.17 |
| 2.28 | 2.65 | 4.18 | 11.01 | 88.99 |
| 2.65 | 3.09 | 5.60 | 16.61 | 83.39 |
| 3.09 | 3.6 | 7.15 | 23.76 | 76.24 |
| 3.6 | 4.19 | 8.70 | 32.46 | 67.54 |
| 4.19 | 4.88 | 9.87 | 42.33 | 57.67 |
| 4.88 | 5.69 | 10.58 | 52.90 | 47.10 |
| 5.69 | 6.63 | 10.81 | 63.72 | 36.28 |
| 6.63 | 7.72 | 10.66 | 74.38 | 25.62 |
| 7.72 | 9.00 | 9.00 | 83.38 | 16.62 |
| 9.00 | 10.48 | 6.91 | 90.29 | 9.71 |
| 10.48 | 12.21 | 4.77 | 95.06 | 4.94 |
| 12.21 | 14.22 | 2.87 | 97.93 | 2.07 |
| 14.22 | 16.57 | 1.43 | 99.36 | 0.64 |
| 16.57 | 19.31 | 0.54 | 99.89 | 0.11 |
| 19.31 | 22.49 | 0.11 | 100.00 | 0.00 |

- (1) CMPF : Cumulative size distribution which is obtained by summing the fractions of particle that are finer than specific size between the smallest and largest sizes of distribution.
- (2) CMPL : Cumulative size distribution which is obtained by summing the fractions of particle that are larger than specific size between the smallest and largest sizes of distribution.

APPENDIX C

The analysis data of particle size distribution of 0.3wt% Sb_2O_3 doped SnO_2 after wet ball milling.

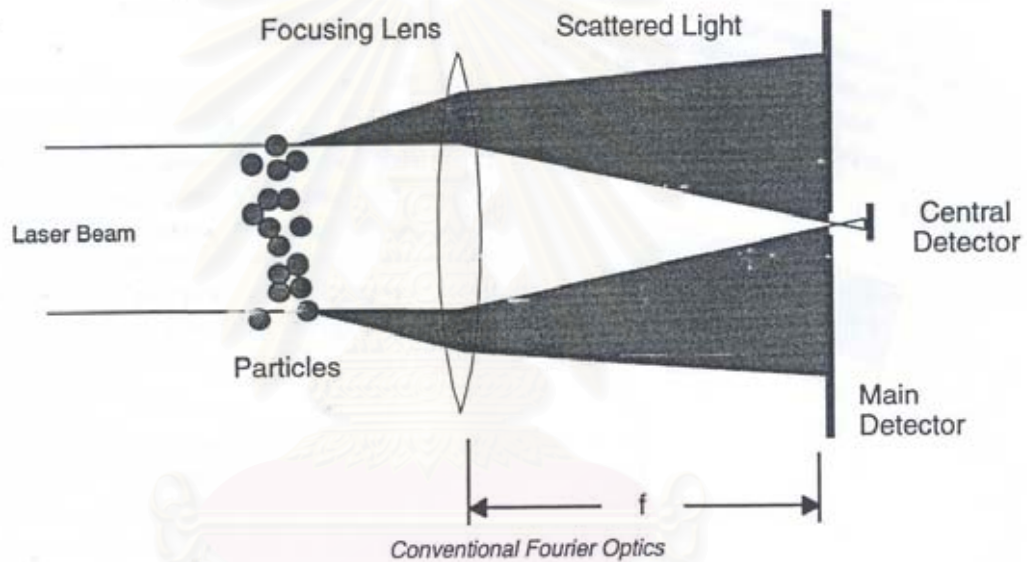
| size (μm) | | % (mass) | CMPL % ⁽¹⁾ | CMPF % (2) |
|------------------------|------|----------|-----------------------|------------|
| 0.04 | 0.05 | 0.00 | 0.00 | 100.00 |
| 0.05 | 0.06 | 1.96 | 1.96 | 98.04 |
| 0.06 | 0.07 | 3.35 | 5.30 | 94.70 |
| 0.07 | 0.08 | 4.43 | 9.74 | 90.26 |
| 0.08 | 0.09 | 5.32 | 15.06 | 84.94 |
| 0.09 | 0.11 | 6.08 | 21.14 | 78.86 |
| 0.11 | 0.13 | 6.73 | 27.87 | 72.13 |
| 0.13 | 0.15 | 7.24 | 35.10 | 64.90 |
| 0.15 | 0.17 | 7.59 | 42.69 | 57.31 |
| 0.17 | 0.20 | 7.73 | 50.42 | 49.58 |
| 0.20 | 0.23 | 7.65 | 58.07 | 41.93 |
| 0.23 | 0.27 | 7.33 | 65.40 | 34.60 |
| 0.27 | 0.31 | 6.79 | 72.18 | 27.82 |
| 0.31 | 0.36 | 6.09 | 78.28 | 21.72 |
| 0.36 | 0.42 | 5.29 | 83.57 | 16.43 |
| 0.42 | 0.49 | 4.40 | 87.97 | 12.03 |
| 0.49 | 0.58 | 3.50 | 91.47 | 8.53 |
| 0.58 | 0.67 | 2.60 | 94.07 | 5.93 |
| 0.67 | 0.78 | 1.78 | 95.85 | 4.15 |
| 0.78 | 0.91 | 1.11 | 96.96 | 3.04 |
| 0.91 | 1.06 | 0.64 | 97.60 | 2.40 |
| 1.06 | 1.27 | 0.39 | 97.99 | 2.01 |
| 1.27 | 1.44 | 0.32 | 98.31 | 1.69 |
| 1.44 | 1.68 | 0.32 | 98.63 | 1.37 |
| 1.68 | 1.95 | 0.31 | 98.94 | 1.06 |
| 1.95 | 2.28 | 0.28 | 99.21 | 0.79 |
| 2.28 | 2.65 | 0.23 | 99.44 | 0.56 |
| 2.65 | 3.09 | 0.17 | 99.61 | 0.39 |
| 3.09 | 3.60 | 0.12 | 99.73 | 0.27 |
| 3.60 | 4.19 | 0.10 | 99.84 | 0.16 |
| 4.19 | 4.88 | 0.08 | 99.92 | 0.08 |
| 4.88 | 5.69 | 0.08 | 100.00 | 0.00 |

- (1) CMPF : Cumulative size distribution which is obtained by summing the fractions of particle that are finer than specific size between the smallest and largest sizes of distribution.
- (2) CMPL : Cumulative size distribution which is obtained by summing the fractions of particle that are larger than specific size between the smallest and largest sizes of distribution.

APPEXDIX D

Conventional Fourier Optics

The conventional optical configuration is shown diagrammatically in the figure below. The light from a low power Helium-Neon laser is used to form a collimated and monochromatic beam of light, of maximum 18 mm in diameter. This beam of light is known as the analyser beam and any particle present within it will scatter this laser light. The particles are introduced to the analyser beam by sample presentation modules or by direct spraying through the measurement area.



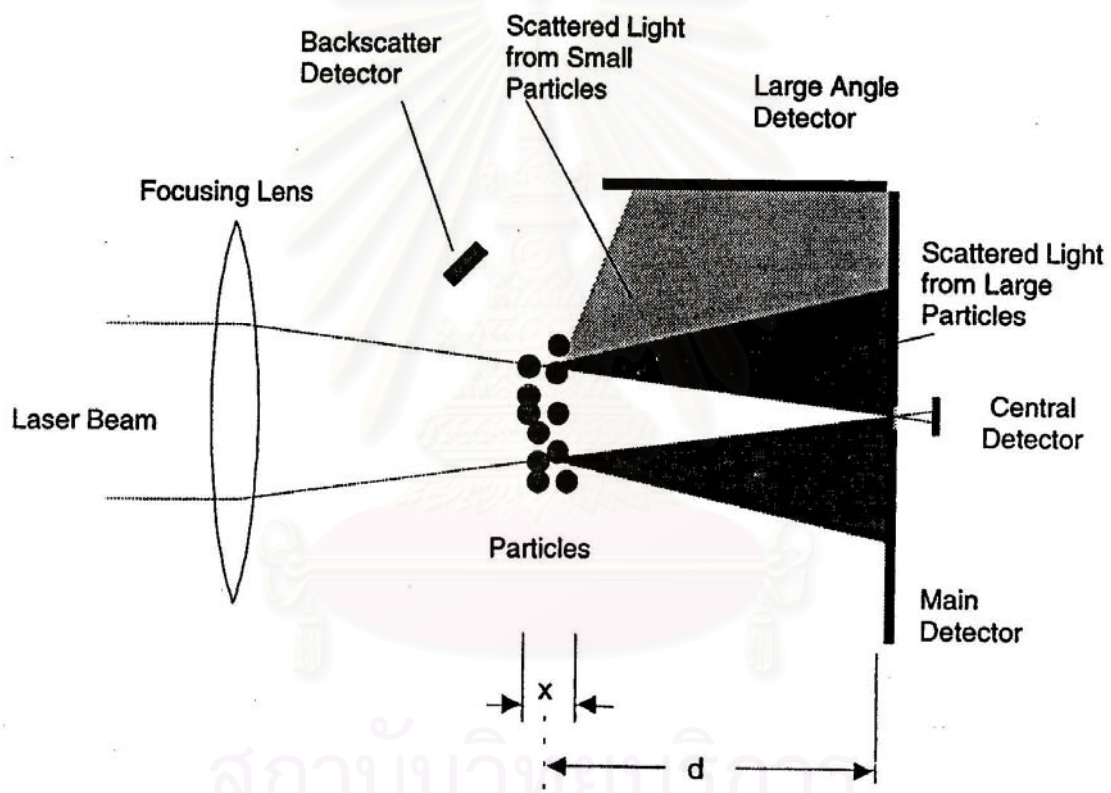
This light scattered by the particles and the unscattered remainder are incident on a receiver lens also known as the rang lens. This operates as a Fourier transform lens forming the far field diffraction pattern of the scattered light at its focal plane. Here a custom designed detector, in the form of a series of angular sectors, gathers the scattered light over a range of solid angles of scatter.

The unscattered light is brought to a focus on the detector and passes through a small aperture in the detector and out of the optical system. The total laser power passing out of the system. The total laser power passing out of the system in this way is monitored allowing the sample volume concentration to be determined.

APPENDIX E

Reverse Fourier Optics Configuration

In this optical configuration of the components is altered. However, in principle, the measurement made is the same. The need for this configuration is to allow the accurate measurement of scattering much higher angles than is possible by the conventional method. The figure below illustrates the component layout and shows the extra detectors on the Mastersizer S and Microplus to measure large angle scattering and backscatter (scattering at angles greater than 90°).



Reverse Fourier Optics of the Mastersizer S and Microplus

The laser beam is expanded as in the conventional optics but, instead of forming a collimated analyser beam, the output beam is focused to a point in the plane of the detector. The cell is placed at an accurately determined distance from the detector plane in this converging analyser beam. In this configuration the detector still measures the effective far field diffraction pattern. However, the scaling constant, which is the focal length f for the conventional optics, becomes the cell

detector distance d in the reverse Fourier configuration. Now, if the cell is moved closer to detector, the diffraction pattern becomes smaller on the detector. If it moves further away it grows larger.

However, the second method also has a drawback, and it is for this reason the Mastersizer allows both optical methods to be used. The scale of the scattering pattern formed on the detector depends upon the distance from the detector to the scatter. Thus if the particles are allowed to spread over a significant distance x along the optical axis an apparent size spreading will also occur proportional to the ratio of $[d+x]/d$. Mastersizer has the unique capability of being able to measure samples dispersed in the liquids down to $0.05 \mu\text{m}$ whilst retaining the ability also to measure sprays and dry powder aerosols down to $0.5 \mu\text{m}$.



APPENDIX F

| 21-1250 | | Wavelength= 1.54184 | | | |
|---|---------|---------------------|---|---|---|
| SnO2 | 2θ | Int | h | k | l |
| Tin Oxide | 26.601* | 100 | 1 | 1 | 0 |
| | 33.904* | 81 | 1 | 0 | 1 |
| | 37.982* | 24 | 2 | 0 | 0 |
| Cassiterite, syn | 39.008* | 5 | 1 | 1 | 1 |
| | 42.648* | 2 | 2 | 1 | 0 |
| Rad.: CuKα1 λ: 1.5405 Filter: Ni Beta.M d-sp: | 51.797* | 63 | 2 | 1 | 1 |
| Cut off: Int.: Diffract. I/leor.: | 54.807* | 17 | 2 | 2 | 0 |
| Ref: Swanson, Tatge, Natl. Bur. Stand. (U.S.), Circ. 539, 1, 54 (1953) | 57.886* | 8 | 0 | 0 | 2 |
| | 61.946* | 13 | 3 | 1 | 0 |
| | 64.787* | 17 | 1 | 1 | 2 |
| | 66.025* | 15 | 3 | 0 | 1 |
| Sys.: Tetragonal S.G.: P4 ₂ /mnm (136) | 71.344* | 7 | 2 | 0 | 2 |
| a: 4.738 b: c: 3.188 A: C: 0.6729 | 78.766* | 11 | 3 | 2 | 1 |
| α: β: γ: Z: 2 mp: | 81.251* | 3 | 4 | 0 | 0 |
| Ref: Ibid. | 83.743* | 8 | 2 | 2 | 2 |
| | 87.287* | 3 | 3 | 3 | 0 |
| | 89.816* | 8 | 3 | 1 | 2 |
| | 90.984* | 8 | 4 | 1 | 1 |
| Dx: 6.993 Dm: 7.020 SS/FOM: F ₃₀ =20(.031, 49) | 93.433* | 3 | 4 | 2 | 0 |
| | 96.169* | 4 | 1 | 0 | 3 |
| ω: ηβ: 2.006 σ _r : 2.0972 Sign: + 2V: | 108.401 | 8 | 4 | 0 | 2 |
| | 112.146 | 3 | 5 | 1 | 0 |
| Ref: Winchell, A., Winchell, H., Microscopic Character of Artificial Inorg. Solid Sub., 62 (1964) | 114.955 | 3 | 3 | 3 | 2 |
| | 116.193 | 8 | 4 | 3 | 1 |
| | 121.891 | 7 | 3 | 0 | 3 |
| Color: White | 122.008 | 6 | | | |
| Sample from Johnson, Matthey Co., Ltd. Their spectroscopic analysis showed no impurities greater than faint trace. X-ray pattern taken at 26 C. Optical data on specimen from Dana's System of Mineralogy, 7th Ed., 1 555. Opaque mineral optical data on specimen from Mwirasando mine, Uganda, R3R%=11.5-12.4, Disp.=Std., VHN100=1168-1332, Ref.: IMA Commission on Ore Microscopy QDF. 02 Ti type. Rutile group, rutile subgroup. Also called: tin stone.PSC: tP6. To replace 1-657. Deleted by 41-1445, lower Fn, Bayliss, 8/90. Mwt: 150.69. Volume[CD]: 71.57. | 130.764 | 6 | 5 | 2 | 1 |
| | 133.999 | 1 | 4 | 4 | 0 |
| | 137.880 | 4 | 3 | 2 | 3 |
| | 143.181 | 2 | 5 | 3 | 0 |
| | 147.697 | 6 | 5 | 1 | 2 |

สถาบันวิทยบริการ
จุฬาลงกรณ์มหาวิทยาลัย

APPENDIX G

| 05-0534 | | Wavelength= 1.54184 | | | | | | | | | |
|---|--|---------------------|-----|----|---|---|------------|-----|----|---|---|
| Sb203 | | 2 θ | Int | h | k | l | 2 θ | Int | h | k | l |
| Antimony Oxide | | 13.751* | 12 | 1 | 1 | 1 | 130.034 | 3 | 10 | 6 | 6 |
| | | 27.732* | 100 | 2 | 2 | 2 | 133.013 | 2 | 12 | 4 | 4 |
| | | 32.104* | 40 | 4 | 0 | 0 | 135.312 | 3 | 13 | 3 | 1 |
| Senarmonite, syn | | 35.086* | 11 | 3 | 3 | 1 | 142.099 | 2 | 13 | 3 | 3 |
| Rad.: CuK α λ : 1.5405 Filter: Ni Beta.M d-sp: Diffractometer | | 39.597* | 2 | 4 | 2 | 2 | 149.741 | 2 | 13 | 5 | 1 |
| Cut off: Int.: Diffract. I/lor.: | | 42.127* | 3 | 5 | 1 | 1 | | | | | |
| Ref: Swanson, Fuyat, Natl. Bur. Stand. (U.S.), Circ. 539, 3, 31 (1954) | | 46.025* | 42 | 4 | 4 | 0 | | | | | |
| | | 48.281* | 2 | 5 | 3 | 1 | | | | | |
| | | 54.595* | 35 | 6 | 2 | 2 | | | | | |
| | | 57.180* | 11 | 4 | 4 | 4 | | | | | |
| Sys.: Cubic S.G.: Fd3m (227) | | 59.148* | 7 | 5 | 5 | 1 | | | | | |
| a: 11.152 b: c: A: C: | | 64.138* | 3 | 7 | 3 | 1 | | | | | |
| α : β : γ : Z: 16 mp: | | 67.150* | 4 | 8 | 0 | 0 | | | | | |
| Ref: Ibid. | | 68.889* | 4 | 7 | 3 | 3 | | | | | |
| | | 74.135* | 12 | 6 | 6 | 2 | | | | | |
| Dx: 5.584 Dm: SS/FOM: F ₃₀ =37(.0171, 48) | | 76.373* | 8 | 8 | 4 | 0 | | | | | |
| | | 78.076* | 2 | 9 | 1 | 1 | | | | | |
| | | 82.485* | 1 | 9 | 3 | 1 | | | | | |
| | | 85.250* | 5 | 8 | 4 | 4 | | | | | |
| | | 91.277* | 4 | 9 | 5 | 1 | | | | | |
| | | 91.835* | 6 | 10 | 2 | 2 | | | | | |
| | | 95.655* | 1 | 9 | 5 | 3 | | | | | |
| Ref: Dana's System of Mineralogy, 7th Ed., I, 544 (1944) | | 100.104 | 1 | 11 | 1 | 1 | | | | | |
| | | 102.893 | 2 | 8 | 8 | 0 | | | | | |
| | | 104.591 | 3 | 9 | 7 | 1 | | | | | |
| | | 109.211 | 1 | 9 | 7 | 3 | | | | | |
| | | 109.761 | 5 | 10 | 6 | 2 | | | | | |
| Color: Colorless, grayish white | | 112.146 | 3 | 12 | 0 | 0 | | | | | |
| Pattern taken at 26 C. Sample from Mallinckrodt Chemical Works. Spectroscopic analysis: <0.1% Pb, Si; <0.01% Ag, As, Ca, Cu, Fe, Sn, Ni; <0.001% Al, Au, Ba, Bi, Ca, Co, Na, Ti; <0.0001% Cs, In, K, Li, Mg. Also orthorhombic form, valentinite. | | 113.927 | <1 | 11 | 5 | 1 | | | | | |
| Isostructural with arsenolite. As ₂ O ₃ type. Iron group, iron subgroup. Also called: antimony bloom.PSC: cF80. Validated by calculated pattern 43-1071. Mwt: 291.50, Volume[CD]: 1386.94. | | 118.810 | <1 | 11 | 5 | 3 | | | | | |
| | | 121.938 | 2 | 12 | 4 | 0 | | | | | |
| | | 123.931 | 1 | 9 | 9 | 1 | | | | | |
| | | 129.403 | 3 | 11 | 7 | 1 | | | | | |

สถาบันวิทยบริการ
จุฬาลงกรณ์มหาวิทยาลัย

VITA

Miss. Utoomporn Korkerd was born on the 11th of March 1979, in Bangkok. After graduating with a Bachelor's Degree in Physics from Faculty of Science, Chulalongkorn University in 2001. She continued a further study in Master's Degree in the field of Ceramic Technology at Chulalongkorn University and graduated in April 2004.



สถาบันวิทยบริการ
จุฬาลงกรณ์มหาวิทยาลัย